Efficient Algorithms for Retrospective Motion Correction in MRI

by

Yuan Bian

A dissertation submitted to the Graduate Faculty of
Auburn University
in partial fulfillment of the
requirements for the Degree of
Doctor of Philosophy

Auburn, Alabama
August 3, 2019

Keywords: MRI motion correction, retrospective motion correction, GANs, image registration, image reconstruction

Approved by

Stanley J. Reeves, Chair, Professor of Electrical and Computer Engineering
Thomas S. Denney Jr., Professor of Electrical and Computer Engineering
Gopi Deshpande, Associate Professor of Electrical and Computer Engineering
Dmitry Glotov, Associate Professor of Mathematics and Statistics
George T. Flowers, Professor and Dean of Graduate School

Abstract

Compared with other medical imaging modalities, MR imaging is time consuming due to the relatively slow sequential data acquisition pattern. Hence, motion is often an unavoidable issue for MRI. Object motion during the signal acquisition can reduce image quality due to the induced artifacts, which further hinders diagnosis and scientific research. These degraded images may require repeated scans, which leads to treatment delay and cost increases. If images with motion artifacts are not properly interpreted, erroneous diagnoses and false scientific findings may occur.

To reduce motion artifacts, three groups of methods are used by practitioners: motion prevention, artifact mitigation, and motion correction. Motion prevention methods are the most straightforward way to reduce motion artifacts. However, these may not always be suitable or effective. Artifact mitigation methods mainly include faster imaging and periodic triggering and gating. Imaging speed has limits, and triggering and gating require extra time, effort, and complexity. Therefore, motion correction methods have received significant attention.

MRI motion correction techniques can be classified into three groups: motion correction based on k-space trajectories, prospective motion correction (PMC) and retrospective motion correction (RMC). Motion correction based on k-space trajectories relies on specially designed and implemented trajectories, which limits the flexibility of the techniques and requires more acquisition time. PMC is achieved by obtaining tracking data of the pose (position and orientation) of the object, passing these data to the scanner with minimal delay, and adjusting the MR pulse sequences so that the imaging volume moves to follow the object. PMC requires extra hardware and calibration and sometimes extra acquisition

time. RMC postprocesses the data and reconstructs MR images after the data is fully acquired. In RMC the process of acquisition is independent of motion. RMC includes three main groups: self-navigation motion tracking methods to calculate motion information, autofocusing methods based on evaluation of image quality, and motion correction by training neural networks. Self-navigation motion correction methods rely on Fourier properties by taking advantage of overlapping k-space data to track motion. This approach requires additional k-trajectories, which increases both time and complexity of the scan. Autofocusing methods do not rely on a specific data sample pattern, equipment or sequence design. These approaches assume a rigid body or deformable object motion model and estimate motion model parameters by iterative optimization of an image quality metric when the raw k-space data are modified according to the motion model. Artificial neural network methods establish the mapping relationship between the motion-corrupted images and the no-motion images by training a large number of related images, and estimate motion-corrected images from motion-corrupted images. The focus of this thesis is the development of autofocusing and neural-network approaches to RMC.

In this dissertation, we develop three methods to correct MRI motion retrospectively. The first contribution is an autofocusing motion correction method to address the two challenges of previous methods: high calculation load and local minima. We propose to use multiple linear-motion initializations and joint refinement of a global model to decrease and constrain the search space. In the first step, k-space is divided into several segments based on acquisition order. Linear motion is assumed and searched in each segment to get initial motion parameters. In the second step, several control points are chosen on the piecewise linear initial approximation, and then a piecewise cubic Hermite interpolation polynomial is fitted from the control points to obtain smooth motion curves. The motion curves are refined by optimizing a focus criterion. These strategies make the proposed algorithm efficient and robust. Different focus criteria are compared under the proposed method. To further improve computational efficiency, golden-section search is used to estimate rotation, and

two map data structures are applied to store calculated data. Simulations and experimental results demonstrate that the proposed method can effectively and efficiently correct rigid motion in MR images.

The second contribution of this work is an efficient motion correction method based on fast robust correlation. Translational search can be computationally demanding. A correlation operation can be used to calculate an image match when the matching criterion is the sum of squared errors. However, this approach cannot be used for nonquadratic matching criteria. Fast robust correlation is a computationally efficient search algorithm for translational image matching in the frequency domain. This method can calculate matching surfaces from nonquadratic criteria using a series of high-speed correlations by defining a kernel with sinusoidal terms. The proposed method corrects motion-distorted images by aligning translational motion between images formed by neighboring frequency segments. Since the squared difference kernel is invariant to motion between partial-Fourier images, we adopt the absolute value kernel, which can be easily approximated by sinusoidal terms. Total variation of the sum of partial-Fourier images is chosen as the new matching criterion. FFTs are used to calculate correlations for computational speed. Different search strategies to combine and correct motion over the whole k-space are discussed and compared. The proposed method can perform real-time processing to reduce image motion artifacts significantly in the simulations and MRI cardiac experiments.

The third contribution of this dissertation is a novel data-driven motion correction method for magnitude MR images using generative adversarial networks (GANs). Although the previous proposed methods can correct motion effectively and efficiently, they both require complex-valued raw data. However, raw data is not usually preserved in a clinical environment. In this case the previous two methods cannot be used. GANs (pix2pix model) are implemented to reduce motion artifacts and reconstruct motion-corrupted images through adversarial training between generator and discriminator networks to estimate a motion-corrected image that is close to the reference image. The training set is made of image pairs consisting of motionless reference images and corresponding motion-simulated images. The proposed method is validated by a simulated motion test set and a real motion (experimental) test set.

Acknowledgments

I would like to thank my advisor, Dr. Stanley J. Reeves, for his encouragement and guidance over the years. Dr. Reeves supported me throughout my research with his patience while sharing me with his insightful ideas. This dissertation would never have existed without him.

I would like to thank Dr. Thomas S. Denney, Dr. Gopikrishna Deshpande, and Dr. Meredith Reid, for providing great suggestions in my research. I would like to thank Dr. Dmitry Glotov, who provided invaluable comments for this work. I would like to thank Dr. Ronald Beyers for his help of experimental preparation and MRI data acquisition. I also thank Dr. Yanzhao Cao for serving as the outside reader for this dissertation.

I would like to thank all my group members, especially Xiaoxia Zhang, Sinan Zhao, Yu Shao, Chenxi Hu, Ming Li, Hai Lu, Shuo Shang, and Huanyi Zhou, for their kindness and suggestions during my research.

Finally, I would like to thank my beloved parents, Jinyue Bian and Guang Shao, for the endless love they gave me. They always encourage me and support my decisions in each step of my life. The have always taken care of me no matter where I was.

Table of Contents

Abstract ii

Acknowledgments vi

List of Figures x

List of Tables xx

1 Introduction 1

1.1 MRI basics 1

1.1.1 MRI physics 1

1.1.2 MR image formation 2

1.2 MRI motion 4

1.3 Overview of the dissertation 6

2 MRI Motion Correction 8

2.1 Motion correction based on k-space trajectories 8

2.2 Prospective motion correction 9

2.2.1 motion correction strategy 10

2.2.2 motion tracking 11

2.3 PMC methods 13

2.3.1 PACE and PROMO 13

2.3.2 SNAV 14

2.4 Retrospective motion correction 15

2.5 Autofocusing methods 16

2.5.1 automatic correction of motion artifacts in Magnetic Resonance images using an entropy focus criterion 16

2.5.2 blind retrospective motion correction of MR images 18

2.5.3 nonrigid motion correction in 3D using autofocusing with localized linear translations 19
2.6 Artificial neural network methods 20
2.7 Advantages and limitations of PMC and RMC 20
2.7.1 advantages of PMC 20
2.7.2 limitations of PMC 21
2.7.3 advantages of RMC 22
2.7.4 limitations of RMC 22
3 Image Registration 25
3.1 Transformation models 28
3.2 Matching criteria 31
3.3 Optimization methods 35
4 An Efficient and Robust Autofocusing MR Image Motion Correction Method using Global Motion Estimation 37
4.1 Motion model and acquisition assumption 38
4.2 Previous search strategies 39
4.3 Focus criteria 40
4.4 Proposed method 42
4.5 Golden-section search 47
4.6 Map data structure 49
4.7 Interpolation methods 50
4.8 Simulations 52
4.9 Experiments 61
4.10 Discussion 63
5 An Efficient Motion Correction Method Based on Fast Robust Correlation . . . 64
5.1 Fast robust correlation review 65
5.2 Motion model and assumption 66

5.3 Squared kernel 67

5.4 Proposed match criterion 68

5.5 Proposed method 71

5.6 Search strategy 72

5.7 Simulations 78

5.7.1 comparison of search strategies 78

5.7.2 examples of the proposed method 83

5.8 Experiments 88

5.9 Discussion 90

6 Motion Correction of Magnitude MR Images using Generative Adversarial Networks 91

6.1 Artificial neural networks 91

6.2 Convolutional neural networks 94

6.3 Generative adversarial networks (pix2pix model) 95

6.4 Dataset and training 98

6.5 Results 99

7 Conclusions 106

List of Figures

1.1 Excitation process. Left: The net magnetization is parallel to the external strong magnetic field B_0 before an RF pulse. Center and right: An RF pulse with the resonant frequency allows the RF energy to be absorbed by the protons, and makes the net magnetization to rotate away from B_0. (This image is from [80]) 2

1.2 Three gradient coils are inside the bore of an MR scanner. (This image is from the link `https://slideplayer.com/slide/9887251/`) 3

2.1 Trajectories of a PROPELLER composed of 9 strips. (Figure 2.1 is from[77].) . 9

2.2 The strategy of PMC. 10

2.3 Gradients change with rotation of the head. (Figure 2.3 is from [64].) 11

2.4 Process of PACE. 13

2.5 3D IR-SPGR sequence with SP-Navs and EKF. (Figure 2.5 is from [100].) . . . 14

2.6 (a) Signal amplitude of spherical shell (b) before and (c) after a 12° relative rotation. (Figure 2.6 is from [98].) 15

2.7 Optimization strategy of Blind Retrospective Motion Correction of MR Images. The k-space data is processed from center (low frequency part) to the whole k-space to optimize motion parameters using coarse to fine optimization. (Figure 2.7 is from [59].) 19

2.8 (a) Sample locations after RMC correction for rotation object. (b) Sample locations after PMC for rotation object. 23

3.1 Different times brain images registration to detect a lesion. (This image is from the link https://thebestphotos.eu/detection-of-focal-longitudinal-changes-in-the-brai html) 26

3.2 Different views aerial images registration to extend the view. (This image is from MathWorks website Image Registration section, and the link is https://www.mathworks.com/discovery/image-registration.html) 26

3.3 Different sensors brain images registration to fuse images. (This image is from UCF Medical Image Computing (CAP 5937) slices (Spring 2016), and the link is http://www.cs.ucf.edu/\protect\unhbox\voidb@x\penalty\@M\{}bagci/teaching/mic16/lec15.pdf) 26

3.4 The steps of area-based registration methods 27

3.5 The steps of feature-based registration methods 27

3.6 Affine transformation model, the parallel lines keep parallel after an affine transformation. 30

3.7 A thin-plate spline that passes through a set of control points. (Figure 3.7 is from the link http://elonen.iki.fi/code/tpsdemo/.) 31

3.8 Left: source image. Middle: target image. Right: deformed source image through B-splines registration. (Figure 3.8 is from [103].) 31

4.1 The motion model of the proposed method. in k-space, each dash line is one k_{phase} line. Different k_{phase} lines have their own motion parameters $(\Delta x, \Delta y, \Delta r)$. Red, green and blue are three k_{phase} lines with three different sets of motion parameters. 39

4.2 The strong relationship between neighboring lines results in motion estimation error. Segment 1 and segment 2 are two neighboring segments in k-space and the green solid line gives the real motion for each k-space line of the segment 1 and the segment 2. Due to the strong bond between the red and blue thick solid lines, the estimated motion of the segment 1 is dominated by the red thick solid line, which results in the errors for other lines in the segment 1. 40

4.3 The process of piecewise linear initial approximation. There are three motion curves with the x axis representing k_{phase} lines and the y axis representing pixels for x, y translations and rotation degree for rotation. The whole k-space is divided into three segments with a certain number of k_{phase} lines in each segment. In Segment 1, the linear estimations of the three motions are chosen from 729 ($9 \times 9 \times 9$, in each motion curve, 9 slopes (blue dashed line) are given) different motion combinations, which can minimize the criterion of the image formed by Segment 1, marked as red lines. In Segment 2, the linear estimations of the three motions are chosen from 729 different motion combinations all starting from the linear estimation of Segment 1, which can minimize the criterion of the image formed by Segment 1 and Segment 2, marked as green lines. The process is repeated for Segment 3. 44

4.4 The process of joint refinement of global model. In the first row, four equally spaced control points (black cross) are chosen on the piecewise linear approximation (red linear lines) for each motion parameter, and the globally criterion optimization is accomplished by refining three piecewise cubic Hermite interpolating polynomials (three green dashed curves) fitted from the four control points. One more control point is added from the previous refined motion curves (red curves in the second row) to get a refined curves (green dashed curves in the second row). The process is repeated until the desired model precision is accomplished (three red curves in the third row). 46

4.5 The process of rotation correction. The frequency domain images are logarithmically scaled. 47

4.6 One step of golden-section search to find the minimum. (Figure 4.6 is from [101].) 48

4.7 The map is used to store the rotated k-space data with rotation angle as the key. When the rotation angle −3.38° is searched, the corresponding rotated k-space matrix $F_{6M\times N}$ is returned. 50

4.8 Rotation interpolation. The frequency domain images are logarithmically scaled. The length and width of the zeropadded images are twice the original image. . . 51

4.9 The difference images comparison. The same image is used as the reference images but different floating image. For (a), the floating image is generated by Figure 4.8. For (b), the floating image is generated by rotating the reference image directly. In order to acquire the same orientation with the reference image, both floating images rotate an angle clockwise and then rotate the same angle counterclockwise. (In order to rotate clockwise and counterclockwise, for (a), the padding zero image is used to rotate and then downsampled.) Both difference images are shown at the same scaling. The dominant error occurs around the edge in (a), while the image content error is the main error in (b) with a bigger margin. 51

4.10 Three different motions. The number of function values (160) corresponds to the number of k_{phase} lines. Horizontal axis coordinates from 1 to 160 correspond to centric-out phase-encode lines acquisition order from the central (low frequency $k_{\text{phase}} = 0$) to the peripheral region of k-space (high frequency); vertical axis coordinates correspond to the motions of each k_{phase} line in one of the three motion directions (two translations with unit pixel and rotation with unit degree). (a) piecewise linear. (b) parabolic. (c) sinusoidal. 52

4.11 Comparison of the reference image, motion-corrupted image, and five corrected images. (a)The reference image. (b)The motion-corrupted image. (c)The motion-corrected image based on image entropy. (d)The motion-corrected image based on the entropy of one-directional gradient of image along the phase-encoding direction. (e)The motion-corrected image based on entropy of two directional gradients of image. (f)The motion-corrected image based on total variation. (g)The motion-corrected image based on the sum of absolute value. 55

4.12 Comparison of the reference image, motion-corrupted image, and five motion-corrected images and corresponding motion estimation plots. (a)The reference image. (b)The simulated motion-corrupted image. (c)The motion-corrected image based on the image entropy. (e)The motion-corrected image based on the entropy of the one-directional gradient of image along the phase-encoding direction. (g)The motion-corrected image based on the entropy of the two directional gradients of image. (i)The motion-corrected image based on the total variation. (k)The motion-corrected image based on the sum of the absolute values. (d)(f)(h)(j)(l) are the comparisons of the estimated motion trajectories and real motion trajectories based on the five criteria. The solid curves represent real motion trajectories (green for horizontal motion, red for vertical motion and black for rotation), and the dashed curves represent estimated motion trajectories (green for horizontal translation and red for vertical translation with unit pixel of the y axis; black for rotation with unit degree of the y axis). 57

4.13 Comparison of the reference image, motion-corrupted image, and five motion-corrected images and corresponding motion estimation plots. (a)The reference image. (b)The simulated motion-corrupted image. (c)The motion-corrected image based on the image entropy. (e)The motion-corrected image based on the entropy of the one-directional gradient of image along the phase-encoding direction. (g)The motion-corrected image based on the entropy of the two directional gradients of image. (i)The motion-corrected image based on the total variation. (k)The motion-corrected image based on the sum of the absolute values. (d)(f)(h)(j)(l) are the comparisons of the estimated motion trajectories and real motion trajectories based on the five criteria. The solid curves represent real motion trajectories (green for horizontal motion, red for vertical motion and black for rotation), and the dashed curves represent estimated motion trajectories (green for horizontal translation and red for vertical translation with unit pixel of the y axis; black for rotation with unit degree of the y axis). 60

4.14 Comparison of the reference image, real motion-corrupted image and motion-corrected image in the sagittal plane. Due to the motion difference between the neck part and the head part, the image above the green dashed line part was used to calculate the focus criterion. (a) No-motion (reference) image. (b) Real motion-corrupted image. (c) Motion-corrected image. 62

4.15 Comparison of the no-motion image, real motion-corrupted image and motion-corrected image in the axial plane. (a) No-motion (reference) image. (b) Real motion-corrupted image. (c) Motion-corrected image. 62

5.1 The motion assumption for the proposed motion correction method. We only consider the motion between different segments. Within each segment, the object is assumed motionless. 67

5.2 The comparison between the filtered and unfiltered square wave. (a) The magnitude and phase of the filter. (b) The filtered and unfiltered square wave. . . . 69

5.3 Comparison of different values of P and the absolute value kernel. (a) $P = 1$. (b) $P = 2$. (c) $P = 3$. (d) $P = 4$. (e) $P = 5$. (d) $P = 6$. 70

5.4 Search Strategy 1 of the proposed method. Different numbers represent different segments. The yellow segment is the reference segment, the light blue one is the corresponding floating segment, and the blue one is the motion-corrected segment. From top to bottom, the relative motion between the reference and floating segments is determined. 73

5.5 Search Strategy 2 of the proposed method. Different numbers represent different segments. The blue segment is the reference segment, and the light blue one is the corresponding floating segment. The reference segment is enlarged after combining the previous corrected floating segment until all the segments are corrected. 74

5.6 Search Strategy 3 of the proposed method. The blue segment is the reference segment, and the light blue one is the corresponding floating segment. The reference segment is enlarged after combining the previous corrected floating segment until all the segments are corrected. The neighboring symmetric segments are in turn chosen as the floating segments. 75

5.7 Search Strategy 4 of the proposed method. The blue segment is the reference segment, the light blue one is the corresponding floating segment and the yellow one is the segment corrected twice. Take segment 3 for example. Segment 3 and 4 are symmetric segments. After segment 3 and segment 4 are corrected in turn, the segment 3 is corrected again with the corrected segment 4 as part of the reference. 76

5.8 Search Strategy 5 of the proposed method. The blue segment is the reference segment, the light blue one is the corresponding floating segment and the yellow one is the segment corrected twice. The symmetric segments are corrected twice. 77

5.9 Example 1 of the proposed method with segment size 8. 84

5.10 Example 2 of the proposed method with segment size 10. 85

5.11 Example 3 of the proposed method with segment size 12. 86

5.12 Example 4 of the proposed method with segment size 15. 87

5.13 Comparison of breath-hold no-motion images, original free-breathing images and reconstructed images from the original free-breathing images for two cardiac phases. The first row is one cardiac phase, and the second row is the other cardiac phase. (a)(d) breath-hold no-motion images. (b)(e) original free-breathing images. (c)(f) reconstructed images from the original free-breathing images. . . 89

6.1 One multilayer perceptron neural network. The blue neurons represent the neurons from input layer, the green neurons represent the neurons from hidden layers, and the purple neuron represent the neurons from output layer 92

6.2 Example of a convolutional neural network. (Figure 6.2 is from [62].) 94

6.3 An example of a GAN. (Figure 6.2 is from `https://skymind.ai/wiki/generative-adversarial-ne`

6.4 An example of a cGAN. The discriminator D is trained to distinguish the tuple between motion-corrected image $G(y)$ and motion-corrupted image y from the tuple between motionless image x and motion-corrupted image y. The generator G is trained to fool the discriminator D. Both the generator G and discriminator D can access the motion corrupted image y in the cGAN. 97

6.5 Results of motion correction on five simulation datasets from the simulation test set. For each dataset, we use two rows to compare the results. The first row consists of three images from left to right: motionless image (reference), motion-corrupted image, the absolute value of the difference between the reference and motion-corrupted image. The second row consists of three images from left to right: motionless image (reference), motion-corrected image, the absolute value of the difference between the reference and motion-corrected image. 104

6.6 Results of motion correction on two experimental datasets from the experimental test set. The first column shows no-motion images generated by subject motion in the experiment; the second column shows motion-corrupted images generated by motionless subject in the experiment; the third column shows the motion-corrected images through pix2pix model. 105

List of Tables

3.1 Search directions of different algorithms 35

5.1 Average translational motion estimation errors (two directions Δ_x,Δ_y) of each k-space segment (8 lines) for each search strategy (pixel/unit) 80

5.2 Average values of four criteria of the reference image, the motion blurred images and the five reconstructed images from the five search strategies (8 lines segment) 80

5.3 Average translational motion estimation errors (two directions Δ_x,Δ_y) of each k-space segment (10 lines) for each search strategy (pixel/unit) 81

5.4 Average values of four criteria of the reference image, the motion blurred images and the five reconstructed images from the five search strategies (10 lines segment) 81

5.5 Average translational motion estimation errors (two directions Δ_x,Δ_y) of each k-space segment (12 lines) for each search strategy (pixel/unit) 81

5.6 Average values of four criteria of the reference image, the motion blurred images and the five reconstructed images from the five search strategies (12 lines segment) 82

5.7 Average translational motion estimation errors (two directions Δ_x,Δ_y) of each k-space segment (15 lines) for each search strategy (pixel/unit) 82

5.8 Average values of four criteria of the reference image, the motion blurred images and the five reconstructed images from the five search strategies (15 lines segment) 82

6.1 Average values of three metrics of the motion-corrupted images and the motion-corrected images 100

Chapter 1

Introduction

This chapter provides the background of MRI motion, and is organized as follows: 1.1 MRI basics, 1.2 MRI motion, and 1.3 overview of the dissertation.

1.1 MRI basics

Magnetic Resonance Imaging (MRI) is a widely used medical imaging technique which exploits the phenomenon that in a magnetic field, some nuclei can absorb and then re-emit energy, which can be detected under certain conditions. MRI is non-invasive, uses non-ionizing radiation, and provides contrast in soft-tissue structures. This capability is an indispensable imaging tool both in research and in clinical applications. An MRI scanner is a complicated system. Here we only discuss the basic MRI physics and MR image formation.

1.1.1 MRI physics

The physical phenomenon of MRI is called Nuclear Magnetic Resonance. Certain nuclei have a property called nuclear spin, which is randomly oriented without an external magnetic field. When these nuclei are placed in an external strong magnetic field B_0, these spins are quantized to produce a net magnetization vector M, which is in the same direction with B_0. Nuclei can absorb radio-frequency (RF) energy, which can push M out of alignment with B_0 by sending an RF pulse with a certain frequency. M becomes orthogonal to B_0, and the nuclei precess around B_0. This process is called nuclear magnetic resonance or excitation, which is shown in Figure 1.1. The RF pulse is designed to match the resonant frequency of the system to resonate these nuclei. This behavior is characterized by the Larmor equation, which is given by

$$\omega_0 = \gamma B_0, \tag{1.1}$$

where ω_0 is the precession frequency of M under B_0, and γ is the gyromagnetic ratio. Equation (1.1) is fundamental to MRI.

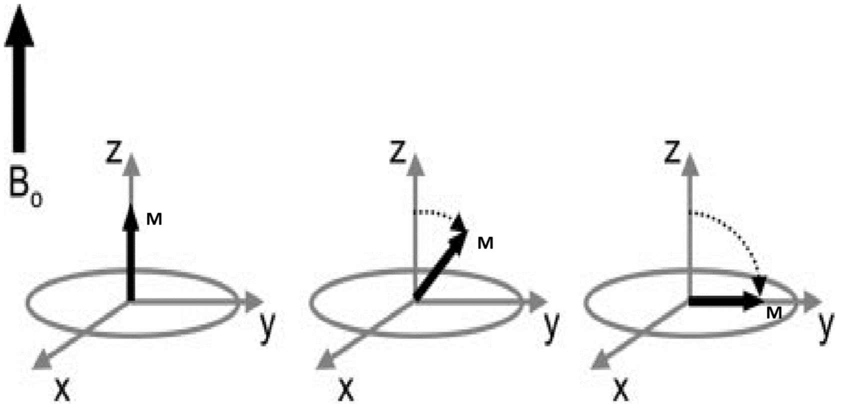

Figure 1.1: Excitation process. Left: The net magnetization is parallel to the external strong magnetic field B_0 before an RF pulse. Center and right: An RF pulse with the resonant frequency allows the RF energy to be absorbed by the protons, and makes the net magnetization to rotate away from B_0. (This image is from [80])

After the RF pulse is withdrawn, M begins to return to the original equilibrium state, which is the same direction as B_0. During the return process, M continues to precess at the frequency ω_0, and energy is emitted. A receiving coil is used to produce a signal by detecting M. The generated signal has the same frequency ω_0.

1.1.2 MR image formation

Spatial encoding is used to match the generated signal to the position of its source. Three gradient coils shown in Figure 1.2, which generate three field gradients G_x, G_y and G_z in the x, y and z directions, are used to achieve spatial encoding. The total magnetic field in the z direction is given by:

$$B_z(z) = B_0 + G_z z, \tag{1.2}$$

where B_0 is in the z direction.

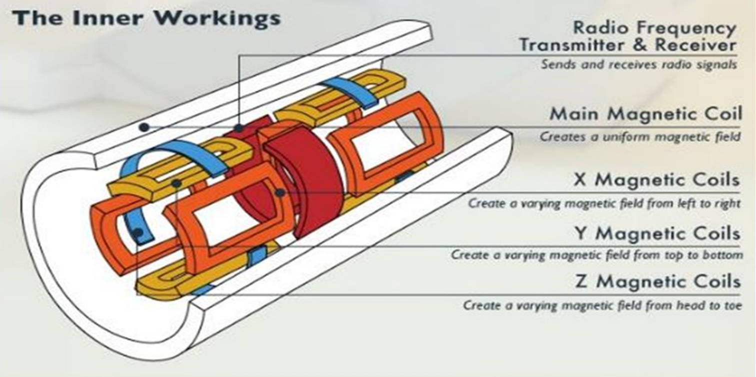
The Inner Workings
Radio Frequency Transmitter & Receiver
Sends and receives radio signals
Main Magnetic Coil
Creates a uniform magnetic field
X Magnetic Coils
Create a varying magnetic field from left to right
Y Magnetic Coils
Create a varying magnetic field from top to bottom
Z Magnetic Coils
Create a varying magnetic field from head to toe

Figure 1.2: Three gradient coils are inside the bore of an MR scanner. (This image is from the link `https://slideplayer.com/slide/9887251/`)

Slice selection is the first step for spatial encoding, which is used to choose a 2D plane from the 3D object to be excited. According to the Larmor equation, Eq (1.2) can be used to implement slice selection.

After slice selection, the spatial encoding becomes a 2D problem within a plane. According to Fourier Series Theory, any image can be represented as the sum of a series of 2D sinusoids. In the spatial encoding of MRI, every sample of the measured signal is the sum of all the spins in the excited slice at one time point. At each time point, the spins are excited in a wave pattern, which corresponds to a particular 2D sinusoid type, across the selected slice. In general, the x direction is called the frequency encoding direction and the y direction is called the phase encoding direction. The sampled domain is called k-space, which is usually sampled in the pattern of an array with the same size as the reconstructed image. The k-space sample values are complex.

According to [71], the relation between samples in k-space $S(k_x, k_y)$ and spin density $\rho(x, y)$ is given by

$$S(k_x, k_y) = \int\int \rho(x, y) \exp\Big\{-i2\pi\big(k_x(t)x + k_y(t)y\big)\Big\}dxdy, \tag{1.3}$$

where $k_x(t)$ and $k_y(t)$ are given by

$$k_x(t) = \frac{\gamma}{2\pi} \int_0^t G_x(\upsilon) d\upsilon, \tag{1.4}$$

$$k_y(t) = \frac{\gamma}{2\pi} \int_0^t G_y(\upsilon) d\upsilon. \tag{1.5}$$

Equation (1.3) is the Fourier transform of $\rho(x, y)$. The inverse Fourier transform of samples in k-space is the reconstructed image, which is given by

$$f(x, y) = \int \int S(k_x, k_y) \exp\Big\{ i2\pi \big(k_x(t)x + k_y(t)y\big) \Big\} dk_x dk_y. \tag{1.6}$$

1.2 MRI motion

Compared with other medical imaging modalities, MR imaging is time consuming due to the relatively slow sequential data acquisition pattern. Hence, motion is often an unavoidable issue for MRI. The common reasons for human motion include:

muscle property. Subjects cannot keep still during the long scan time, because muscles cannot stand long time extension, especially for some gestures.

periodic involuntary motion. These involuntary motions include breathing, cardiac beat, vessel pulsation and blood flow.

disease. Some muscles cannot be controlled due to diseases, such as Parkinson's disease and stroke patients [86].

uncontrollable subjects. Some subjects like children [16, 79] and those with mental disorders may not stay in the scanner compliantly.

Object motion during the signal acquisition can reduce image quality due to the induced artifacts, which further hinders diagnosis and scientific research. These degraded images may require repeated scans, which leads to treatment delay and cost increases. If the artifact images are not reasonably understood, the erroneous diagnoses and false scientific findings may occur [4, 41].

In general, motion artifacts are the results of a combination of effects [108]: image sharp edge blur, ghosting, signal loss, and undesired signal appearance.

MRI motion can have different classification criteria [34]. Based on deformation, motion can be grouped into rigid or nonrigid motion. Based on time difference, motion can be separated into inter-scan and intra-scan motion. The inter-scan motion is motion that occurs between excitation pulses, while intra-scan motion is motion that occurs within an excitation pulse. Based on motion range, for 2D motion, motion within a 2D plane is called in-plane motion, while the motion out of a 2D plane is termed through-plane motion. Motion can also be divided into periodic and random motion.

In order to reduce motion artifacts, three groups of methods are implemented [108]: motion prevention, artifact mitigation, and motion correction.

Motion prevention methods are the most straightforward ways to reduce motion artifacts. Training subjects in MRI environment, scanning during the sleep of infants and babies, using anesthesia for young children [67, 47], constraining bodies by foam restraints or head holders [26], and breath-holding during cardiac or abdomen imaging are the most common strategies to prevent motion. However, these methods are not always effective [102, 67], and some of them are very uncomfortable.

Artifact mitigation methods mainly include faster imaging and periodic triggering and gating.

Faster imaging is used to reduce motion artifacts by improving imaging efficiency. Subjects are likely to keep still and feel less uncomfortable in shorter scan time. Some sequences, such as FLASH [40], bSSFP [85] and EPI, can implement faster imaging. But these methods have tradeoffs between speed and image resolution and SNR. In addition, the acquisition speed cannot be accelerated without bound, considering the practical equipment limitations and human sensation [45]. Even if the acquisition time is made shorter, some kinds of motion still cannot be avoided. Parallel imaging [88, 81, 36] and compressed sensing [63] are other tools to accelerate imaging. Coil sensitivity calibration is a key to parallel imaging.

New artifacts may be introduced if the reference data is not processed properly [38, 76]. Compressed sensing may introduce patchiness artifacts in some cases [110].

Triggering and gating are widely used in cardiac and abdominal imaging, because breath and heartbeat are quasi-periodic. Triggering method collects data at the same cardiac or breath phase of different cycles. Gating acquires data continuously and then reorders the data. Triggering and gating need extra signals and sensors, such as ECG. In addition, both methods rely on a periodicity assumption, which is not easily satisfied for arrhythmia patients and pediatrics, or other kinds of motion.

Neither motion prevention nor artifact mitigation strategies are always practical. Therefore, motion correction methods are often indispensable. We will discuss motion correction methods in Chapter 3 in detail.

1.3 Overview of the dissertation

This dissertation is structured as follows. In Chapter 2, we discuss MRI motion correction techniques, and classify them into three groups: motion correction based on k-space trajectories, prospective motion correction and retrospective motion correction. In Chapter 3, we summarize the image registration problem and discuss three aspects of it—transformation models, matching criteria, and optimization methods. In Chapter 4, we propose an efficient and robust autofocusing MR image motion correction method using global motion estimation to address the two challenges of previous methods: high calculation load and local minima. We propose to use multiple linear-motion initializations and joint refinement of a global model to decrease and constrain the search space. Different focus criteria are compared under the proposed method. To further improve computational efficiency, golden-section search is used to estimate rotation, and two map data structures are applied to store calculated data. In Chapter 5, we propose an efficient motion correction method based on fast robust correlation. The proposed method corrects motion-distorted images by aligning translational motion between images formed by neighboring frequency segments. We adopt the absolute value kernel, which can be easily approximated by sinusoidal terms. Total variation of the sum of partial-Fourier images is chosen as the new matching criterion. FFTs are used to calculate correlations for computational speed. Different search strategies to combine and correct motion over the whole k-space are discussed and compared. In Chapter 6, we present a novel data-driven motion correction method for magnitude MR images using generative adversarial networks (GANs). GANs (pix2pix model) are implemented to reduce motion artifacts and reconstruct motion-corrupted images through adversarial training between generator and discriminator networks to estimate a motion-corrected image that is close to the reference image. The training set is made of image pairs consisting of motionless reference images and corresponding motion-simulated images. In Chapter 7, we make some observations about the research and suggest future work.

Chapter 2
MRI Motion Correction

MRI motion correction techniques can be classified into three groups: motion correction based on k-space trajectories, prospective motion correction (PMC) and retrospective motion correction (RMC). k-space trajectories are the sample patterns to fill k-space. Some k-space trajectories can enable estimating motion directly from the sample data. Prospective motion correction techniques perform a real-time update of the data acquisition strategy, which is performed by tracking object positions adaptively. Retrospective motion correction postprocesses the data and reconstructs MR images after the data is fully acquired.

This chapter is organized as follows: 2.1 motion correction based on k-space trajectories, 2.2-2.3 prospective motion correction techniques and several methods, 2.4 retrospective motion correction techniques, 2.5 autofocusing methods, 2.6 artificial neural network methods, and 2.7 advantages and limitations of PMC and RMC.

2.1 Motion correction based on k-space trajectories

Motion correction based on k-space trajectories is a type of self-navigation motion correction. PROPELLER [77] is one of the most popular k-space trajectories. PROPELLER stands for “Periodically Rotated Overlapping Parallel Lines with Enhanced Reconstruction”, which collects data in centered rectangular strips rotated around the k-space origin until filling the disc of k-space. In each strip, the same number of phase encoded lines are acquired. This sample pattern is shown in Figure 2.1.

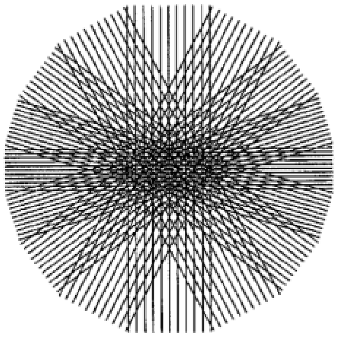

Figure 2.1: Trajectories of a PROPELLER composed of 9 strips. (Figure 2.1 is from[77].)

This sample pattern can reduce motion artifacts by oversampling the k-space center. A circle in the central k-space is generated by the overlap between strips. In-plane rotations and translations of each strip are corrected by correlation between the central circle and each strip based on Fourier transform properties. Through-plane motion can be detected by cross-correlation. To reduce the effect of through-plane motion to the final reconstruction, the strips with through-plane motion are given a smaller weight factor.

The PROPELLER trajectories can be used in undersampling methods [6]. PROPELLER is very useful in clinical applications and is implemented on all the major imaging platforms. Compared to the Cartesian sampling pattern, the acquisition time of PROPELLER is increased due to the strong oversampling in central k-space. Even if PROPELLER can detect through-plane motion, it is mainly used for 2D image motion correction.

2.2 Prospective motion correction

Prospective motion correction was first proposed by Haacke and Patrick [39]. In the past thirty years, PMC has become a popular method and is widely used in MRI motion correction. The motion correction model and several kinds of motion tracking methods are shown below.

2.2.1 motion correction strategy

If an object is in motion, the object and imaging volume should maintain a constant relationship. The strategy is achieved by obtaining tracking data of the pose (position and orientation) of the object, passing these data to the scanner with minimal delay, and adjusting the MR pulse sequences so that the imaging volume moves to follow the object [64]. Figure 2.2 shows the strategy of PMC.

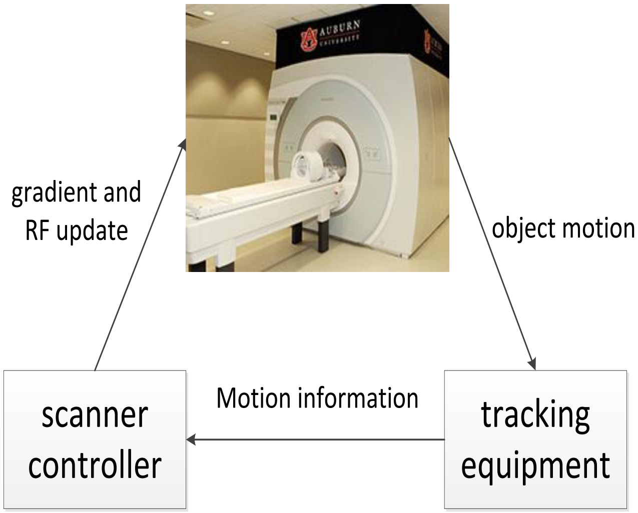

Figure 2.2: The strategy of PMC.

Rigid motion model can be described by:

$$x(t) = R(t)x_o + T(t), \tag{2.1}$$

where x_o is the original two-element position vector before motion, $x(t)$ is the position vector after motion occurs at the time point t, $R(t)$ is the rotation matrix of the imaged object as a function of time point t and $T(t)$ is the translation vector as a function of time point t. $T(t)$ can be corrected by changing receive phase and RF transmit frequency. In order to compensate for $R(t)$, the original gradient g_o should be changed to $g(t)$ as follows:

$$g(t) = R(t)g_o. \tag{2.2}$$

The frequency, phase and slice-encoding gradients for the rotated object are combined with no motion gradients. In other words, the logical gradients, which are for the actual pose of object, are represented by combinations of the physical gradients. Figure 2.3 shows the compensation.

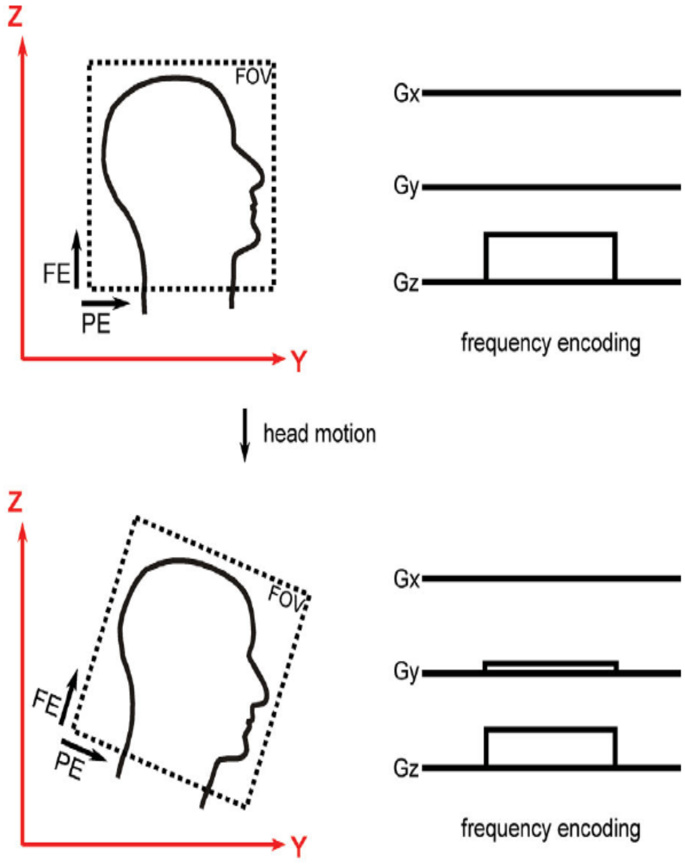

Figure 2.3: Gradients change with rotation of the head. (Figure 2.3 is from [64].)

2.2.2 motion tracking

In order to track the pose information of the object, three groups of tracking methods—field detection, optical methods and MR navigators—are used.

field detection methods

These methods were first introduced by Ackerman et al. [1]. The main idea of field detection methods is that different positions of the scanner have different magnetic field environments, which are measured to localize the positions of the object. Active markers [74, 73] or probes [10, 11], which are attached to the subject, are required to implement the measurements. These methods have some disadvantages. The equipment is always connected by wires to the scanner, which makes the patient less comfortable and makes the scan more complicated.

optical methods

The use of a camera system is one of the most popular optical methods. A camera or cameras are used to track motion of markers, which are affixed to the subject, to get the position of the subject. Camera systems include out-of-bore camera system [107, 90, 5] and in-bore camera systems [83, 3, 104]. The camera is out of the scanner systems in an out-of-bore system, which reduces the compatibility requirement with the scanner but increases the challenge of accuracy. In-bore camera systems require higher MR compatibility but can generally track motion more accurately. There are two other kinds of optical methods—laser systems [28, 29] and bend-sensitive fiber—optic tape [43]. At least one marker is required in the optical system. Cross-calibration is necessary to transform the subject position information in the coordinate system of the optical tracking system to the MRI scanner coordinate system.

MR navigators

MR navigators include two kinds of navigators: image-based navigators and k-space navigators. Image-based navigators, such as PACE [91] and PROMO [100], make use of image registration information to update the position of the subject. These allow the user to define the interesting image region for motion correction and avoid nonrigid parts of the image region like the neck. However, the acquisition time is always longer than k-space navigators, and this long acquisition time for navigators may exceed otherwise unused time in the sequence, which may produce incompatibility problems with some MRI sequences. K-space navigators, such as orbital navigators [97], spherical navigators [98] and cloverleaf navigators [93], sample the same part of k-space data repeatedly to determine rotations and translations by k-space comparison. Compared with field detection and optical methods, no marker and no additional equipment are needed for MR navigator methods. However, they require modified or additional k-space trajectories and may require extra time to scan the additional k-space trajectories. The information from MR navigators can also be used to correct motion retrospectively.

2.3 PMC methods

2.3.1 PACE and PROMO

Both PACE and PROMO are image-based prospective motion correction methods. Prospective Acquisition Correction (PACE) was first proposed by Thesen. This method is a combination of both prospective and retrospective motion correction. An image-based motion detection is used to estimate the 3D rigid motion, which can be used to adjust the position of the volume before the next volume acquisition. At the same time, retrospective correction is performed to decrease the residual volume-to-volume motion. Figure 2.4 shows the process of PACE.

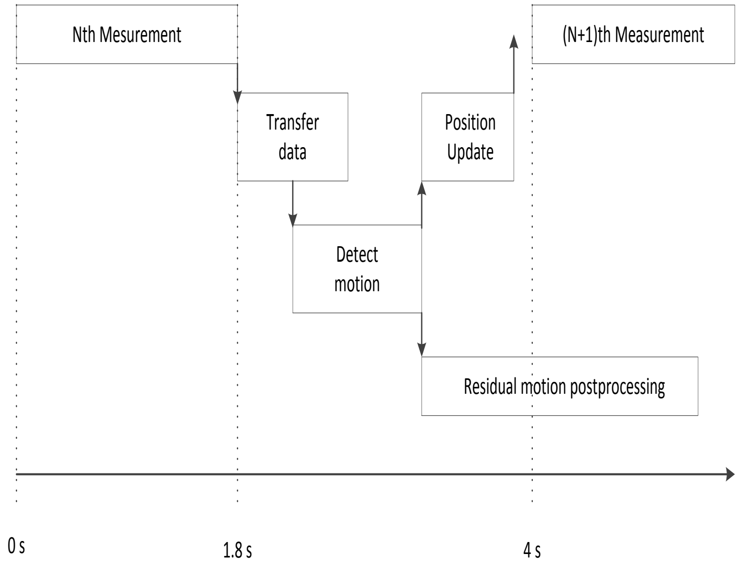

Figure 2.4: Process of PACE.

PROMO represents “PROspective MOtion correction”, is another popular motion correction method based on images. Three orthogonal 2D spiral navigators (SP-Navs) are acquired to reconstruct images. The extended Kalman filter (EKF) is used to predict and correct motion based on the reconstructed images from the spiral navigators. In order to keep the scan efficient, multiple SP-Navs and EKFs are used in the recovery time of scan sequences. Figure 2.5 shows 3D IR-SPGR sequence with SP-Navs and EKFs [100].

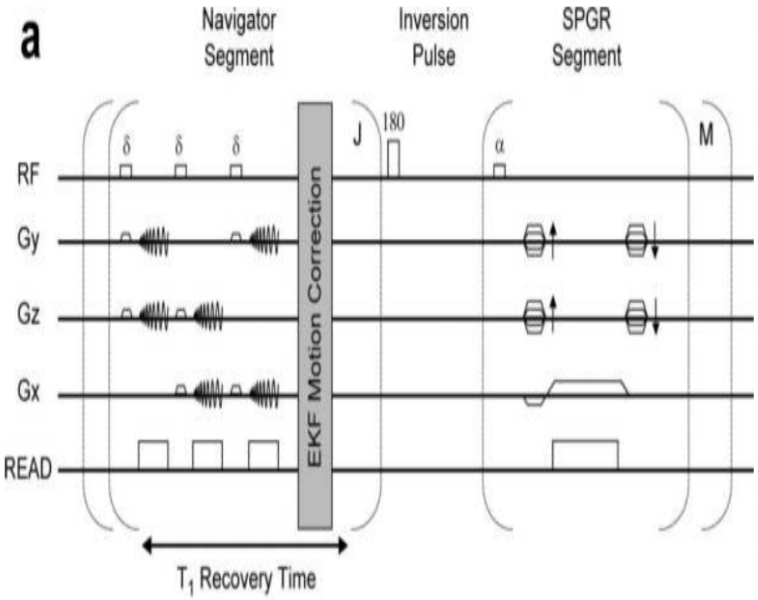

Figure 2.5: 3D IR-SPGR sequence with SP-Navs and EKF. (Figure 2.5 is from [100].)

2.3.2 SNAV

A spherical shell in k-space is sampled as a 3D spherical navigator (SNAV) echo, which is used to measure rigid motion in 3D space [98]. 3D rotation and translation of an imaged object can be detected by registration in k-space. The relationship between a reference position k-space signal at the location (k_ρ, θ, ϕ) and a new object position at the rotated coordinate frame (k_ρ, θ', ϕ') in spherical coordinates is given by:

$$S'(k_\rho, \theta', \phi') = S(k_\rho, \theta, \phi) \exp\big\{i2\pi k_\rho(\Delta x \cos\theta \sin\phi + \Delta y \sin\theta \sin\phi + \Delta z \cos\phi)\big\}, \qquad (2.3)$$

where $(\Delta x, \Delta y, \Delta z)$ are the translations in the three axis directions. k_ρ is unchanged in the rotated coordinate, so both signals are on the same shell.

The relation between a reference position (k_x, k_y, k_z) and a new translation-only object position (k'_x, k'_y, k'_z) is given by:

$$S'(k'_x, k'_y, k'_z) = S(k_x, k_y, k_z) \exp\big\{i2\pi \left(\Delta x k_x + \Delta y k_y + \Delta z k_z\right)\big\}. \tag{2.4}$$

Since k-space registration is implemented, the three rotation parameters can be found separately from the three translation parameters. The registration can be made by rotating the magnitude values of the shell to detect the rotation information, and then translation parameters can be obtained by comparing with the phase differences after rotation is corrected. Figure 2.6 shows the spherical shell and rotation k-space registration.

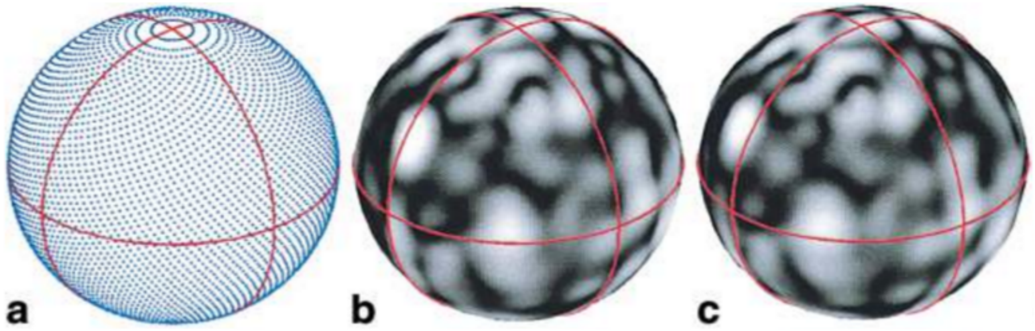

Figure 2.6: (a) Signal amplitude of spherical shell (b) before and (c) after a 12° relative rotation. (Figure 2.6 is from [98].)

2.4 Retrospective motion correction

Retrospective motion correction refers to modifying k-space or image data during image reconstruction, after all data is acquired [34]. The process of acquisition is independent of motion. RMC includes three main groups: self-navigation motion tracking methods to calculate motion information, autofocusing methods based on evaluation of image quality, and motion correction by training neural networks. Self-navigation motion correction methods rely on Fourier properties by taking advantage of overlapping k-space data to track motion [15, 69, 9]. Autofocusing methods do not rely on a specific data sample pattern, equipment or sequence design. These approaches assume a rigid body or deformable object motion model and estimate motion model parameters by iterative optimization of an image quality metric when the raw k-space data are modified according to the motion model [8]. Artificial neural network methods establish the mapping relationship between the motion-corrupted images and the no-motion images by training a large number of related images, and estimate motion-corrected images from motion-corrupted images.

In the next sections, we will discuss several autofocusing methods and artificial neural network methods in detail.

2.5 Autofocusing methods

2.5.1 automatic correction of motion artifacts in Magnetic Resonance images using an entropy focus criterion

To our knowledge, the first autofocusing MRI motion correction method was proposed by Atkinson et al. [8]. An image entropy focus criterion was used to correct motion-corrupted MR images. Patient motion can be described by a motion trajectory, which is assumed to be rigid motion as a function of time. Continuous movement is discretized as a series of motion nodes, and in each node the motion is constant. Each node corresponds to the acquisition of one k-space line or one group of k-space lines. The starting point for this trajectory is zero motion corresponding to one group of k-space lines, while the motions in other groups of k-space lines are corrected by assessing the image quality, named entropy focus criterion. The motion estimation is modified with trial-and-error iteratively to obtain the best quality image.

The entropy of an image E is defined as:

$$E = -\sum_{i=1}^{N} \frac{|p_i|}{p_{\text{total}}} \ln\left(\frac{|p_i|}{p_{\text{total}}}\right), \tag{2.5}$$

where p_i is the pixel value of the image, and N is the total number of pixels of the image. p_{total} is given by:

$$p_{\text{total}} = \sqrt{\sum_{i=1}^{N} p_i^2}. \tag{2.6}$$

Entropy minimization prefers high contrast and increasing the number of dark pixels, while motion tends to do the opposite by creating ghosts and blurring images in the dark regions. For an image, when all the image energy is in one pixel and the other pixel values are 0, E equals 0, which is the minimum of (2.5). But when all the pixel values in a 256×256 images are equal, the image entropy E is around 1420, which is the maximum of (2.5) for that image size.

The optimization strategy is similar to a multi-resolution search scheme. The readouts within the acquisition are grouped into several segments, and each segment includes the same number of non-overlapping MRI k-space lines. In order to illustrate this clearly, we take 256 readouts as an example. The k-space is separated into 16 segments, each having a length of 16 k-space lines. The 16 segments are grouped into two parts—lower part and upper part. Each part consists of 8 segments. The lower part is from the scan center to the end of the scan, and the upper part is from the scan center to the start of the scan. The first segment of the lower part consists of 16 k-space lines from the scan center (low frequency) towards the end of the scan (high frequency). This segment has trial translations in both the phase encoding and frequency encoding directions $\{-N, -(N-1), -1, 0, 1, (N-1), N\}$ (N is the searching range), with a total of $(2N+1) * (2N+1)$ combinations for this segment. For each combination, preserving other segments unchanged, the image entropy is calculated by (2.5). The lowest entropy of the combination is accepted, and the motion of the first segment of the lower part is corrected corresponding to the combination. The subsequent segments of the lower part are considered similarly in turn. The segments of the upper part are calculated in the same way. This process is repeated, and the segment length decreases by two k-space lines in each iteration. In this way the gross motions are determined first and gradually refined.

This method has high computational load due to using a trial-and-error approach. In addition, the optimization strategy makes the search more likely to be trapped in local minimum.

2.5.2 blind retrospective motion correction of MR images

To reduce computational load for 3D rigid motion, an analytical gradient-based motion correction (GradMC) algorithm was proposed by Loktyushin et al. [59]. A parameterized 3D motion-corrupted k-space model was proposed. Entropy of the gradient of the image is used as the focus criterion in this method. The motion assumption is similar to [8] but in 3D space. Quasi-Newton and Broyden-Fletcher-Goldfarb-Shanno is used to optimize the cost function iteratively.

Entropy of gradient of an image is defined as:

$$\phi(I) = H(D_x I) + H(D_y I), \tag{2.7}$$

where D_x and D_y are the difference matrices in horizontal and vertical directions and $H()$ is defined as:

$$H(p) = -v^T \ln v, v = \sqrt{\frac{p \odot p^*}{p^H p}}, \tag{2.8}$$

where $\odot$ is the point-wise product of two vectors, p is the pixel vector of the image I, $*$ represents the complex conjugate, and H represents complex conjugate transpose.

Coarse to fine optimization strategy is used. The coarse image formed by only lower frequency k-space data is corrected first, and then a finer image is formed by adding a higher-frequency segment. All the k-space lines that formed the finer image are corrected based on the focus criterion. The process iteratively covers all the k-space lines and corrects the whole k-space data, which is shown in Figure 2.7.

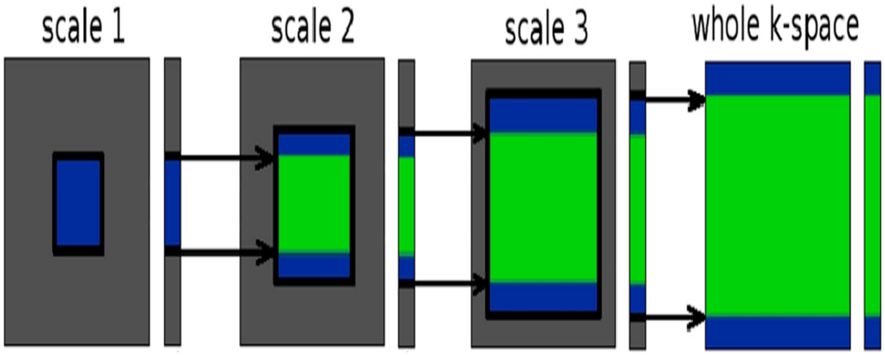

Figure 2.7: Optimization strategy of Blind Retrospective Motion Correction of MR Images. The k-space data is processed from center (low frequency part) to the whole k-space to optimize motion parameters using coarse to fine optimization. (Figure 2.7 is from [59].)

Since the algorithm performs line-by-line 6-parameter correction, the calculation load is very high. Hence, a highly parallel implemented GPU version gradient-based motion correction optimization strategy is used. A similar idea was used to correct nonrigid motion by correcting each rigid motion patch [60].

2.5.3 nonrigid motion correction in 3D using autofocusing with localized linear translations

An autofocusing motion correction method based on “Butterfly” navigators to reduce calculation load and correct nonrigid motion was introduced by Cheng et al. [19]. The different motion on each small patch of image is approximated by a translation. “Butterfly” navigators provide possible translational motion information to reduce the search range. Localized entropy of the gradient of the image is used as the focus criterion. Based on this localized autofocusing framework, a new motion correction method combined with other sample patterns and compressed sensing was proposed [20].

2.6 Artificial neural network methods

Artificial neural networks (ANNs) are widely used in machine learning. In general, an ANN is made of a collection of connected computational units, called artificial neurons, which simulates the biological neurons. Artificial neurons are arranged in layers. Different network structures are formed by different number, arrangements and connections of layers, or different orders of functional layers. A loss function is a measure function to compare the real output (the labeled output from the training set) with network output. An ANN is trained to minimize a loss function using a labeled training set. The details of ANNs will be discussed in the Chapter 6.

Neural networks are widely used in the MRI field: image reconstruction [105, 95, 82], image denoising [87, 13, 12], image super-resolution [109, 57, 17], and image segmentation [18, 42, 21]. The history of using neural networks to correct MRI motion is relative short. In general, these methods require pairs of images as the training set: motionless images and corresponding motion-corrupted images but using different network structures and loss functions. Loktyushin et al. [61] proposed a motion correction method using convolutional neural networks. Duffy et al. [24] used a modified HighRes3dNet (HR3DNet) [56] to correct MRI head motion. Pawar et al. [75] implemented an encoder-decoder convolutional neural network to restore motion-blurred images. Armanious et al. [7] proposed a novel framework called MedGAN based on GANs for medical image translation.

2.7 Advantages and limitations of PMC and RMC

In this section, we discuss the advantages and limitations of PMC and RMC separately and at the end discuss one hybrid motion correction method.

2.7.1 advantages of PMC

data consistency and uniform sampling

In PMC, the FOV (field of view) follows the object tightly, so the object cannot move out of the imaging volume in normal situations. Uniform sampling can be kept in PMC; on the other hand, RMC cannot perform uniform sampling, especially in the case of large rotation.

through-plane motion

Spin-history effects occur when the object moves in and out of the imaging slice [33]. Through-plane motion can disrupt the steady state in one imaging slice, leading to signal fluctuations in conventional imaging. PMC can correct the through-plane motion to reduce the spin-history effects.

real-time imaging

Imaging time is an important factor in research and clinical applications. Some modern PMC can provide real-time imaging.

calculation load

Calculation load is relatively low for PMC, and there is no additional calculation performed for the image reconstruction.

2.7.2 limitations of PMC

tracking motion error effect

The performance of PMC is determined by the acquisition of reliable and accurate tracking data. Inaccurate pose data or noisy data can corrupt the image information. Cross-calibration errors may be fatal for optical PMC.

additional hardware

For optical and field detection methods, additional hardware is needed to track the motion, which makes the whole system complicated and expensive.

sequence adjustments

For the MR-navigator methods, some MRI sequences have to be changed to add the navigators, which may increase the scan time and lead to complicated sequence modification. In some cases, navigators are not compatible with sequences.

marker attachment

Markers have to be attached to the object securely to track the motion, which results in inconvenience and discomfort for the subject. If markers move, erroneous updates will be applied, which may destroy image quality.

2.7.3 advantages of RMC

simple system

For autofocusing methods, no additional hardware, no gradient update, no modification of MRI sequences and no markers are needed. For neural network methods, there are no specific requirements for the software and hardware of scanners. A basic MR system is enough for RMC. Accounting for the equipment cost and operation complexity, RMC is suitable for clinical use.

real-time motion correction

Compared with other RMC methods, we propose a new motion correction method based on fast robust correlation that can provide real-time motion correction. For artificial neural network methods, if the training time is ignored, the motion correction can be accomplished in real time.

no preparation required

Because no special sequences or hardware is required, no special preparation is required prior to or during acquisition. A decision about performing motion correction can be made after the data is acquired.

2.7.4 limitations of RMC

through-plane motion

2D RMC cannot correct through-plane motion, which may lead to motion correction errors and induce image artifacts.

non-realistic images

Non-realistic motion-corrected images may be generated by artificial neural networks methods. It is hard to eliminate this phenomenon, which is determined by the nature of the artificial neural network.

nonuniform samples

According to the property of Fourier transforms, correction of large angle rotations may result in nonuniform sampling and local Nyquist violations, which is shown in Figure 2.8.

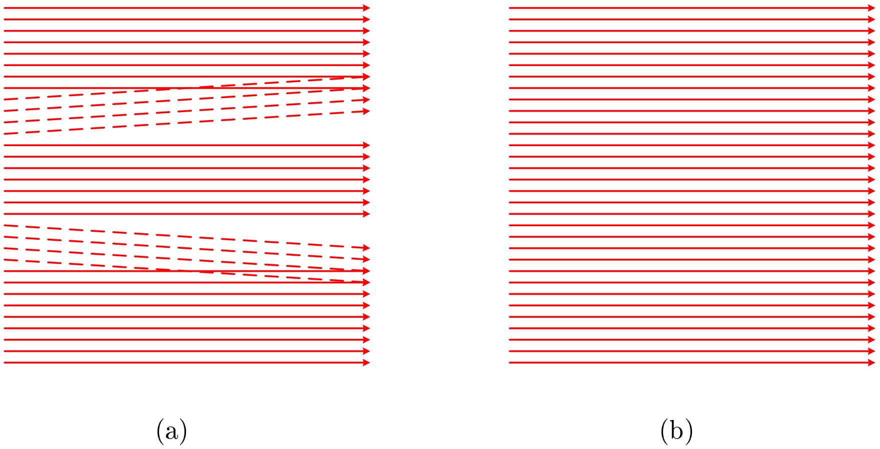

Figure 2.8: (a) Sample locations after RMC correction for rotation object. (b) Sample locations after PMC for rotation object.

calculation load

The calculation load is relatively high for previous RMC methods. The most common way to reconstruct images is to iteratively update motion parameters.

local minima

RMC are easily trapped in local minima, due to the vast motion search space and imperfect optimization strategies.

A combination of PMC and RMC is possible and some of the limitations can be addressed partially [14, 65]. Aksoy proposed a motion correction method to combine prospective optical-based motion correction with removal of residual motion artifacts by entropy-based retrospective autofocusing [2]. In general, scanner-camera cross-calibration is the key factor with optical prospective motion correction, because a small error in the cross-calibration can result in wrong position adjustment for the scanner and induce image artifacts. However, for this hybrid method, the requirement of cross-calibration accuracy is decreased, and high-quality images may still be obtained, because the autofocusing motion correction method is applied after data is acquired. The details of this method will not be discussed here.

Chapter 3

Image Registration

Image registration is closely related to some motion correction methods and our proposed methods. In this chapter, some basic image registration concepts are first discussed. Image registration is defined as a process by which different sets of data are transformed into the same coordinate system. This process sets one image as the target (also called the fixed image, or the reference image), and implements a transformation model to the other image (also called the moving image, the floating image, or the source image) to match the target image.

Image registration is a basic technology in image processing. The applications can be generally classified into three fields [112].

different times. Images of the same object are acquired at different times, and the purpose of registration is to find the changes of the object, such as motion tracking, landscape changes and tumor evolution.

different views. Images are obtained from different viewpoints at the same time, and the purpose of registration is to get a bigger view of images, such as remote sensing and 3D image reconstruction.

different sensors. Images are acquired from different sensors for the same object, and the purpose of registration is to catch and fuse more details of the same object, such as remote sensing, multiple sensor fusion, MR-CT, and MR-SPECT fusion.

Figure 3.1, Figure 3.2 and Figure 3.3 give examples of different times, different views, and different sensors image registration.

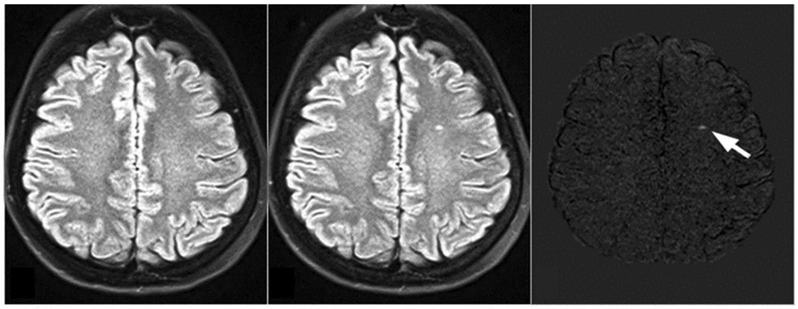

Figure 3.1: Different times brain images registration to detect a lesion. (This image is from the link https://thebestphotos.eu/detection-of-focal-longitudinal-changes-in-the-brain-by.html)

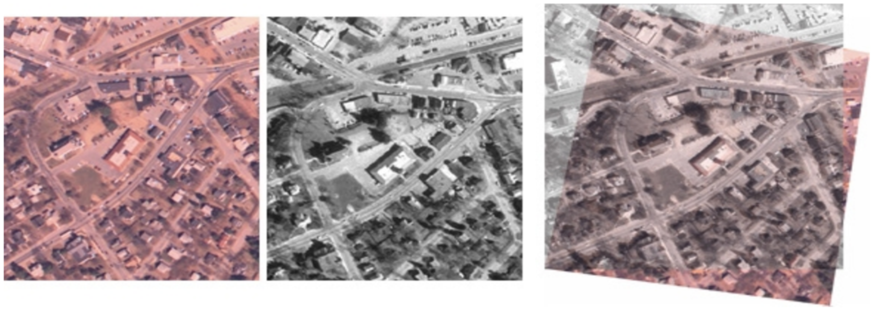

Figure 3.2: Different views aerial images registration to extend the view. (This image is from MathWorks website Image Registration section, and the link is https://www.mathworks.com/discovery/image-registration.html)

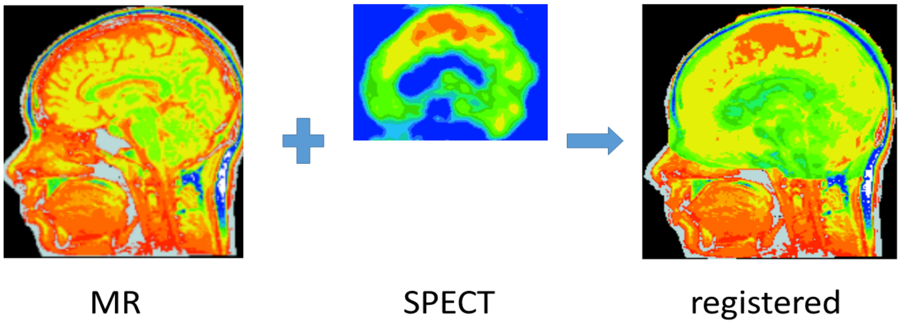

Figure 3.3: Different sensors brain images registration to fuse images. (This image is from UCF Medical Image Computing (CAP 5937) slices (Spring 2016), and the link is http://www.cs.ucf.edu/~bagci/teaching/mic16/lec15.pdf)

The image registration methods can be classified into two groups: area-based registration and feature-based registration. The process of both registration methodologies show in Figure 3.4 and Figure 3.5.

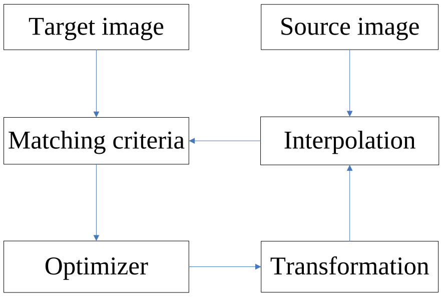

Figure 3.4: The steps of area-based registration methods

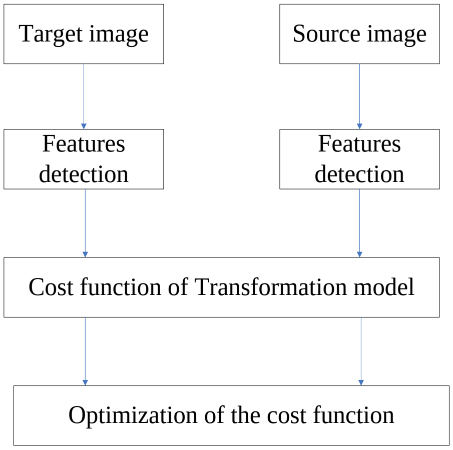
Target image
Source image
Features detection
Features detection
Cost function of Transformation model
Optimization of the cost function

Figure 3.5: The steps of feature-based registration methods

In general, a registration algorithm, whether area-based or feature-based, can be decomposed into three parts:

transformation models. The way that a source image can be changed to match the target image.

matching criteria. The similarity measures of two images to be matched.

optimization methods. Algorithms to maximize or minimize the matching criteria.

For the feature-based image registration, one more step—feature detection—is needed. Considering the relation to the proposed methods, we only discuss area-based image registration here. This chapter is organized as follows: 3.1 transformation models, 3.2 matching criteria, and 3.3 optimization methods.

3.1 Transformation models

A transformation model defines how one image can be deformed to align with the other image, which is an important step for registration. The choice of transformation model depends on the image registration application and the nature of the image data, which influences the rest of the registration steps. The transformation model has two functions. First, it improves the similarity of the images by defining the source image move relative to the target image. Second, it defines the source image interpolation if necessary. In general, transformation models can be classified into three primary groups: rigid, affine and non-rigid models.

The rigid transformation model is a basic and widely used model in image registration. Rigid transformation preserves the Euclidean distance for each point pair in a Euclidean space, which is also called a Euclidean transformation. In two-dimensional space, the model is always defined by three parameters: two translation parameters and one rotation parameter, which is described as three degrees of freedom. These parameters are applied to a vector locating a point in the source image to find its location in the target image. Different orders of rotation and translation operations may have different transformation model representations [31, 37]. For rotation before translation, the transformation model is given by:

$$\begin{bmatrix} x' \\ y' \\ 1 \end{bmatrix} = \begin{bmatrix} \cos\theta & \sin\theta & t_x \\ -\sin\theta & \cos\theta & t_y \\ 0 & 0 & 1 \end{bmatrix} \begin{bmatrix} x \\ y \\ 1 \end{bmatrix}, \tag{3.1}$$

where t_x and t_y specify the translations along the x and y axes, and θ is the angle of rotation at the center of the image.

The corresponding model for translations before rotation is given by:

$$\begin{bmatrix} x' \\ y' \\ 1 \end{bmatrix} = \begin{bmatrix} \cos\theta & \sin\theta & t_x\cos\theta + t_y\sin\theta \\ -\sin\theta & \cos\theta & -t_x\sin\theta + t_y\cos\theta \\ 0 & 0 & 1 \end{bmatrix} \begin{bmatrix} x \\ y \\ 1 \end{bmatrix}. \tag{3.2}$$

In three-dimensional space, the model includes six parameters: three translation parameters and three rotation parameters. Here we just show the representation for rotations before translations:

$$\begin{bmatrix} x' \\ y' \\ z' \\ 1 \end{bmatrix} = \begin{bmatrix} \cos\omega\cos\phi & \cos\theta\sin\phi + \cos\phi\sin\omega\sin\theta & \sin\phi\sin\theta - \cos\phi\sin\omega\cos\theta & t_x \\ -\cos\omega\sin\phi & -\sin\theta\sin\omega\sin\phi + \cos\theta\cos\phi & \sin\theta\cos\phi + \sin\phi\sin\omega\cos\theta & t_y \\ \sin\omega & -\sin\theta\cos\omega & \cos\theta\cos\omega & t_z \\ 0 & 0 & 0 & 1 \end{bmatrix} \begin{bmatrix} x \\ y \\ z \\ 1 \end{bmatrix}, \tag{3.3}$$

where t_x, t_y and t_z specify the translations along the x, y and z axes, and θ, ω and ϕ are the angles rotation around the x, y and z axes.

A rigid transformation model is mainly used in two ways. One is to model rigid structure motion, such as head MRI. The other is for pre-registration of non-rigid structures, that is then followed by more complicated non-rigid registration based on the pre-registration.

An affine transformation model can permit translation, rotation, scaling and shearing deformations [49]. This model can align images with perspective distortions. Figure 3.6 shows this model. The transformed coordinates are given by:

$$\begin{bmatrix} x' \\ y' \\ z' \\ 1 \end{bmatrix} = \begin{bmatrix} a_{11} & a_{12} & a_{13} & t_x \\ a_{21} & a_{22} & a_{23} & t_y \\ a_{31} & a_{32} & a_{33} & t_z \\ 0 & 0 & 0 & 1 \end{bmatrix} \begin{bmatrix} x \\ y \\ z \\ 1 \end{bmatrix}, \tag{3.4}$$

where a_{11}, a_{12}, a_{13}, a_{21}, a_{22}, a_{23}, a_{31}, a_{32} and a_{33} specify rotation, scaling and shearing deformations, and t_x, t_y and t_z specify the translations.

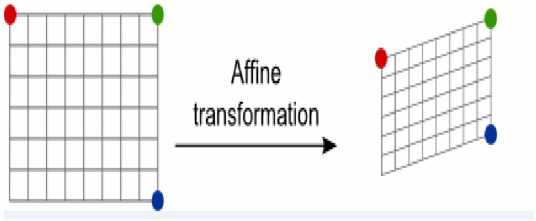

Figure 3.6: Affine transformation model, the parallel lines keep parallel after an affine transformation.

Non-rigid registration is a popular topic in recent research. One commonly used and important non-rigid registration method is a group of splines technique [89, 53, 54]. In splines registration methods, corresponding control points are defined in both target and source images to calculate distance between these control points by spline function. Thin-plate splines [25] and B-splines [103] are the most widely used among the spline methods. Thin-plate splines registration is a global method, which means each control point in the thin plate has a global influence on the transformation model. If the position of one control point changes, the transformation model will change, and the whole transformed image will change. By contrast, B-splines is a local registration method, which is defined in the vicinity of each control point. So one control-point position change will only affect transformation in the neighborhood of the point, not the whole transformed image. Hence, it is more robust. Figures 3.7 and 3.8 show the thin-plate splines and B-splines registration.

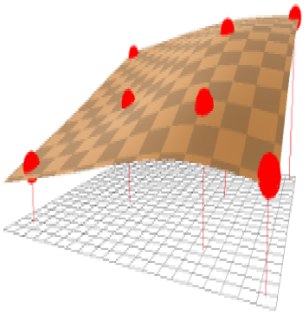

Figure 3.7: A thin-plate spline that passes through a set of control points. (Figure 3.7 is from the link `http://elonen.iki.fi/code/tpsdemo/`.)

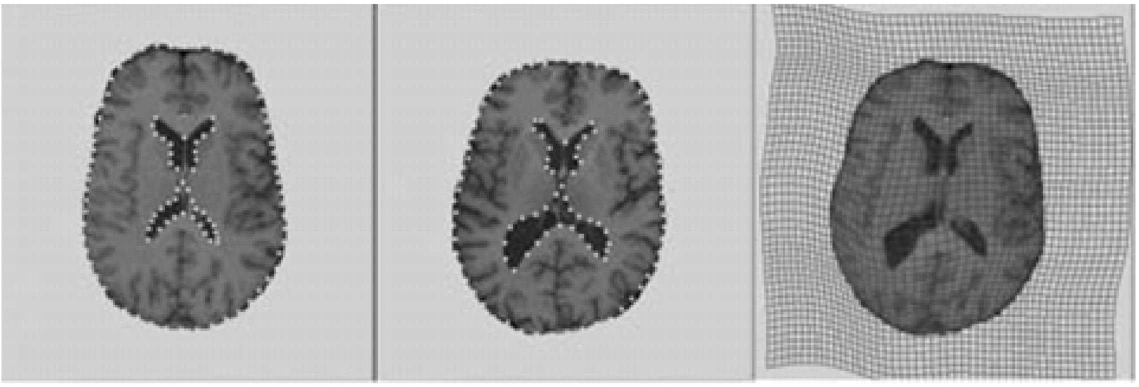

Figure 3.8: Left: source image. Middle: target image. Right: deformed source image through B-splines registration. (Figure 3.8 is from [103].)

3.2 Matching criteria

Area-based matching criteria align images by evaluating the whole image domain pixel values. This strategy is widely used when image features are not salient or the features are hard to detect, such as some kinds of medical image registration. Since the whole data is used, the registration is more robust, and error pixels do not have much effect on the final transformation model. However, computational expense is increased when the size of the image is large.

The area-based matching criteria include two similarity measures: intensity-based and frequency-based.

Intensity-based similarity measures can be divided into three groups: based on intensity differences, based on intensity cross-correlation and based on information theoretic approaches [22, 44].

Intensity difference methods usually use the sum of squared or absolute differences (SSD or SAD) as a matching criterion. In order to use the intensity differences similarity measure, the same structures of the target and source images should have similar intensity values. Thus, the minimum of SSD or SAD means two images matched. SSD and SAD are given by:

$$SSD = \frac{1}{N} \sum_{x \in \Omega_{T,S}} \Big[T(x) - S\big(t(x)\big) \Big]^2, \tag{3.5}$$

$$SAD = \frac{1}{N} \sum_{x \in \Omega_{T,S}} \Big| T(x) - S\big(t(x)\big) \Big|, \tag{3.6}$$

where $T(x)$ is the intensity of voxel x in the target image and $S\big(t(x)\big)$ is the intensity of the corresponding voxel in the source image through the estimation of the transformation function $t(x)$, $\Omega_{T,S}$ is the overlap region of the target and the source images and N is the number of voxels in this region.

The cross-correlation (CC) method has also been used as an image similarity measure. The assumption behind CC is that there is a linear intensity relation between the two images. Compared with SSD, the maximum of CC means two images are correctly aligned. CC is given by:

$$CC = \frac{\sum_{x \in \Omega_{T,S}} \Big(T(x) - \bar{T} \Big) \Big(S\big(t(x)\big) - \bar{S} \Big)}{\sqrt{\sum_{x \in \Omega_{T,S}} \Big(T(x) - \bar{T} \Big) \sum_{x \in \Omega_{T,S}} \Big(S\big(t(x)\big) - \bar{S} \Big)}}, \tag{3.7}$$

where $\bar{T}$ is the mean voxel intensity of the target image and $\bar{S}$ is the mean voxel intensity of the source image.

SSD and CC are used for mono-modal registration, but for multi-modal, registration information theoretic approaches are the most popular.

Joint distribution of the Shannon entropy provides one way to measure the alignment [78], which is given by:

$$H(T,S) = -\sum_{t,s} p_{T,S}(t,s)\log p_{T,S}(t,s), \tag{3.8}$$

where $p_{T,S}(t,s)$ is a joint probability density function of target and source images in the overlap region. The entropy is low when the distribution has concentric peaks, and it is high when the distribution is more uniform. So the strategy is to minimize the joint entropy to match the images. The joint probability density function is generated from a joint histogram of the target and source images.

When joint distribution of the Shannon entropy is used alone, misregistration can occur. For example, when two images only have one piece of background overlaps, the joint histogram has only one sharp peak, and the joint entropy has a low value that leads to an uncorrected registration. Mutual information (MI) [66, 99] is an effort to solve this problem. MI measures the amount of information in the overlapping volume by the marginal entropy of the individual image being registered together with the joint entropy, which is given by:

$$MI(T,S) = H(T) + H(S) - H(T,S), \tag{3.9}$$

where $H(T)$ and $H(S)$ are the marginal entropies of each image. Eq 3.10 and Eq 3.11 give the overlap region marginal entropy of each image.

$$H(T) = -\sum_{t} p_T(t)\log p_T(t) \qquad \forall T(x) = t | x \in \Omega_{T,S}, \tag{3.10}$$

$$H(S) = -\sum_{s} p_S(s)\log p_S(s) \qquad \forall S(x) = s | x \in \Omega_{T,S}. \tag{3.11}$$

MI can be further expressed as:

$$MI(T,S) = H(T) + H(S) - H(T,S) = \sum_{t,s} p_{T,S}(t,s) \log \frac{p_{T,S}(t,s)}{p_T(s) p_S(t)}. \tag{3.12}$$

For the previous example, the marginal entropies will have low values when the overlapping region only includes background, and they will have high values when the overlapping region includes sharp structures. The marginal entropy terms provide a tradeoff with the joint entropy.

All three previously discussed similarity measures are in the spatial domain, but there is also a group of methods whose similarity measures are defined in the Fourier domain [46, 32]. If data is processed more easily in the frequency domain or an acceleration of the computation speed is needed, Fourier-domain methods can be a more powerful tool. This group of methods is a natural fit with MRI, because the image data is acquired by sampling in the Fourier domain (k-space). The phase correlation method (PCM) is the most common method in this group. According to the Fourier shift property, a linear phase difference in the Fourier transform of two images comes from a translation of the images, which is given by

$$F_S(k,l) = F_T(k,l) \exp\bigl\{-j(kt_x + lt_y)\bigr\}, \tag{3.13}$$

where F_S and F_T are the Fourier transform of source and target images. (k,l) are the Fourier domain coordinates.

The normalized cross-power spectrum is used to calculate phase correlation matrix, which is given by:

$$Q(k,l) = \frac{F_T(k,l) F_S^*(k,l)}{\bigl|F_S(k,l) F_S^*(k,l)\bigr|} = exp\bigl\{-j(kt_x + lt_y)\bigr\}. \tag{3.14}$$

PCM is robust against frequency-dependent noise and time-varying illumination disturbances. However, PCM is used only for registration of translations of images.

3.3 Optimization methods

Optimization is required to find the transformation to best align two images, which means finding the minimization or maximization of similarity measures. A good optimizer should be reliable and quick to find possible solutions. Different registration problems require different optimizers.

The similarity measure of registration can be accounted as an n-dimensional function, where n is the number of parameters of the transformation model. In order to find the n parameters to minimize or maximize this function, iterative optimization algorithms are the most common strategy.

In general, optimizing n parameters follows an update below:

$$s_{i+1} = s_i + \lambda_i g_i(s_i), \tag{3.15}$$

where s is the vector of n parameters of a similarity measure function, λ is the step length, g is the search direction, and i defines the number of the iteration.

Typical methods to update n parameters include: gradient descent (GD), conjugate gradient (CG), Quasi-Newton (QN), Levenberg - Marquardt (LM) and Gauss-Newton (GN) methods [89]. The main difference among these algorithms is how to find the next step search direction, namely g. The equations of the above algorithms are shown in Table 3.1.

Table 3.1: Search directions of different algorithms

Algorithms	Search directions
GD	$g = -\nabla_s(s)$
CG	$g = -\nabla_s(s_i) + \beta_i g_{i-1}$
QN	$g = -\hat{H}^{-1}(s)\nabla_s(s)$
LM	$g = -\big(\hat{H}^{-1}(s) + \alpha I\big)\nabla_s(s)$
GN	$g = -\big(J^T(s)J(s)\big)^{-1}\nabla_s(s)$

A multi-resolution strategy is generally used in these iterative algorithms, which is also known as a coarse-to-fine strategy [72]. First, both the target and the source images are down-sampled. Then these two down-sampled images are aligned. Second, the transformation parameters from the last step are used as the initial guess for higher-resolution images, which come from the original images with a smaller downsampling rate. So the registration is from lower- to higher-resolution images until the original resolution is reached. In each step, the parameters found in the previous step are used to obtain the initial guess of the current step. This strategy can avoid the local minimum problem and increase computational speed.

Chapter 4

An Efficient and Robust Autofocusing MR Image Motion Correction Method using Global Motion Estimation

Autofocusing motion correction methods are one kind of retrospective MRI motion correction method. These methods assume a parameterized motion model and estimate the model parameters by iterative optimization of an image quality metric, called a focus criterion. Motion is corrected after the raw k-space data are modified according to the optimized model parameters. Implementing these methods does not require additional hardware, gradient update, modification of MRI sequence or markers attached on subjects. However, due to the vast size of the search space, autofocusing methods always have two challenges: high calculation load and local minima.

In order to address the two challenges, a new autofocusing motion correction algorithm is proposed in the chapter. We propose to use multiple linear-motion initializations and joint refinement of a global model to decrease and constrain the search space. In the first step, k-space is divided into several segments based on acquisition order. Linear motion is assumed and searched in each segment to get initial motion parameters. In the second step, several control points are chosen on the piecewise linear initial approximation, and then a piecewise cubic Hermite interpolation polynomial is fitted from the control points to obtain smooth motion curves. The motion curves are refined by optimizing a focus criterion. These strategies make the proposed algorithm efficient and robust. Different focus criteria are compared under the proposed method. To further improve computational efficiency, golden-section search is used to estimate rotation, and two map data structures are applied to store calculated data. Simulations and experimental results demonstrate that the proposed algorithm can effectively and efficiently correct motion in MR images.

This chapter is organized as follows: 4.1 motion model and acquisition assumption, 4.2 the problem of previous search strategies, 4.3 focus criteria, 4.4 two steps of the proposed method, 4.5 golden-section rotation search, 4.6 map data structure, 4.7 rotation and translations interpolation methods, 4.8 simulations, 4.9 experiments, and 4.10 discussion.

4.1 Motion model and acquisition assumption

In this chapter, the motion is assumed to be two-directional translations and one rotation in a 2D plane. It is assumed that the x axis corresponds to the frequency encoding direction and the y axis corresponds to the phase encoding direction. The acquisition time gap of different k_{phase} lines is much longer than the duration of the frequency encoding (acquisition of one k_{phase} line). So the motion during the frequency encoding (one single k_{phase} line) is much smaller than the inter-line (different k_{phase} lines) motion, which means intra-line motion can be assumed negligible. The basic unit for motion correction in this chapter is chosen to be a single k_{phase} line, which means we only consider motion between different k_{phase} lines. Within each k_{phase} line, the object is modeled as stationary.

The motion parameters Δx, Δy and Δr corresponding to x and y translations and rotation angle are a function of k_{phase}. Therefore, the motion correction is essential to estimate a total of N_{phase} 3D vectors M, where N_{phase} is the number of k_{phase} lines. The motion parameters can be given by:

$$M(k_{\text{phase}}) = \big(\Delta x(k_{\text{phase}}), \Delta y(k_{\text{phase}}), \Delta r(k_{\text{phase}})\big), \tag{4.1}$$

This motion model is shown in Figure 4.1.

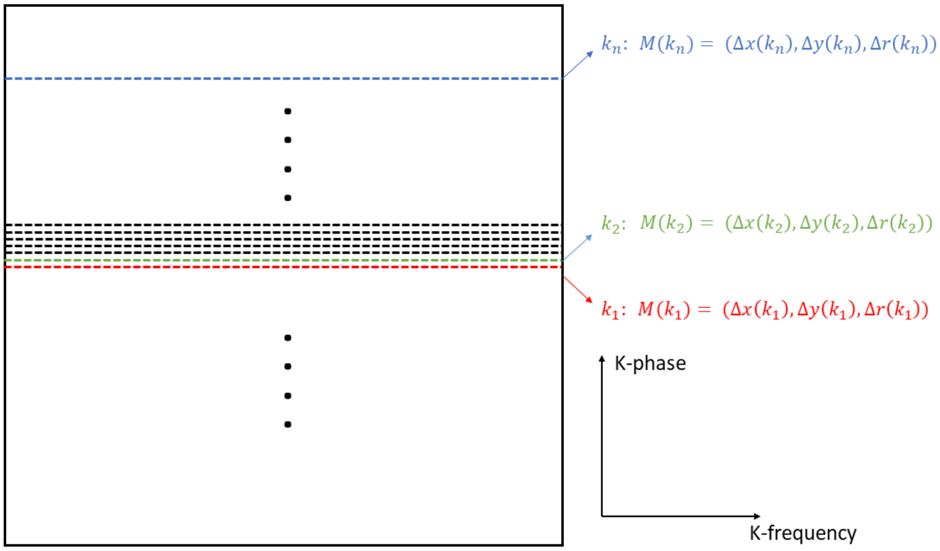
k_n: $M(k_n) = (\Delta x(k_n), \Delta y(k_n), \Delta r(k_n))$
k_2: $M(k_2) = (\Delta x(k_2), \Delta y(k_2), \Delta r(k_2))$
k_1: $M(k_1) = (\Delta x(k_1), \Delta y(k_1), \Delta r(k_1))$
K-phase
K-frequency

Figure 4.1: The motion model of the proposed method. in k-space, each dash line is one k_{phase} line. Different k_{phase} lines have their own motion parameters $(\Delta x, \Delta y, \Delta r)$. Red, green and blue are three k_{phase} lines with three different sets of motion parameters.

4.2 Previous search strategies

In general, the previous search strategies can be classified into two groups. One is to search one segment of k-space data, which includes several neighboring k-space lines, while keeping the remaining k-space lines unchanged. Then a different segment is searched until all segments covering the whole k-space are corrected. After each iteration, the size of the segments is reduced to refine motion. The other strategy is to preserve the central k-space part as the reference and then detect and correct the motion of neighboring peripheral k-space segments. The motion-corrected peripheral k-space segments are combined with the central k-space part to form a new reference, and further peripheral k-space segments are corrected until the whole k-space is covered.

We found that neighboring lines in k-space have a strong relationship, and the motion detection of one segment may not correspond to the average motion of all the lines in the segment when the segment size is smaller than a certain number. Sometimes the motion estimate of a segment matches the motion of the nearest line to the reference segment rather than matching the average motion of the k-space segment to the reference. Due to the strong impact of the neighboring line, the motion of the whole segment may not be corrected properly, which may result in the cost function being trapped in local minima, which is shown in Figure 4.2. In order to overcome this problem and take advantage of the strong relationship between the neighboring lines, a new search strategy based on global motion estimation is proposed in the next section.

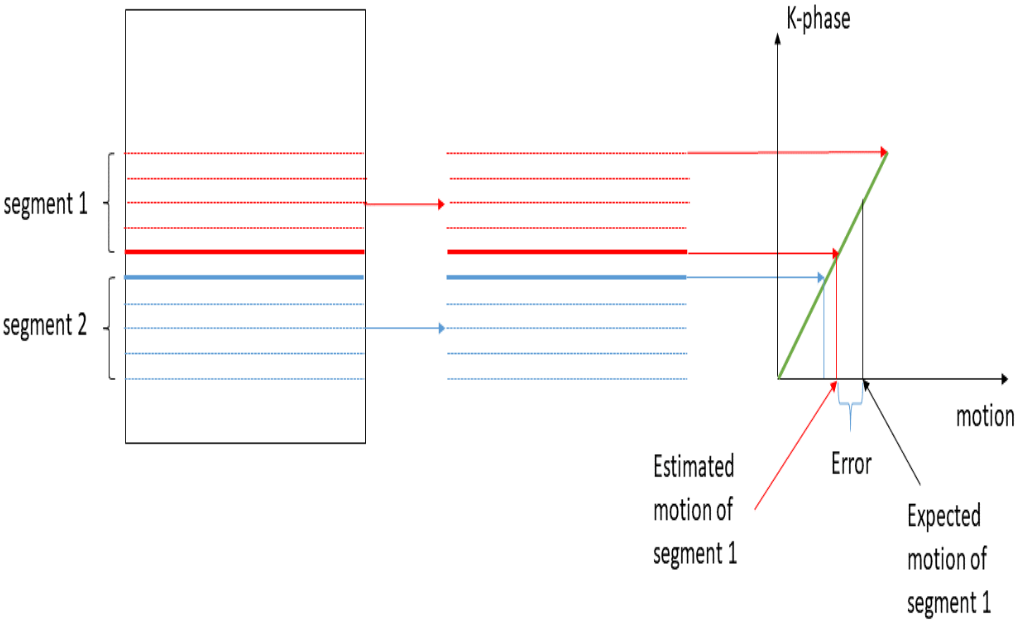

Figure 4.2: The strong relationship between neighboring lines results in motion estimation error. Segment 1 and segment 2 are two neighboring segments in k-space and the green solid line gives the real motion for each k-space line of the segment 1 and the segment 2. Due to the strong bond between the red and blue thick solid lines, the estimated motion of the segment 1 is dominated by the red thick solid line, which results in the errors for other lines in the segment 1.

4.3 Focus criteria

The focus criterion is important for image evaluation in autofocusing methods. Considering accuracy and efficiency, an ideal criterion should satisfy three conditions: first, the criterion value can measure the image quality correctly; secondly, the extremum corresponds to the best image quality. Thirdly, the criterion should be easy calculated. Many focus criteria have been proposed [68] that general meet the above conditions. We cannot provide theoretical proof of which is the optimal criterion under the proposed method, but we can draw a well-grounded conclusion based on empirical performance. Image entropy and different kinds of entropy of the gradient of image are the most popular criteria for autofocusing methods [68, 8, 59, 19]. Based on [68], the entropy of one-directional gradient along the phase-encoding direction is the best criterion. But this conclusion relies on certain evaluation rules, which may not be suitable for the proposed motion correction method. To our knowledge, the same focus criterion may perform differently under various motion correction methods. So in this chapter, the image entropy (Eq 4.2), the entropy of the one-directional gradient of image along the phase-encoding direction (Eq 4.4), the entropy of the two-directional gradients of image (Eq 4.5), the total variation of an image (Eq 4.7) and the sum of the absolute values (Eq 4.9) will be compared under the proposed motion correction method.

The entropy of an image is defined as:

$$c_1 = -\sum_{i=1}^{N} \frac{|p_i|}{p_{\text{total}}} \ln\left(\frac{|p_i|}{p_{\text{total}}}\right), \tag{4.2}$$

where p_i is the pixel value of the image, and N is the total number of pixels of the image. p_{total} is given by:

$$p_{\text{total}} = \sqrt{\sum_{i=1}^{N} p_i^2}. \tag{4.3}$$

The entropy of the one-directional gradient of an image is defined as:

$$c_2 = H(D_y I). \tag{4.4}$$

The entropy of the two-directional gradients of an image is defined as:

$$c_3 = H(D_x I) + H(D_y I), \tag{4.5}$$

where D_x and D_y are the difference matrices in the horizontal and vertical directions, I is the input image, and $H()$ is defined as:

$$H(p) = -v^T \ln v, v = \sqrt{\frac{p \odot p^*}{p^H p}}, \tag{4.6}$$

where $\odot$ is the point-wise product of two vectors, p is the pixel vector of the image I, $*$ represents the complex conjugate, and H represents complex conjugate transpose.

The total variation of an image is defined as:

$$c_4 = S(D_x I) + S(D_y I), \tag{4.7}$$

where $S()$ is defined as:

$$S(p) = \sum_{i=1}^{N} |p_i|, \tag{4.8}$$

where p_i is the pixel value of the image.

The sum of the absolute values of an image is defined as:

$$c_5 = \sum_{i=1}^{N} |p_i|. \tag{4.9}$$

4.4 Proposed method

In order to decrease computational complexity and avoid being trapped in local minima, the proposed method involves two steps: piecewise linear initial approximation and joint refinement of a global model to perform global estimation.

piecewise linear initial approximation

K-space is divided into several segments based on acquisition order. Linear (uniform speed) motion (two translations and one rotation) is assumed in each segment to get initial motion parameters, which are the slopes (the speed) of the linear motions. In order to obtain the slopes of these linear motions, searching is done within possible slopes to optimize the criterion. A linear motion approximation is reasonable, since the acquisition time in each segment is relatively short. Subject motion velocity is expected to be in a small range within a small time frame, which makes the search space small and improves search efficiency. The process is shown in Figure 4.3. Due to the three parameters of the motion model, the search space consists of three levels of loops. In order to further improve search efficiency, golden-section search is introduced to reduce search times, which will be discussed in the later section.

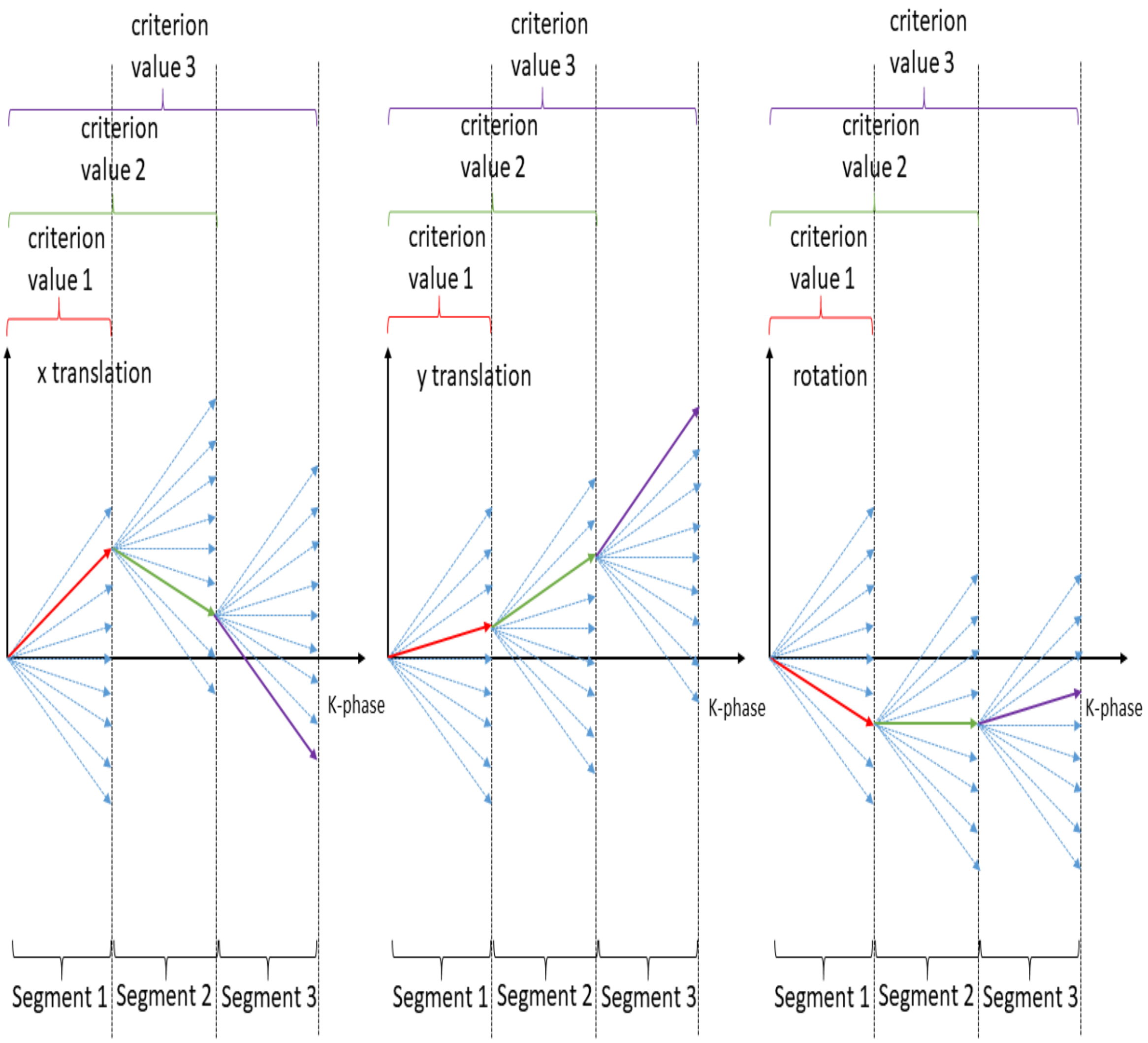

Figure 4.3: The process of piecewise linear initial approximation. There are three motion curves with the x axis representing k_{phase} lines and the y axis representing pixels for x, y translations and rotation degree for rotation. The whole k-space is divided into three segments with a certain number of k_{phase} lines in each segment. In Segment 1, the linear estimations of the three motions are chosen from 729 ($9 \times 9 \times 9$, in each motion curve, 9 slopes (blue dashed line) are given) different motion combinations, which can minimize the criterion of the image formed by Segment 1, marked as red lines. In Segment 2, the linear estimations of the three motions are chosen from 729 different motion combinations all starting from the linear estimation of Segment 1, which can minimize the criterion of the image formed by Segment 1 and Segment 2, marked as green lines. The process is repeated for Segment 3.

joint refinement of global model

To approximate exact motion, joint refinement of global refinement is implemented on the piecewise linear initial approximation. Several equally spaced control points are chosen on the piecewise linear initial approximation. Based on the assumption that subject motion is smooth, a piecewise cubic Hermite interpolating polynomial using MATLAB function `pchip` is fitted from the control points to obtain smooth motion curves. To further refine motion curves, the MATLAB function `fminsearch` is used to globally optimize the criterion by refining the cubic Hermite interpolation curves iteratively. In each iteration, one more control point is added from the previous refined motion curve to provide more degrees of freedom for the motion curve until the desired model precision is accomplished. In each iteration, three motion curves (two translational curves and one rotation curve) are considered as a system to optimize the criterion. The Figure 4.4 shows the above process.

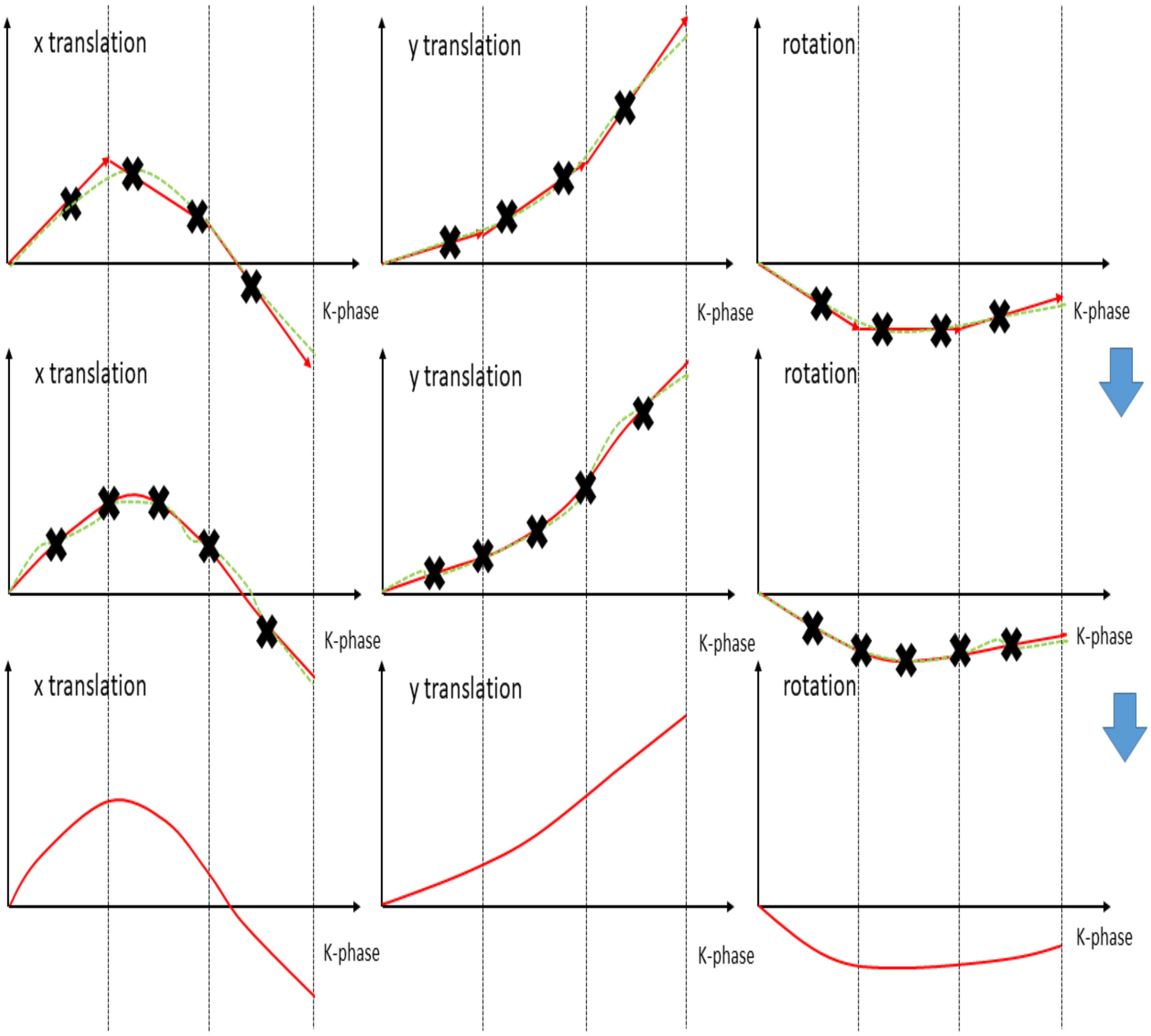

Figure 4.4: The process of joint refinement of global model. In the first row, four equally spaced control points (black cross) are chosen on the piecewise linear approximation (red linear lines) for each motion parameter, and the globally criterion optimization is accomplished by refining three piecewise cubic Hermite interpolating polynomials (three green dashed curves) fitted from the four control points. One more control point is added from the previous refined motion curves (red curves in the second row) to get a refined curves (green dashed curves in the second row). The process is repeated until the desired model precision is accomplished (three red curves in the third row).

To handle the nonuniform sampling in k-space after correction of large angle rotations (Figure 2.8), image rotation correction is performed in the spatial domain. After the image formed by one k-space segment is corrected in the spatial domain, the image is transformed back to the frequency domain, and then the same segment is acquired by resampling the frequency domain. The whole process is shown in Figure 4.5.

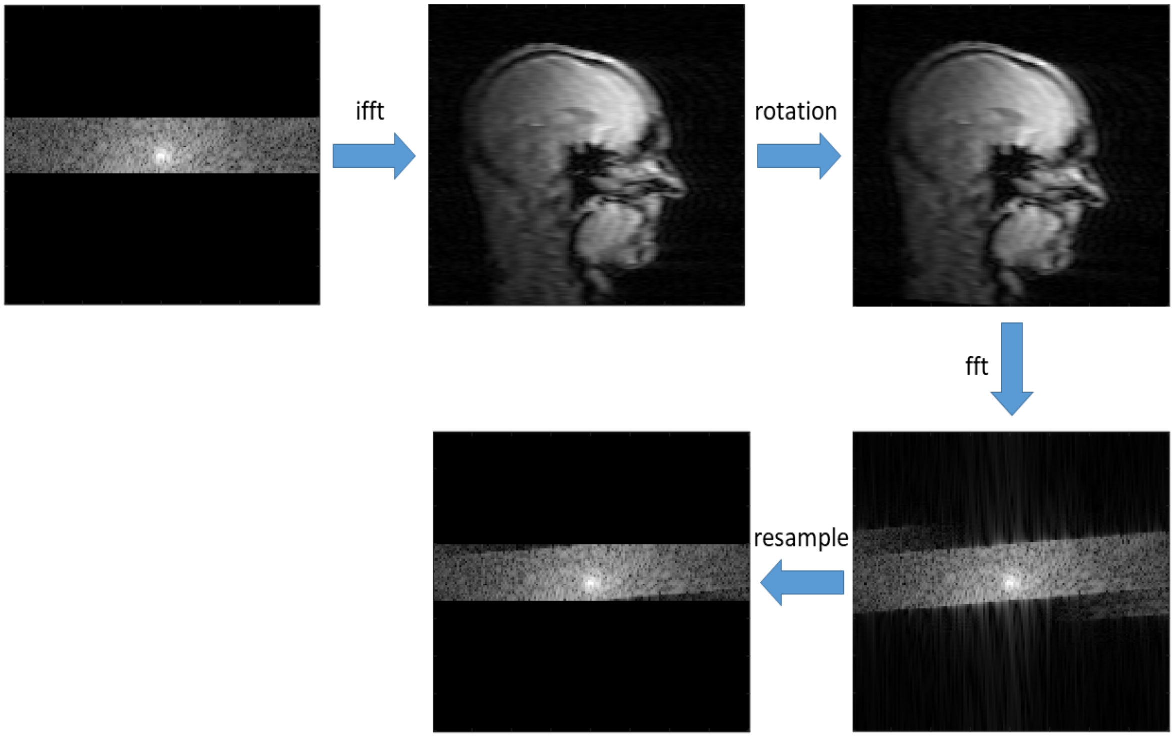

Figure 4.5: The process of rotation correction. The frequency domain images are logarithmically scaled.

4.5 Golden-section search

To make rotation search more efficient, golden-section search is implemented. Here the golden-section search method is discussed in detail first.

Golden-section search is used to find the extremum of a strictly unimodal function by reducing the value range successively [101]. The function values at three points are always maintained, and their distances form a golden ratio. This algorithm, which was first introduced by Kiefer [52], can narrow the range where an extremum exists efficiently. The function values at three points are compared to further narrow the search range.

Figure 4.6 illustrates one step of a golden-section algorithm to find a minimum. f_1, f_2 and f_3 are known values, and f_2 is smaller than f_1 and f_3. The minimum exists in $[x_1, x_3]$.

x_4 is used to further narrow the search range. If f_{4a} is the function value of x_4, the minimum exists in $[x_1, x_4]$, and x_1, x_2 and x_4 are new triplet points needed to be maintained. If f_{4b} is the function value of x_4, the minimum exists in the $[x_2, x_3]$, and x_2, x_4 and x_3 are new triplet points need to be maintained. Search range is narrowed at each step.

The selection of the position of x_4 is important. The new search range is either $[x_1, x_4]$ or $[x_2, x_3]$. In order to reduce iterative times, the length of $[x_1, x_4]$ and the length of $[x_2, x_3]$ should be the same: $b = a + c$. So $x_4 = x_1 + (x_3 - x_2)$. Since x_2 should have the same proportion of space as the new triples points x_1, x_2, x_4 and x_2, x_4, x_3, two equations are derived below:

If x_1, x_2, x_4 are the new triplet points:

$$\frac{c}{a} = \frac{a}{b}. \tag{4.10}$$

If x_2, x_4, x_3 are the new triplet points:

$$\frac{c}{b-c} = \frac{a}{b}. \tag{4.11}$$

From Eq 4.10 and Eq 4.11, we can show that b/a is equal to the golden ratio.

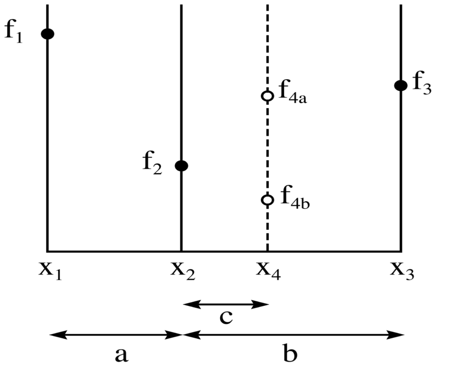

Figure 4.6: One step of golden-section search to find the minimum. (Figure 4.6 is from [101].)

We cannot prove that the criterion values in the rotation search range satisfy a strictly unimodal function condition, but all numerical simulations show they can be treated as a strictly unimodal function.

Golden-section search is used to reduce rotation search times in the step of piecewise linear initial approximation. For each trial of translations, the rotation is chosen by golden-section search to minimize a criterion.

4.6 Map data structure

To eliminate repeated computation, two map data structures are used to improve efficiency. A map is a data structure which is used for fast lookup or data searching. A map uses key-value pairs to store and quickly search data. Every key is unique and maps to a value. In our method, one map is used to store the rotated k-space data with rotation angle as the key, since the image rotation is time consuming and many repeated calculations are potentially needed. The key-value pairs of the map are illustrated in Figure 4.7. The other map is used to keep the criterion for previously evaluated correction parameters in the golden-section search of rotation. Golden-section search decreases rotation search times, and the map data structure saves the calculated results for further use. The processing time is cut in half by using golden-section rotation search and the map data structure.

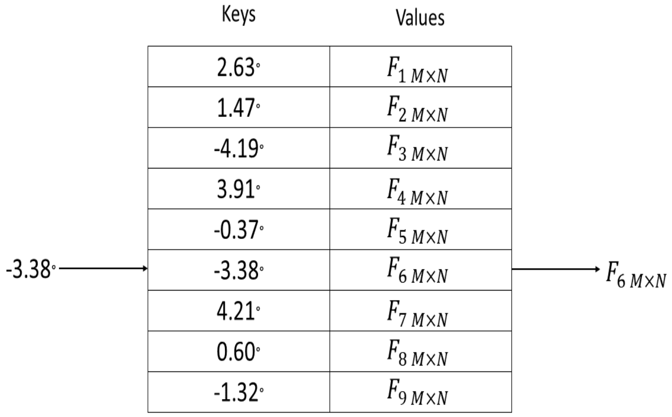

Keys	Values
2.63°	$F_{1\,M\times N}$
1.47°	$F_{2\,M\times N}$
-4.19°	$F_{3\,M\times N}$
3.91°	$F_{4\,M\times N}$
-0.37°	$F_{5\,M\times N}$
-3.38°	$F_{6\,M\times N}$
4.21°	$F_{7\,M\times N}$
0.60°	$F_{8\,M\times N}$
-1.32°	$F_{9\,M\times N}$

Figure 4.7: The map is used to store the rotated k-space data with rotation angle as the key. When the rotation angle $-3.38°$ is searched, the corresponding rotated k-space matrix $F_{6M\times N}$ is returned.

4.7 Interpolation methods

Two interpolation methods—rotation interpolation and translation interpolation—are used in the proposed method. In order to preserve the image quality of rotated images, zeropadding in the frequency domain to interpolate the image is used before image rotation, which is shown in Figure 4.8. This strategy effectively reduces the decay of high frequencies of rotated images arising from nonideal interpolation. But interpolation in the bigger image increases calculation time greatly. A trade-off is made between image quality and processing time. Figure 4.9 shows the error of the image with zeropadding rotation interpolation is much smaller than the image with no zeropadding rotation interpolation. In order to obtain subpixel translation accuracy, translation interpolation is achieved in the frequency domain, according to the properties of the Fourier transform:

$$\begin{cases} f(x,y) \Leftrightarrow F(u,v), \\ f(x-a,y-b) \Leftrightarrow e^{-j2\pi(au+bv)}F(u,v). \end{cases} \tag{4.12}$$

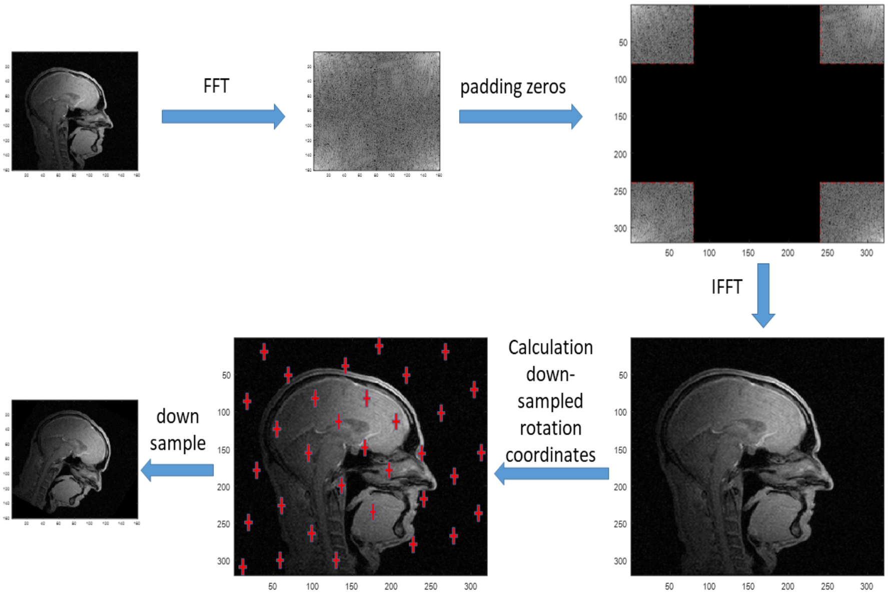

Figure 4.8: Rotation interpolation. The frequency domain images are logarithmically scaled. The length and width of the zeropadded images are twice the original image.

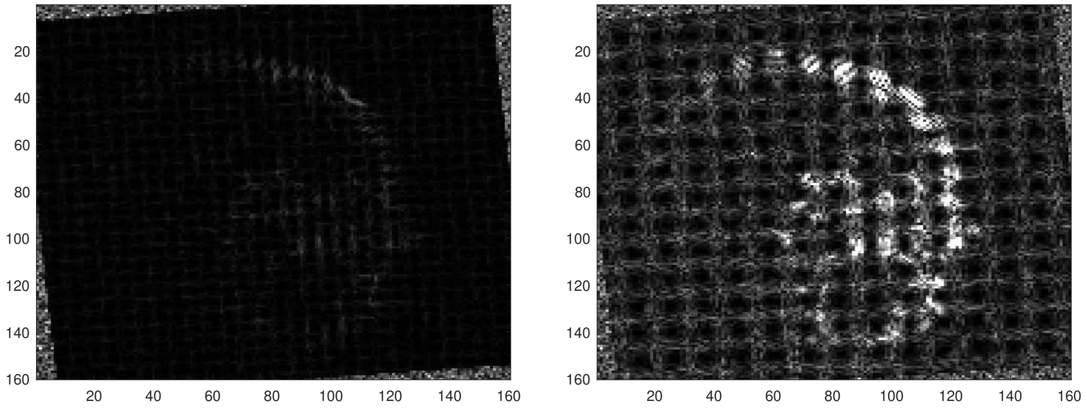

(a)

(b)

Figure 4.9: The difference images comparison. The same image is used as the reference images but different floating image. For (a), the floating image is generated by Figure 4.8. For (b), the floating image is generated by rotating the reference image directly. In order to acquire the same orientation with the reference image, both floating images rotate an angle clockwise and then rotate the same angle counterclockwise. (In order to rotate clockwise and counterclockwise, for (a), the padding zero image is used to rotate and then downsampled.) Both difference images are shown at the same scaling. The dominant error occurs around the edge in (a), while the image content error is the main error in (b) with a bigger margin.

4.8 Simulations

In order to validate the proposed method and compare the five criteria discussed above using the proposed method, simulations were conducted in this section. Three kinds of motion—piecewise linear, parabolic, and sinusoidal—were implemented to simulate two-translational and rotational motion in the 2D plane on a reference image. In order to better model real motion, the parameters of motion were chosen randomly within certain ranges. Fig 4.10 shows one example of each of the three motions.

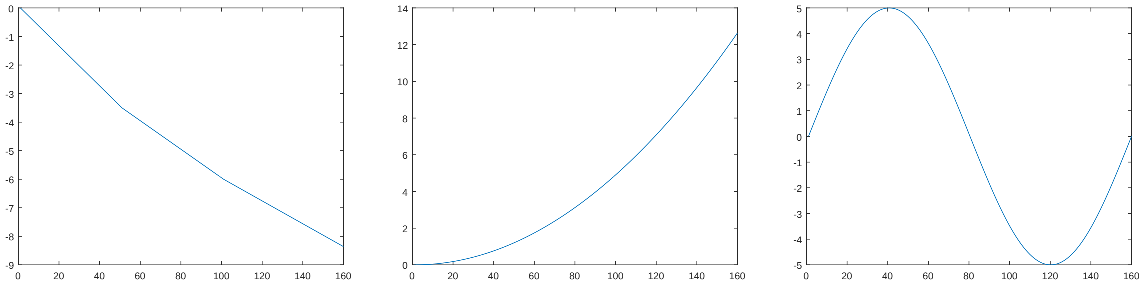

(a) (b) (c)

Figure 4.10: Three different motions. The number of function values (160) corresponds to the number of k_{phase} lines. Horizontal axis coordinates from 1 to 160 correspond to centric-out phase-encode lines acquisition order from the central (low frequency $k_{\text{phase}} = 0$) to the peripheral region of k-space (high frequency); vertical axis coordinates correspond to the motions of each k_{phase} line in one of the three motion directions (two translations with unit pixel and rotation with unit degree). (a) piecewise linear. (b) parabolic. (c) sinusoidal.

The reference image was chosen to be a motion-free complex real-experimental head MR image in the sagittal plane formed by raw k-space data in one coil. The reference image was acquired on a Siemens Verio 3T Scanner by a single-slice 2D GRE sequence with centric-out phase-encode line order at Auburn University MRI Research Center. Since this acquisition order of k_{phase} lines was used for real data in the proposed method, the same acquisition order with the reference sequence was used to simulate motion in this section. This made the simulations closer to the real experiments. In each simulation, the input was a motion-corrupted image generated by modeling motion using one of the above motion trajectories; the output was five motion-corrected images with five motion estimation plots using the five criteria. In most cases, the proposed method can effectively reduce motion artifacts no matter which criterion was used. In some cases, the difference between the motion-corrected images and the reference image by visual inspection is minimal. Fig 4.11 shows one example of comparison between the reference image, motion-corrupted image, and five motion-corrected images.

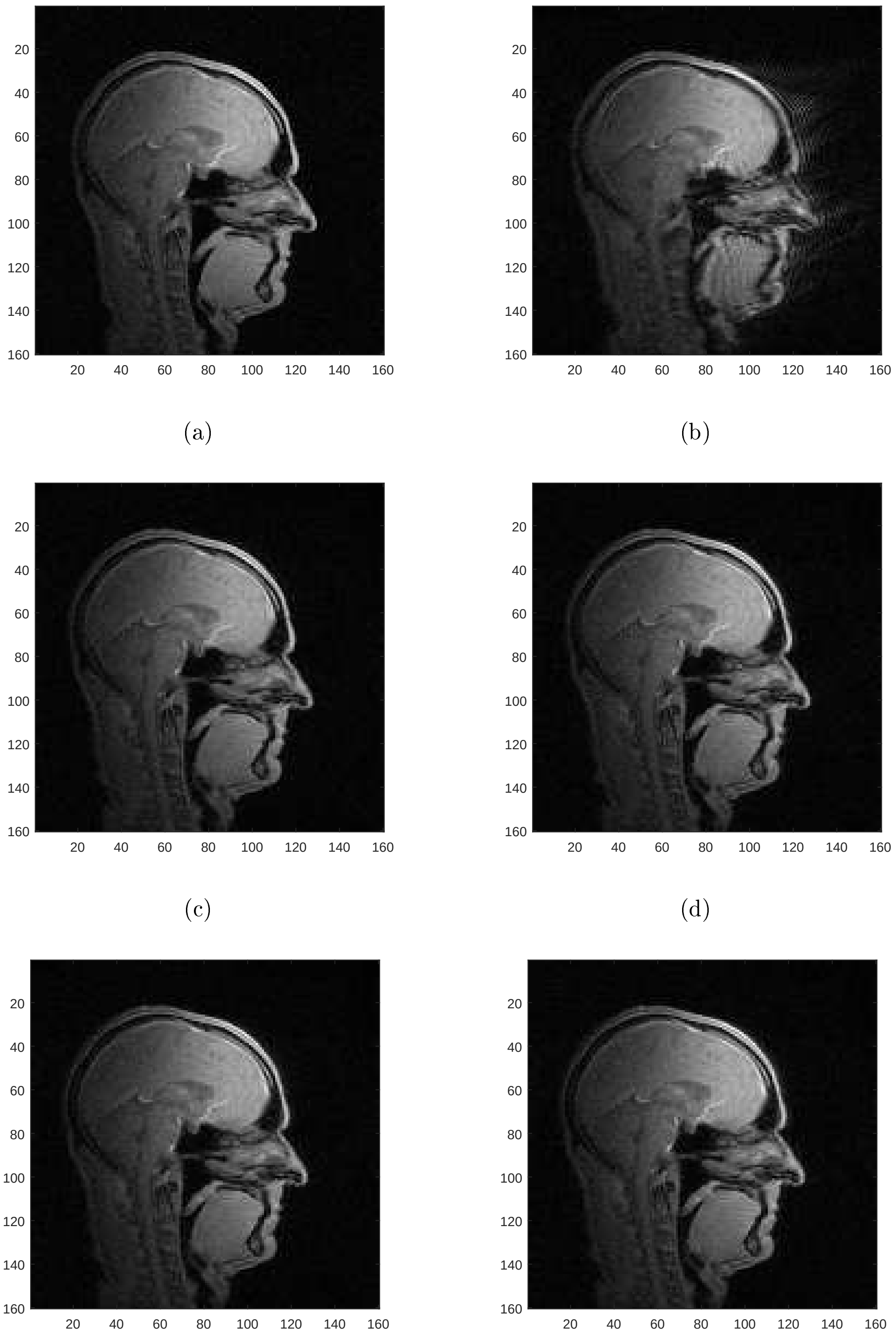

(a)

(b)

(c)

(d)

(e)

(f)

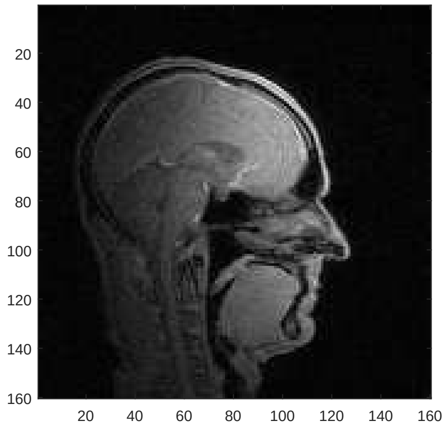

(g)

Figure 4.11: Comparison of the reference image, motion-corrupted image, and five corrected images. (a)The reference image. (b)The motion-corrupted image. (c)The motion-corrected image based on image entropy. (d)The motion-corrected image based on the entropy of one-directional gradient of image along the phase-encoding direction. (e)The motion-corrected image based on entropy of two directional gradients of image. (f)The motion-corrected image based on total variation. (g)The motion-corrected image based on the sum of absolute value.

In some cases, some criteria performed worse than other criteria. In Fig 4.12, the motion-corrected image based on the sum of absolute value looks worse than other corrected images, and some artifacts cannot be properly erased in that image.

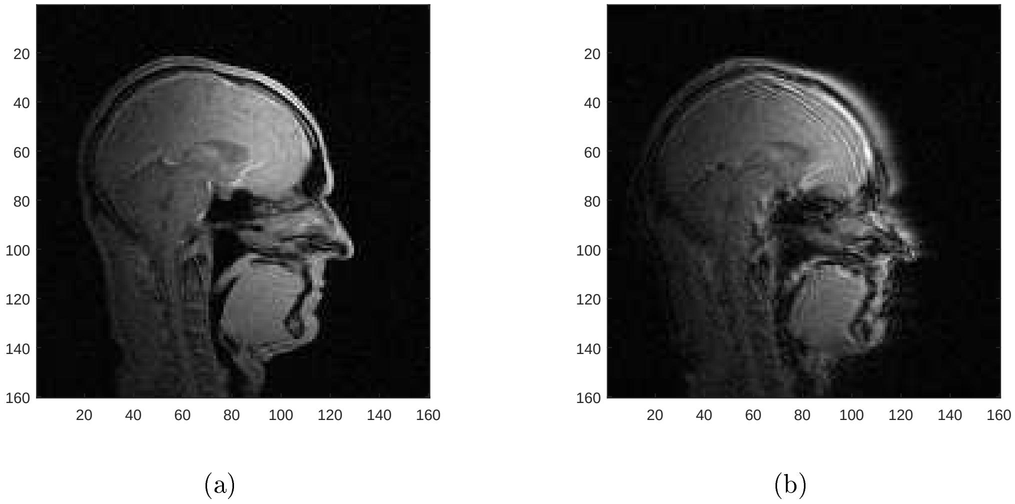

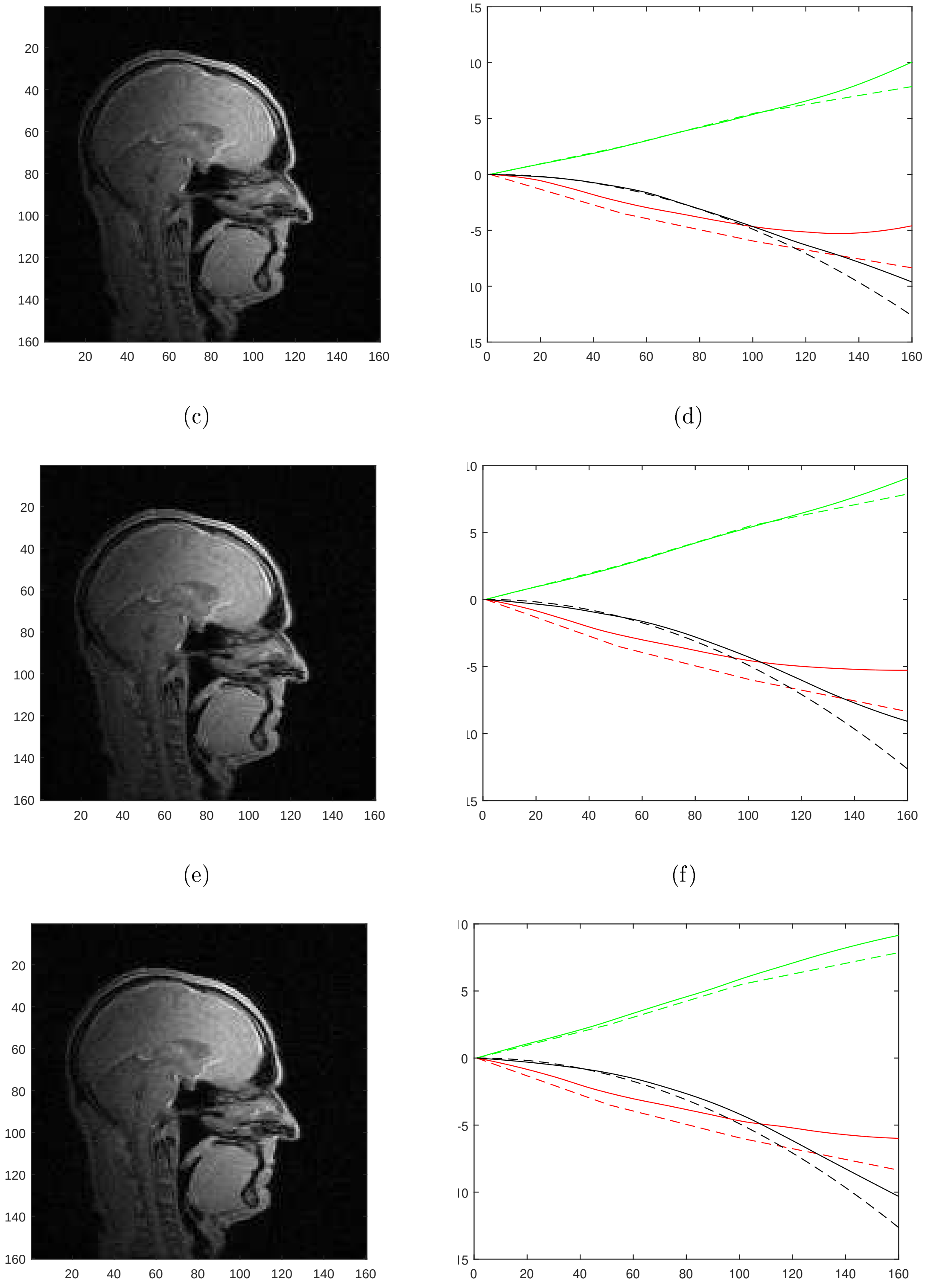

(c)

(d)

(e)

(f)

(g)

(h)

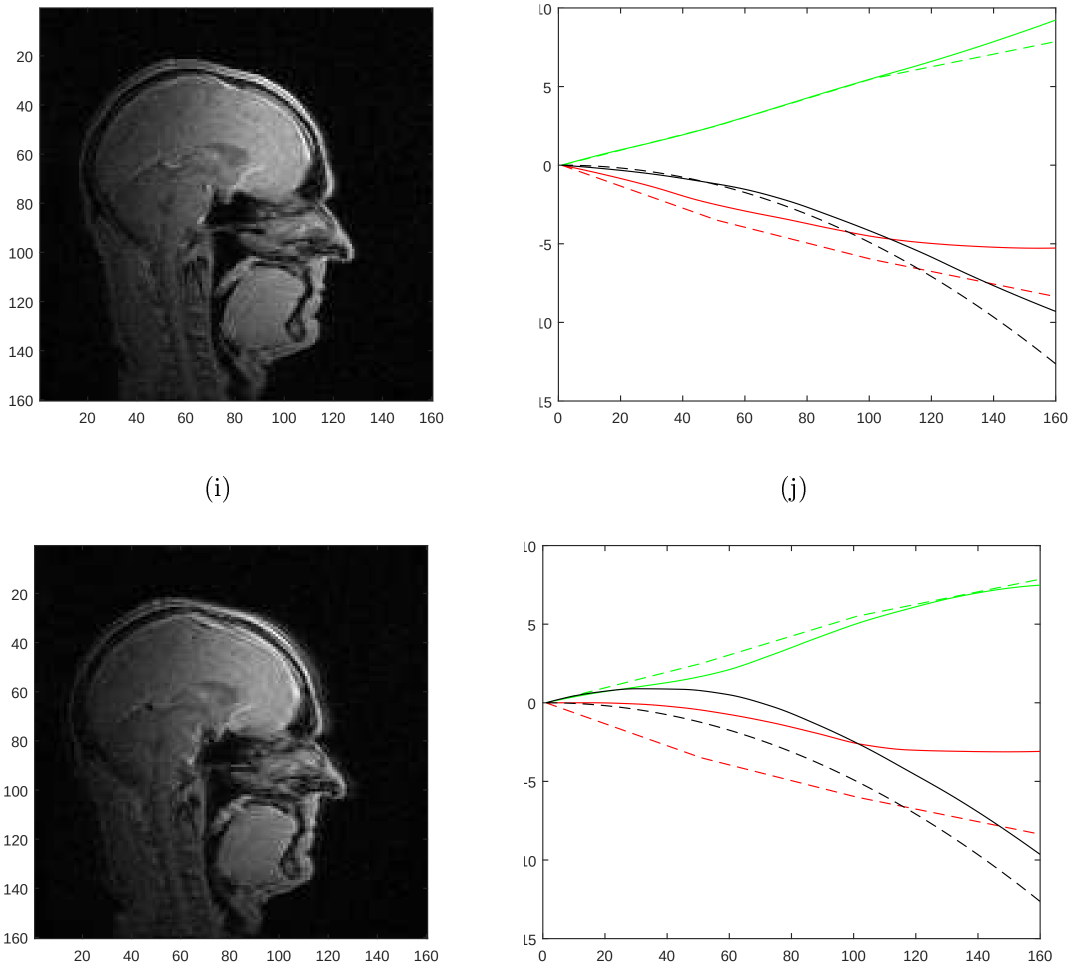

(k)

(l)

Figure 4.12: Comparison of the reference image, motion-corrupted image, and five motion-corrected images and corresponding motion estimation plots. (a)The reference image. (b)The simulated motion-corrupted image. (c)The motion-corrected image based on the image entropy. (e)The motion-corrected image based on the entropy of the one-directional gradient of image along the phase-encoding direction. (g)The motion-corrected image based on the entropy of the two directional gradients of image. (i)The motion-corrected image based on the total variation. (k)The motion-corrected image based on the sum of the absolute values. (d)(f)(h)(j)(l) are the comparisons of the estimated motion trajectories and real motion trajectories based on the five criteria. The solid curves represent real motion trajectories (green for horizontal motion, red for vertical motion and black for rotation), and the dashed curves represent estimated motion trajectories (green for horizontal translation and red for vertical translation with unit pixel of the y axis; black for rotation with unit degree of the y axis).

Comparing Fig 4.12 (d)(f)(h)(j)(l), Fig 4.12 (l) had the biggest error between real and estimated motion trajectories. That's the reason why Fig 4.12 (k) still had artifacts.

When the simulated displacement is large, such as a sinusoidal motion trajectory, the motion-corrected images based on the image entropy and the sum of the absolute values were worse than the motion-corrected images based on the entropy of the one-directional gradient of image along the phase-encoding direction, the entropy of the two directional gradients of image and the total variation. Fig 4.13 shows the results.

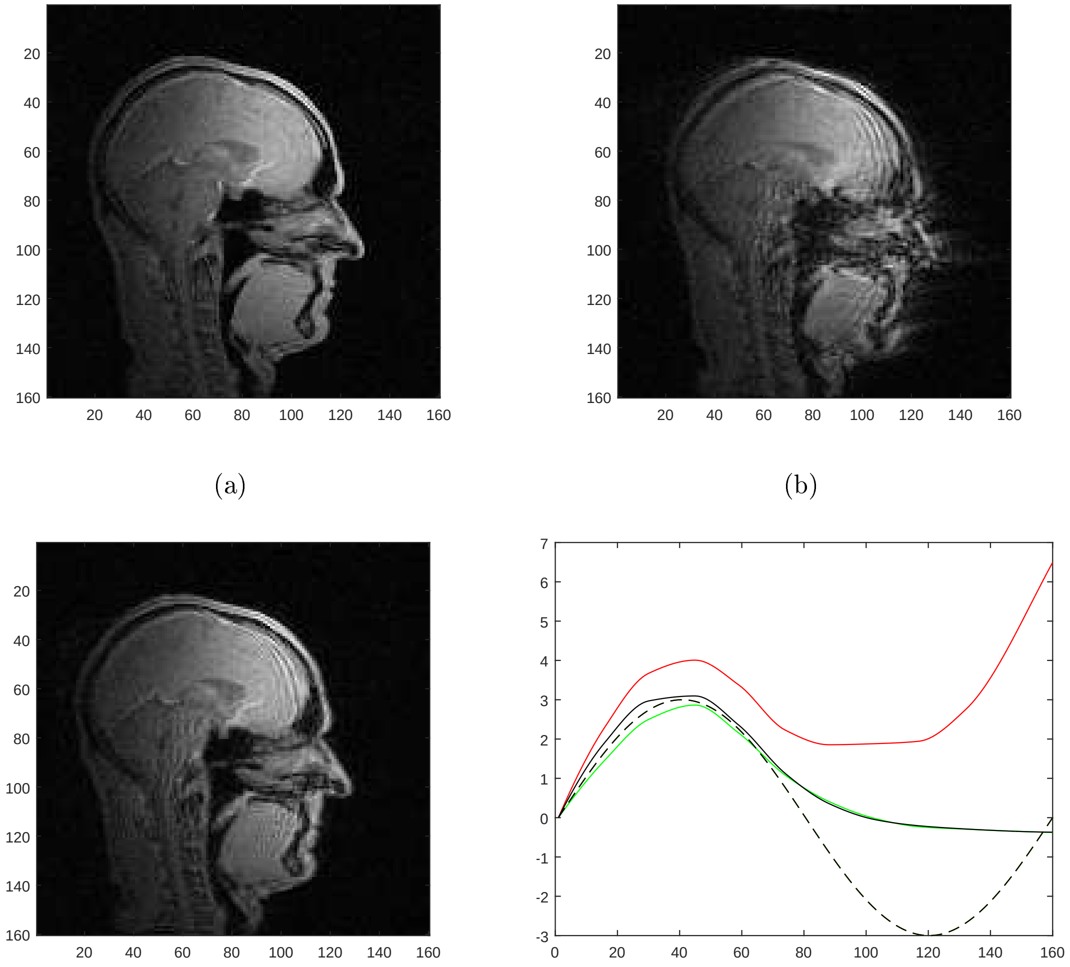

(a)

(b)

(c)

(d)

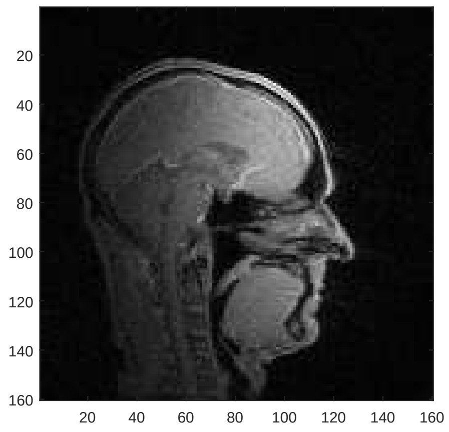
20
40
60
80
100
120
140
160
20
40
60
80
100
120
140
160

(e)

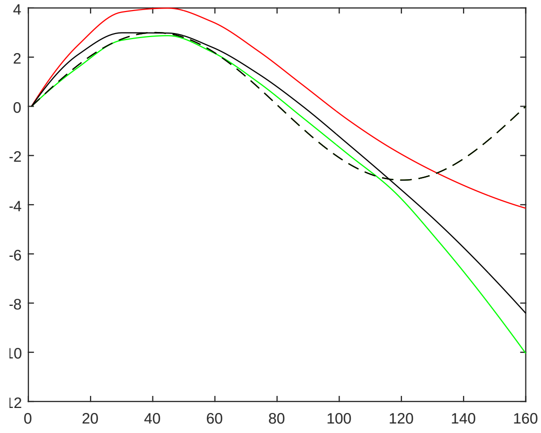
4
2
0
-2
-4
-6
-8
10
12
0
20
40
60
80
100
120
140
160

(f)

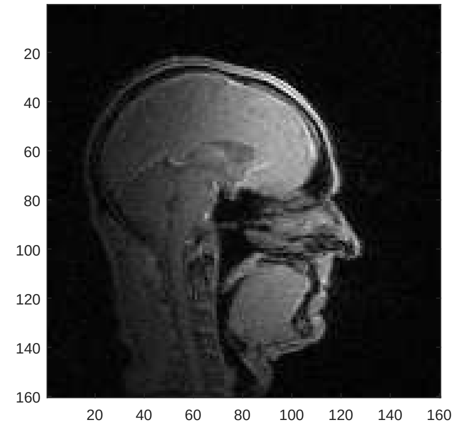
20
40
60
80
100
120
140
160
20
40
60
80
100
120
140
160

(g)

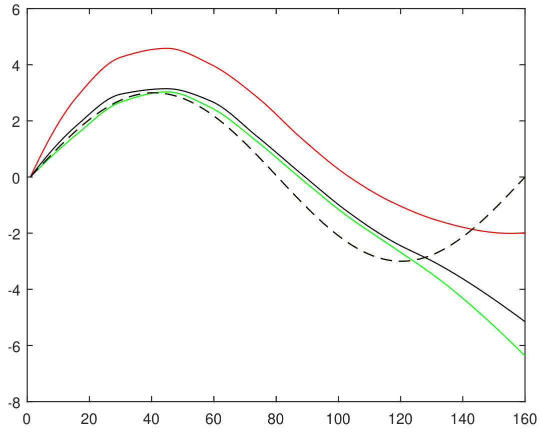
6
4
2
0
-2
-4
-6
-8
0
20
40
60
80
100
120
140
160

(h)

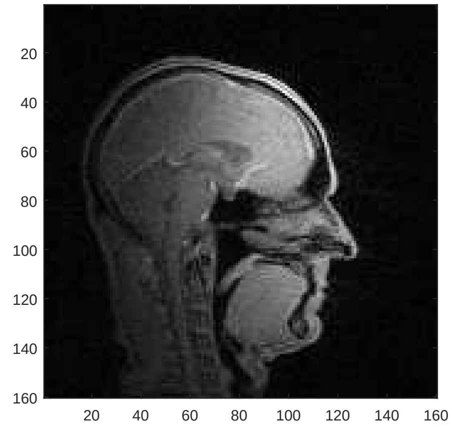
20
40
60
80
100
120
140
160
20
40
60
80
100
120
140
160

(i)

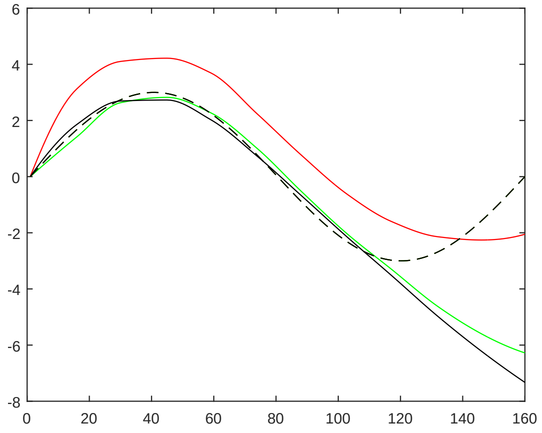
6
4
2
0
-2
-4
-6
-8
0
20
40
60
80
100
120
140
160

(j)

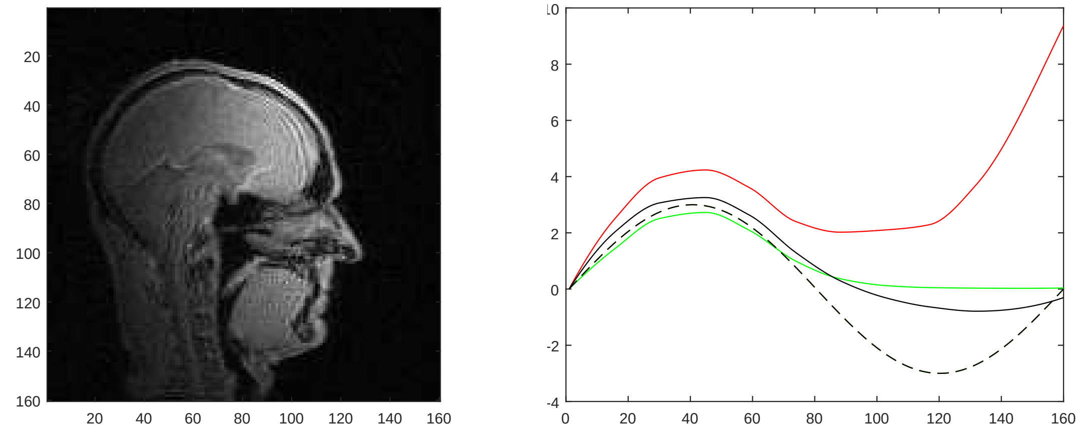

(k)

(l)

Figure 4.13: Comparison of the reference image, motion-corrupted image, and five motion-corrected images and corresponding motion estimation plots. (a)The reference image. (b)The simulated motion-corrupted image. (c)The motion-corrected image based on the image entropy. (e)The motion-corrected image based on the entropy of the one-directional gradient of image along the phase-encoding direction. (g)The motion-corrected image based on the entropy of the two directional gradients of image. (i)The motion-corrected image based on the total variation. (k)The motion-corrected image based on the sum of the absolute values. (d)(f)(h)(j)(l) are the comparisons of the estimated motion trajectories and real motion trajectories based on the five criteria. The solid curves represent real motion trajectories (green for horizontal motion, red for vertical motion and black for rotation), and the dashed curves represent estimated motion trajectories (green for horizontal translation and red for vertical translation with unit pixel of the y axis; black for rotation with unit degree of the y axis).

In Fig 4.13 (f)(h)(j), although the estimated motion cannot totally correct the real motion at the high frequency part (the last one quarter of the sinusoidal curves), there is not too much impact on the motion-corrected images. Although the motion-corrected images based on the image entropy and the sum of the absolute values still had some artifacts, the motion-corrected images were improved significantly compared to the simulated motion-corrupted image.

4.9 Experiments

The performance of the three criteria—the entropy of the one or two directional gradients of image and the total variation—under the proposed method were good and similar in the simulations. Therefore, we selected one of the three—the total variation—to be the focus criterion to correct real motion in the experiments. Head images in the sagittal and axial plane were acquired on a Siemens Verio 3T Scanner using the same sequence as in the Simulations section (Auburn University MRI Research Center). The acquisition order of k_{phase} lines is used to correct the motion. The subject was instructed to perform head nods to acquire motion-corrupted images in the sagittal plane and side-to-side motion to acquire motion-corrupted images in the axial plane. Two no-motion images were acquired separately by the same scan sequence as reference images for comparison. Fig 4.14 and Fig 4.15 show the results of applying the proposed motion correction method on the motion-corrupted images. The motion-corrected images indicate that our method was able to eliminate motion artifacts and preserve sharp boundaries. This method is also efficient. The whole processing time for 160×160 images is under a minute on an 8GB RAM Intel Core i7-3630QM 2.40 GHz CPU processor machines using MATLAB.

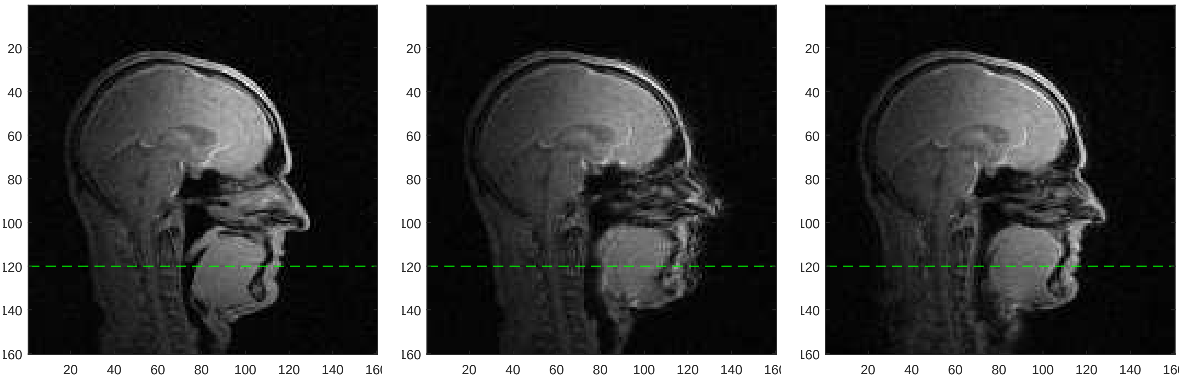

(a) (b) (c)

Figure 4.14: Comparison of the reference image, real motion-corrupted image and motion-corrected image in the sagittal plane. Due to the motion difference between the neck part and the head part, the image above the green dashed line part was used to calculate the focus criterion. (a) No-motion (reference) image. (b) Real motion-corrupted image. (c) Motion-corrected image.

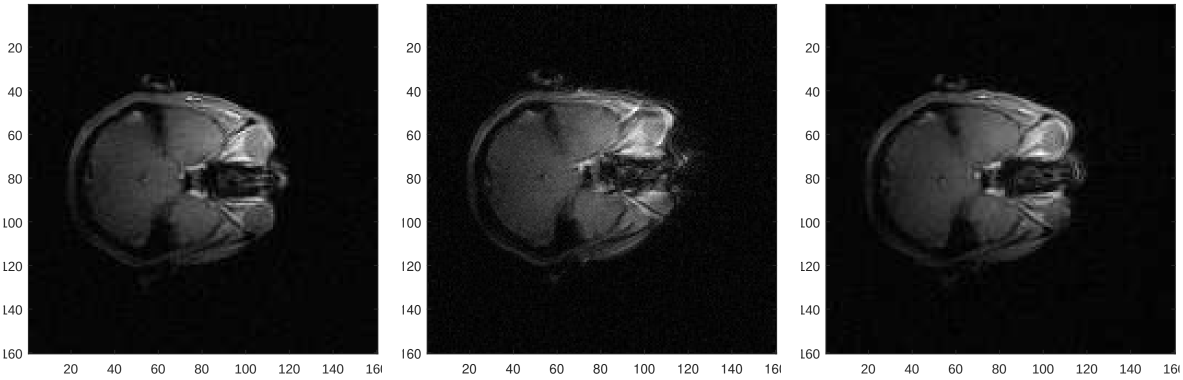

(a) (b) (c)

Figure 4.15: Comparison of the no-motion image, real motion-corrupted image and motion-corrected image in the axial plane. (a) No-motion (reference) image. (b) Real motion-corrupted image. (c) Motion-corrected image.

For the sagittal plane images, due to the different motion between neck part (below the green dashed line) and head part (above the green dashed line), a selected window (above the green dashed line) designated a FOV over which to calculate the focus criterion, which explains why the neck part of the motion-corrected image is still blurred.

4.10 Discussion

The proposed method on a windowed image may potentially correct some complicated nonrigid motions. In some cases, we can assume that the whole image can be divided into several small subimages, within which the motion can be modeled as rigid. The subimages are combined after motion of each subimage is corrected by the windowed method.

The proposed method can be extended to 3D. For 3D rigid motion, six motion trajectories need to be estimated. Due to the increased search space in 3D, the piecewise linear initial approximation needs to be more accurate and efficient.

Chapter 5

An Efficient Motion Correction Method Based on Fast Robust Correlation

Translational search can be computationally demanding. A correlation operation can be used to calculate an image match when the matching criterion is the sum of squared errors. However, this approach cannot be used for nonquadratic matching criteria. Fast robust correlation is a computationally efficient search algorithm for translational image matching in the frequency domain. This method can calculate matching surfaces from nonquadratic criteria using a series of high-speed correlations by defining a kernel with sinusoidal terms. In this chapter, an efficient motion correction method based on fast robust correlation is proposed. The proposed method corrects motion-distorted images by aligning translational motion between images formed by neighboring frequency segments. Since the squared difference kernel is invariant to motion between partial-Fourier images, we adopt the absolute value kernel, which can be easily approximated by sinusoidal terms. Total variation of the sum of partial-Fourier images is chosen as the new matching criterion. FFTs are used to calculate correlations for computational speed. Different search strategies to combine and correct motion over the whole k-space are discussed and compared. The proposed method can perform real-time processing to reduce image motion artifacts significantly in the simulations and MRI cardiac experiments.

This chapter is organized as follows: 5.1 review of fast robust correlation, 5.2 motion model and acquisition assumption, 5.3 the failure of squared kernel, 5.4 proposed match criterion, 5.5 proposed method to estimate the relative motion between the neighboring segments, 5.6 search strategy, 5.7 simulations, 5.8 experiments, and 5.9 discussion.

5.1 Fast robust correlation review

Fast robust correlation (FRC) was first proposed by Fitch et al. [30]. This method implements a series of correlations to calculate the matching surface to increase computational speed. Robust behavior is achieved by defining a new kernel, which is composed of several sinusoidal terms. FRC is used in image registration, such as template matching [51] and image fusion [106]. Based on the sinusoidal terms kernel [30, 48], some principal component analysis methods [92, 58] have been proposed.

This new motion correction method is inspired by FRC. The main idea of FRC is described first.

A matching surface is used to calculate the match quality of two images over a range of 2-D shifts. The general matching surface is expressed as:

$$S(m_x, m_y) = \sum_{x,y} h\big(f(x,y) - g(x-m_x, y-m_y)\big)\alpha_f(x,y)\alpha_g(x-m_x, y-m_y), \tag{5.1}$$

where f and g are two images, m_x and m_y are two-directional translations, (x, y) is the pixel index, $\alpha_f(x, y)$ and $\alpha_g(x, y)$ are image masks, and $h(r)$ is the difference kernel, where r is the pixel difference.

Correlation functions can be calculated efficiently with FFTs, and sinusoidal terms can be rewritten as correlations to make FFT implementation possible. A nonquadratic kernel is chosen for its sensitivity to outliers and efficiency.

$$h(r) = \sum_{p=1}^{P} b_p\big(1 - \cos(a_p \pi r)\big), \tag{5.2}$$

where the parameter sets a_p and b_p determine the curve of the kernel. The robust matching surface with this kernel becomes:

$$S(m_x, m_y) = \sum_{x,y} \alpha_f(x,y)\alpha_g(x-m_x, y-m_y) \sum_{p=1}^{P} b_p \Big[1 - \cos\Big(a_1 \pi \big(f(x,y) - g(x-m_x, y-m_y)\big)\Big)\Big]. \tag{5.3}$$

Eq (5.3) can be expressed as:

$$S(m_x, m_y) = \Re\Big\{(\alpha_f \otimes \alpha_g) \sum_{p=1}^{P} b_p - \sum_{p=1}^{P} b_p \Big[\big(\alpha_f \exp(ja_p \pi f)\big) \otimes \big(\alpha_g \exp(ja_p \pi g)\big)\Big]\Big\}, \tag{5.4}$$

where $\otimes$ represents correlation. Correlations can be efficiently calculated in the Fourier domain by FFTs.

5.2 Motion model and assumption

In this chapter, motion is assumed to be two-directional translations in a 2D plane. However, compared with the previous chapter, the basic unit for motion correction is a certain number of k_y lines, which we refer to as a segment of k-space data. The whole k-space acquisition is assumed to have occurred over time in several non-overlapping neighboring segments, and we only consider the motion between different segments. Within each segment, the object is modeled as stationary. The motion assumption is shown in Figure 5.1. This assumption may not be accurate enough in some cases, but for many problems it is a good approximation.

The motion parameters Δx and Δy are functions of k_s, which is segment s of k_y lines. Therefore, the motion correction is essential to estimate a total of N_s 2D vectors M, where N_s is the number of segments. The motion parameters are given by:

$$M(k_s) = \big(\Delta x(k_s), \Delta y(k_s)\big), \tag{5.5}$$

where Δx, Δy are two-directional translation estimations.

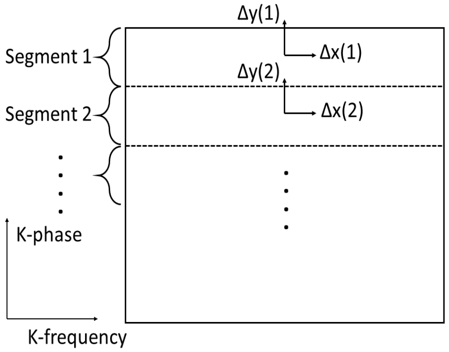

Figure 5.1: The motion assumption for the proposed motion correction method. We only consider the motion between different segments. Within each segment, the object is assumed motionless.

5.3 Squared kernel

The squared difference kernel $h(r) = r^2$, where r is the pixel difference, is not suitable for motion image reconstruction in the context of non-overlapping frequency-domain segments. To see this, consider the matching surface based on the squared difference kernel defined in [30] as follows:

$$S(m_x, m_y) = \sum_{x,y} \big(f(x,y) - g(x-m_x, y-m_y)\big)^2 \alpha_f(x,y)\alpha_g(x-m_x, y-m_y). \tag{5.6}$$

Eq (5.6) can be expressed as:

$$S = \left(f^2\alpha_f\right) \otimes \alpha_g - 2\left(f\alpha_f\right) \otimes \left(g\alpha_g\right) + \alpha_f \otimes \left(g^2\alpha_g\right), \tag{5.7}$$

where $\otimes$ represents correlation. The first term and the third term of Eq (5.7) are constant and can be neglected, and the second term can be computed in the Fourier domain:

$$f \otimes g = \text{ifft}\big(\text{fft}(f)\text{fft}^*(g)\big), \tag{5.8}$$

where * represents complex conjugate.

Since frequency segments do not overlap, this term is zero for any shifts, and the matching surface Eq (5.6) is constant.

5.4 Proposed match criterion

A new criterion is defined in the proposed method. The criterion is the total variation of the sum of images formed by the neighboring k-space segments. Signals with sharp edges have larger total variation in the presence of phase distortion, which is the kind of error that occurs when different frequency segments are acquired at different object positions.

A one-dimensional example illustrates this criterion. The translational motion in the spatial domain is equal to a linear-phase shift in the frequency domain, according to the Fourier shift property. The process of phase shift can be considered as the signal go through the unity gain nonlinear-phase filter. This nonlinear phase can introduce ringing. Figure 5.2 shows a square wave filtered by a unity gain nonlinear-phase filter. The green unfiltered signal represents an image without translational motion and the red filtered signal represents image with translational motion. The green signal has some wave-shape signal disturbance at the sharp edge after filtering. Total variation effectively measures the level of ringing, which can reflect the level of the translation motion. This example illustrates how total variation can be used to detect translation motion even when the frequency segment do not overlap.

As part of the proposed criterion, the absolute value kernel is used:

$$h(r) = |r| \tag{5.9}$$

Correlation functions can be calculated efficiently with FFTs, but correlation assumes a squared kernel.

According to the FRC method, sinusoidal terms are used to approximate the proposed kernel. These terms can then be rewritten as correlations to make FFT implementation

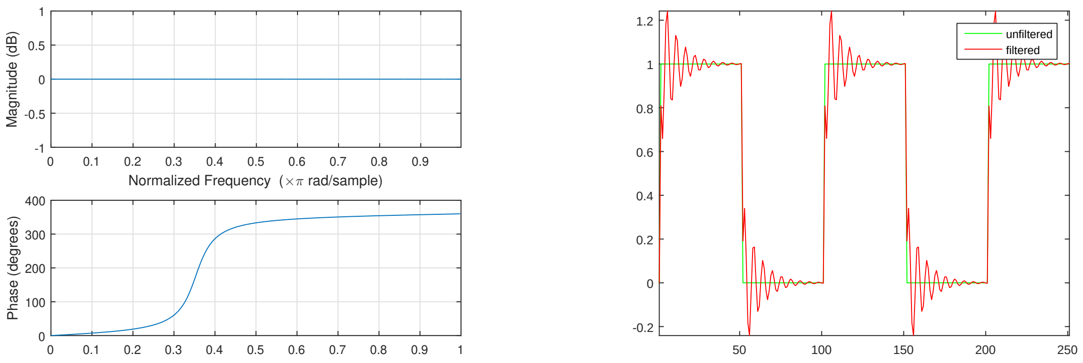

(a) (b)

Figure 5.2: The comparison between the filtered and unfiltered square wave. (a) The magnitude and phase of the filter. (b) The filtered and unfiltered square wave.

possible. A Fourier series is used as a new method to calculate the sinusoidal approximation. Since most kernels satisfy the Dirichlet conditions, the Fourier series is guaranteed to converge. For some kernels, these calculations can be relatively easy compared to [30]. Here a Fourier series is used to estimate the absolute value kernel. According to [30], pixel values should be normalized to the range of $[-1, 1]$, so we consider the Fourier series of $h(r)$ on the range of $[-1, 1]$:

$$h(r) = |r| = a_0 + \sum_{p=1}^{\infty} \big(a_p \cos(pr) + b_p \sin(pr) \big), \tag{5.10}$$

where:

$$\begin{cases} a_0 = \frac{1}{2} \int_{-1}^{1} h(r) dr, \\ a_p = \int_{-1}^{1} h(r) \cos(pr) dr, p \geqslant 1, \\ b_p = \int_{-1}^{1} h(r) \sin(pr) dr, p \geqslant 1. \end{cases} \tag{5.11}$$

Eq (5.9) is even, so $b_p = 0$. The approximation becomes:

$$h(r) \approx \frac{1}{2} - \frac{4}{\pi^2} \sum_{p=1}^{P} \frac{1}{(2p-1)^2} \cos\big((2p-1)\pi r\big) = \frac{1}{2} - \sum_{p=1}^{P} B_p \cos(A_p \pi r). \tag{5.12}$$

This result is similar to [27]. Figure 5.3 compares finite sum approximation with the absolute value kernel. The sinusoidal kernels approach the absolute value kernel as P increases. Based on the empirical performance, we choose $P = 3$ to approximate the absolute value kernel, which is enough to perform well in most cases.

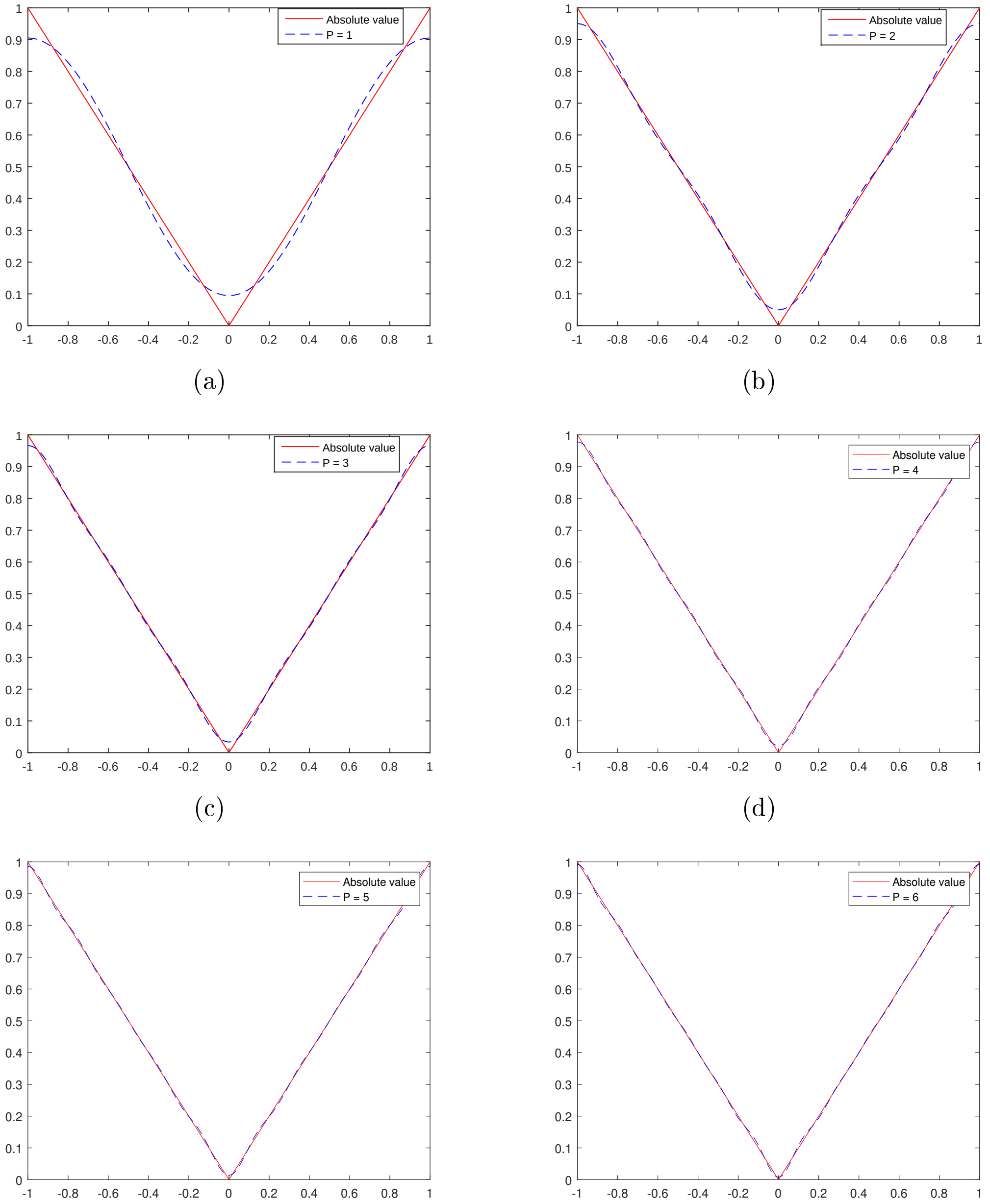

(a)

(b)

(c)

(d)

(e)

(f)

Figure 5.3: Comparison of different values of P and the absolute value kernel. (a) $P = 1$. (b) $P = 2$. (c) $P = 3$. (d) $P = 4$. (e) $P = 5$. (d) $P = 6$.

5.5 Proposed method

f and g represent two images formed by two neighboring k-space segments. f_1 and f_2 are the first difference of f in the horizontal and vertical directions. The same definition is used for g_1 and g_2. Since f_1, f_2, g_1, g_2 are all complex images, the real and imaginary parts of all these images can be represented as f_{1r}, f_{1i}, f_{2r}, f_{2i}, g_{1r}, g_{1i}, g_{2r}, g_{2i}. The matching surface is the sum of four matching surfaces, which are formed by f_{1r} and g_{1r}, f_{1i} and g_{1i}, f_{2r} and g_{2r}, and f_{2i} and g_{2i}. Consider f_{1r} and g_{1r} as an example to show the whole calculation process. Using Eq (5.12) to get the matching surface:

$$S_{1r}(m_x, m_y) = \sum_{x,y} \alpha_{f_{1r}}(x,y)\alpha_{g_{1r}}(x-m_x, y-m_y) \times \left[\frac{1}{2} - \sum_{p=1}^{P} B_p \cos\Big(A_p \pi \big(f_{1r}(x,y) + g_{1r}(x-m_x, y-m_y)\big)\Big)\right]. \tag{5.13}$$

Eq (5.13) is equal to:

$$S_{1r}(m_x, m_y) = \Re\Big\{\frac{1}{2}(\alpha_{f_{1r}} \otimes \alpha_{g_{1r}}) - \sum_{p=1}^{P} B_p \big(\alpha_{f_{1r}} e^{jA_p\pi f_{1r}} \otimes \alpha_{g_{1r}} e^{-jA_p\pi g_{1r}}\big)\Big\}. \tag{5.14}$$

Using FFTs to Eq (5.14):

$$S_{1r}(m_x, m_y) = \Re\Big\{\text{ifft}\Big(\frac{1}{2}\text{fft}(\alpha_{f_{1r}})\text{fft}^*(\alpha_{g_{1r}}) - \sum_{p=1}^{P} B_p \big(\text{fft}(\alpha_{f_{1r}} e^{jA_p\pi f_{1r}})\text{fft}^*(\alpha_{g_{1r}} e^{-jA_p\pi g_{1r}})\big)\Big)\Big\}. \tag{5.15}$$

After the four matching surfaces are computed, the translations can be calculated as follows:

$$(\hat{m}_x, \hat{m}_y) = \arg\min_{(m_x,m_y)} \big(S_{1r}(m_x, m_y) + S_{1i}(m_x, m_y) + S_{2r}(m_x, m_y) + S_{2i}(m_x, m_y)\big). \tag{5.16}$$

To obtain subpixel accuracy, interpolation is implemented by padding zeros in the frequency domain of the partial matching surface.

5.6 Search strategy

The sections above illustrated how to calculate the relative motion between two neighboring non-overlapping segments, but we still need search strategies to combine and correct motion over the whole k-space. For each search strategy, there are two kinds of segments — the reference segment and the floating segment. The relative motion between the reference and the floating segment is detected and corrected for each floating segment using the above method until all the segments are corrected for the whole k-space. Based on the empirical performance, we have concluded that no gap in k-space should be allowed between the reference and floating segments to obtain reliable motion estimates. Some search strategies are proposed in this section and the results are compared in the Simulations section. It is assumed that k-space consists of n segments.

Strategy 1

From the top to the bottom of k-space, each segment is chosen to be the reference segment, and the neighboring segment below it is the floating segment. After calculation of the relative motion of $n-1$ pairs of reference and floating segments, the motion relative to a certain segment of all the other segments is now known and is then corrected. The whole process is shown in Figure 5.4.

Strategy 2

To take advantage of the previous calculated motion information, the reference segment is enlarged after combining the previous corrected floating segments. The whole process is shown in Figure 5.5.

Strategy 3

The segment with zero frequency is chosen as reference, which is enlarged after combining the previous corrected floating segments similar to Strategy 2. Considering the impact of the symmetric segments in k-space, the neighboring symmetric segments are in turn chosen as the floating segments. The whole process is shown in Figure 5.6.

Strategy 4

Compared with the Strategy 3, the odd segment is corrected twice. When the odd segment is corrected the first time, the symmetric segments are not included in the reference segment. This omission may result in error. So in Strategy 4, when the odd segments are corrected the second time, the corrected symmetric segments are combined into the reference segment. The whole process is shown in Figure 5.7.

Strategy 5

Compared with Strategy 4, the odd and even segments both are corrected twice, which is shown in Figure 5.8 in detail.

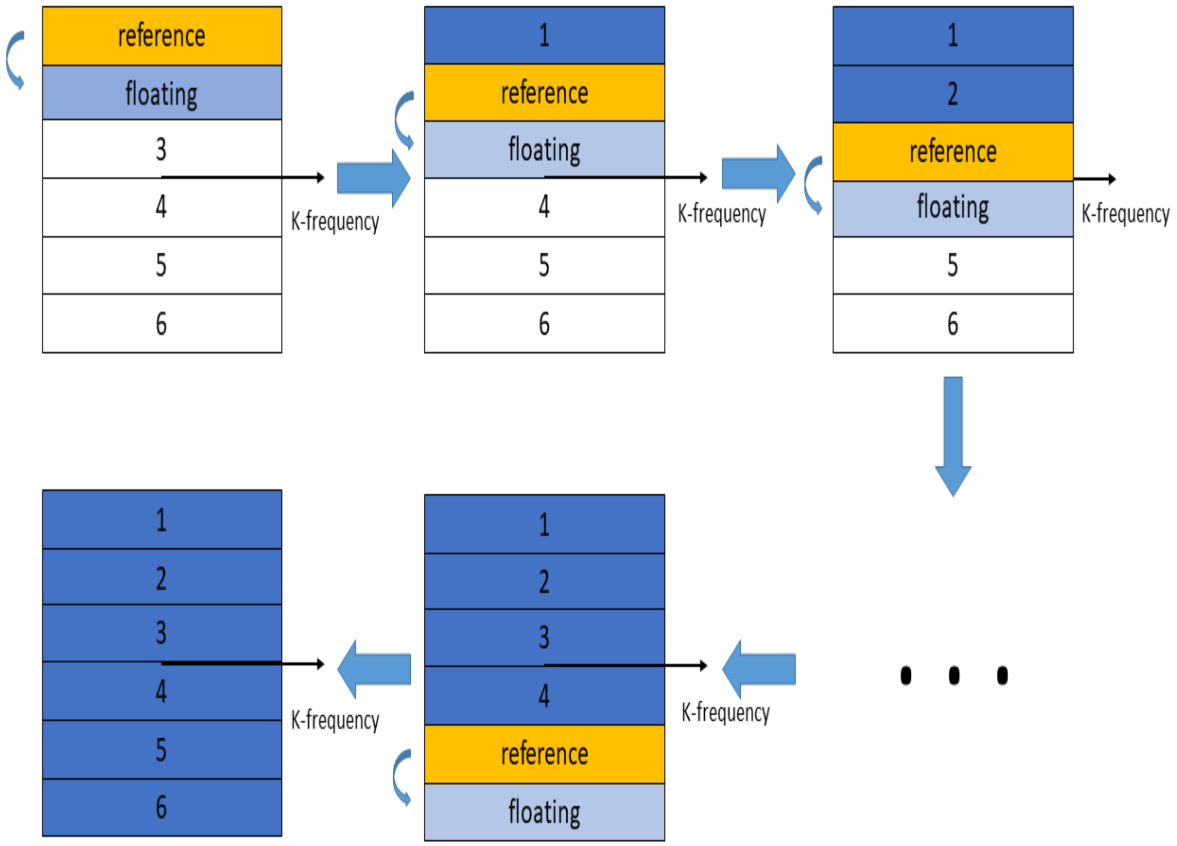

Figure 5.4: Search Strategy 1 of the proposed method. Different numbers represent different segments. The yellow segment is the reference segment, the light blue one is the corresponding floating segment, and the blue one is the motion-corrected segment. From top to bottom, the relative motion between the reference and floating segments is determined.

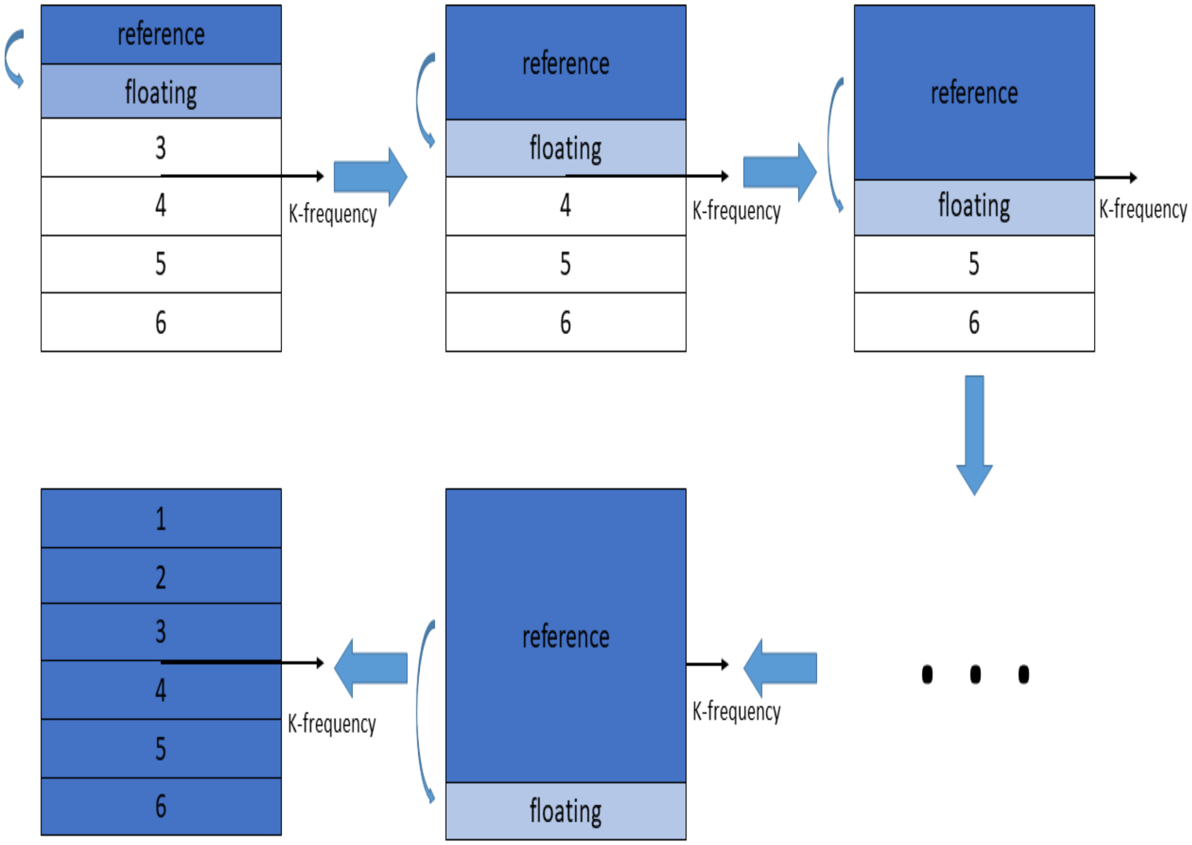

Figure 5.5: Search Strategy 2 of the proposed method. Different numbers represent different segments. The blue segment is the reference segment, and the light blue one is the corresponding floating segment. The reference segment is enlarged after combining the previous corrected floating segment until all the segments are corrected.

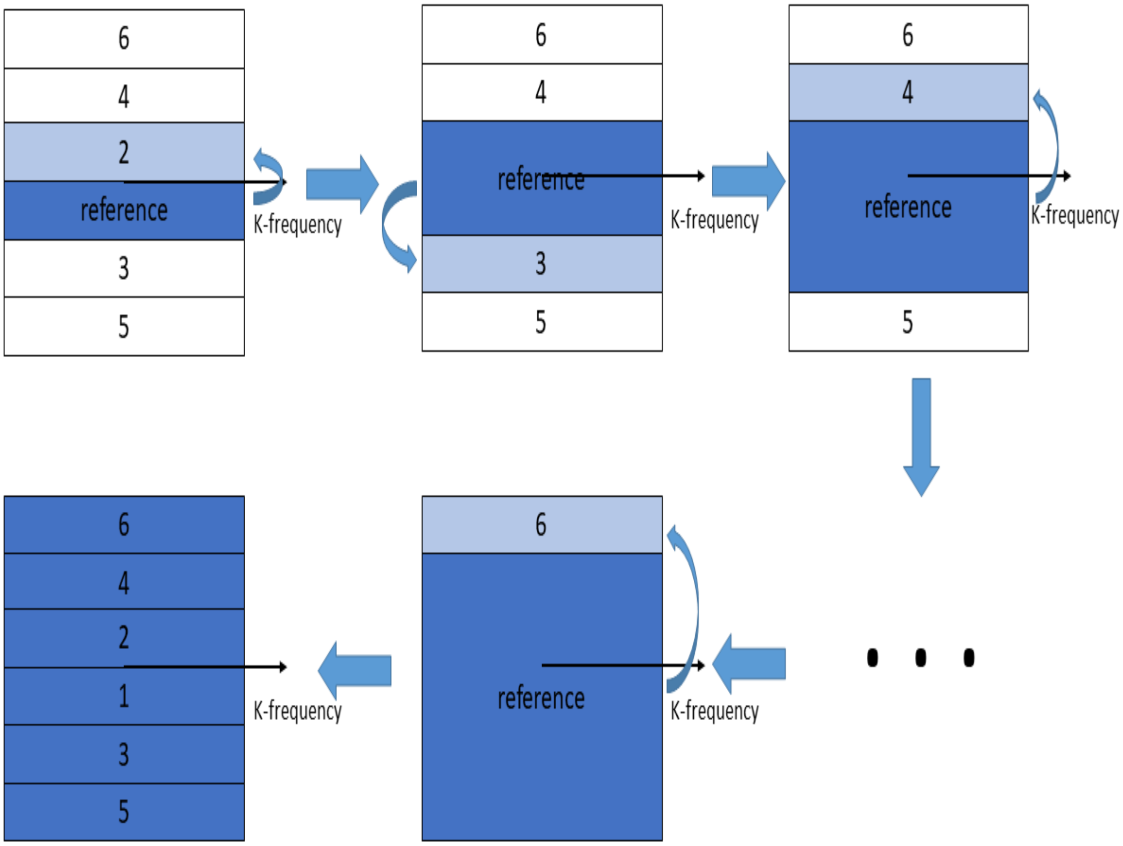

Figure 5.6: Search Strategy 3 of the proposed method. The blue segment is the reference segment, and the light blue one is the corresponding floating segment. The reference segment is enlarged after combining the previous corrected floating segment until all the segments are corrected. The neighboring symmetric segments are in turn chosen as the floating segments.

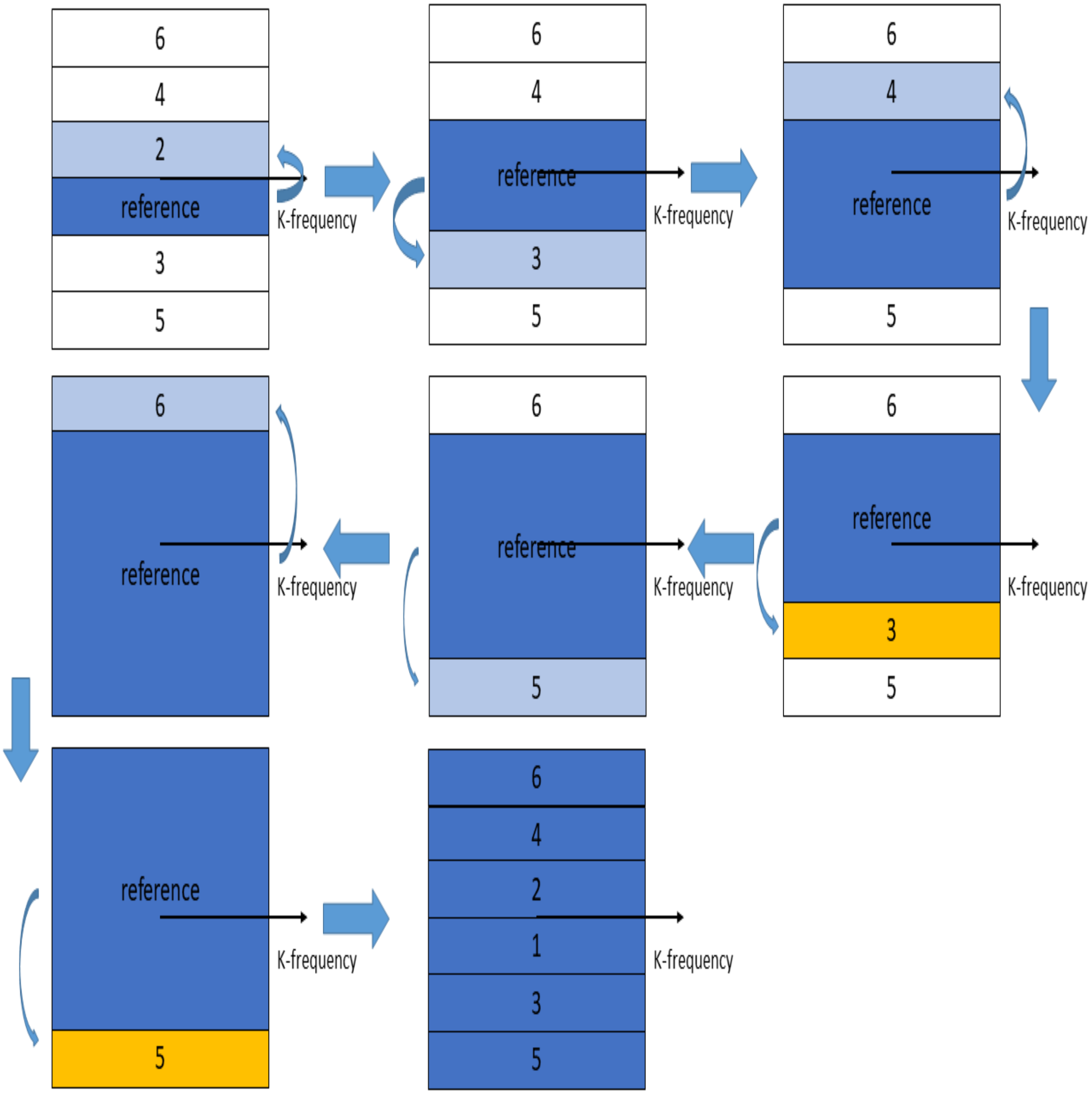

Figure 5.7: Search Strategy 4 of the proposed method. The blue segment is the reference segment, the light blue one is the corresponding floating segment and the yellow one is the segment corrected twice. Take segment 3 for example. Segment 3 and 4 are symmetric segments. After segment 3 and segment 4 are corrected in turn, the segment 3 is corrected again with the corrected segment 4 as part of the reference.

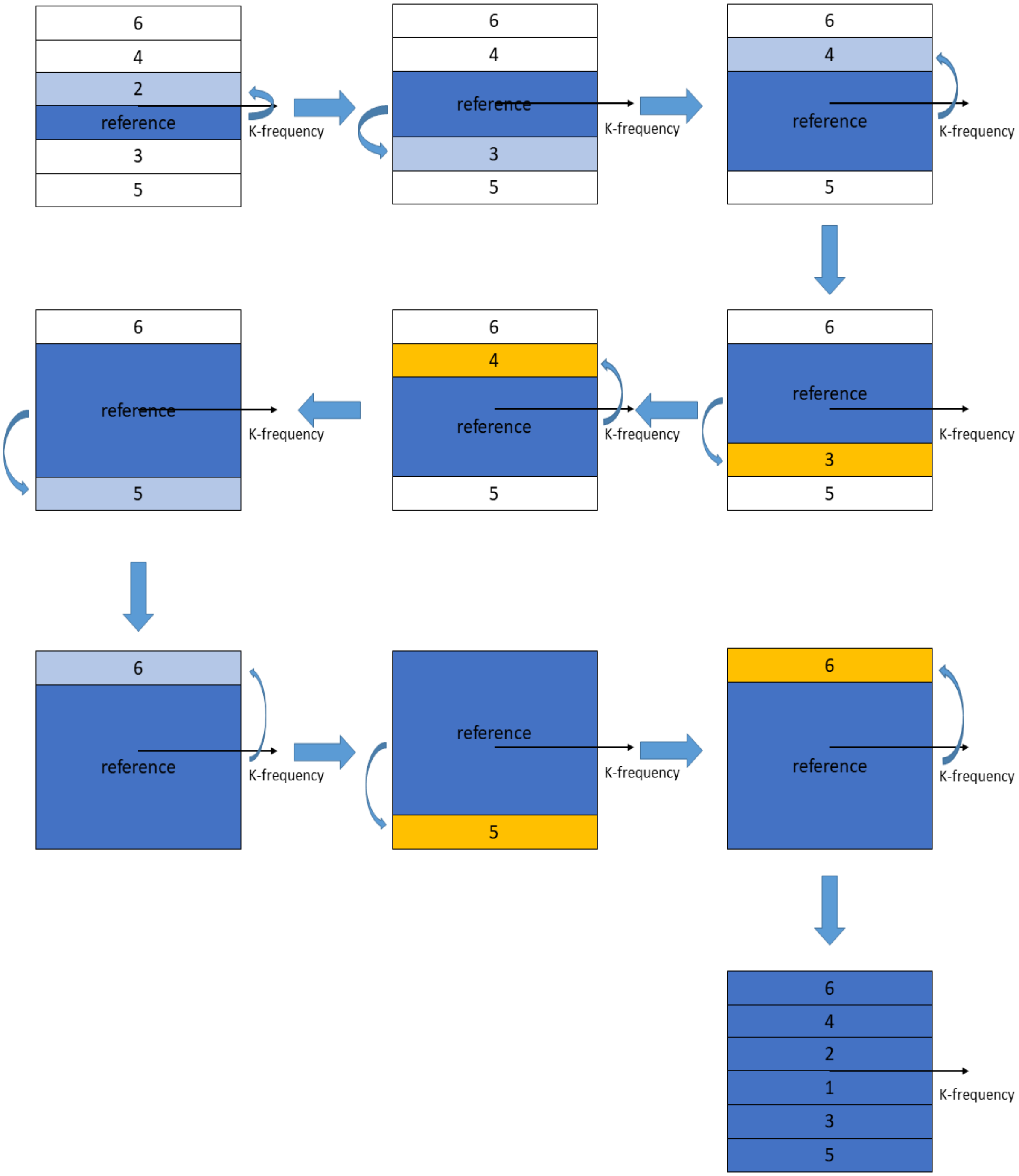

Figure 5.8: Search Strategy 5 of the proposed method. The blue segment is the reference segment, the light blue one is the corresponding floating segment and the yellow one is the segment corrected twice. The symmetric segments are corrected twice.

5.7 Simulations

To validate the proposed algorithm and compare the search strategies, simulations were conducted in this section. One motion-free real-experimental MRI gating cardiac image (complex pixels) was chosen as the reference image, whose size is 128 by 120. The reference image was acquired on a clinical 3T Siemens Verio scanner with balanced Steady State Free Precession (bSSFP) sequence 32-channel cardiac array coil at Auburn University MRI Research Center. The frequency domain of the reference image was separately divided evenly into 15, 12, 10 and 8 parts, corresponding to 8, 10, 12 and 15 lines in each segment, to simulate segments in k-space. Different search strategies of the proposed motion correction method were implemented to detect and correct the simulated translations. Two random values in the range from -10 to 10 pixels, which are big enough to model real motion, were generated to simulate two translations in each segment except the reference segment.

In this section, different search strategies are compared and some motion correction examples are shown.

5.7.1 comparison of search strategies

For each segment size (total of 4 different sizes), 10,000 random translational motion images were generated by the above processing. The 10,000 simulated images were separately processed by the above five search strategies, and the results were compared by the average estimation error for each segment and the average values of four image quality criteria. The motion correction accuracy was $\frac{1}{5}$ pixel here.

The average estimation error for segment j is given by:

$$\Delta x_j = \frac{1}{10000} \sum_{i=1}^{10000} |x_{i,j} - \hat{x}_{i,j}| \, , \Delta y_j = \frac{1}{10000} \sum_{i=1}^{10000} |y_{i,j} - \hat{y}_{i,j}| \, , \tag{5.17}$$

where Δx_j and Δy_j are the average estimation error of segment j in two-translational directions, $x_{i,j}$ and $y_{i,j}$ are the actual translations of the segment j from image i in two-translational directions, and $\hat{x}_{i,j}$ and $\hat{y}_{i,j}$ are the estimated translations of the segment j from image i in two-translational directions using the proposed method.

The average values of four image quality criteria were calculated— SSD (Sum of Squared Difference), IE (image entropy), EG (entropy of gradients of an image) and TV (total variation of an image). SSD (Eq (5.18)) compares one image with the reference image. The definition of image entropy is given by Eq (4.2) and Eq (4.3). The definition of the entropy of gradients of an image is given by Eq (4.5) and Eq (4.6). The definition of the total variation of an image is given by Eq (4.7) and Eq (4.8).

SSD is given by:

$$SSD = \sum_{\boldsymbol{x}=1}^{N} \left| I(\boldsymbol{x}) - I_{\text{ori}}(\boldsymbol{x}) \right|^2, \tag{5.18}$$

where $\boldsymbol{x}$ is the pixel index and N is the total number of pixels of the image.

For each segment size, the average estimation error for each segment and the average values of four image quality criteria, are given to compare the results. Table 5.1 to Table 5.8 show the results of different segment sizes.

Note: I_{ref} represents the reference image, I_{mot} represents the motion-corrupted image, I_{rec1} represents the reconstructed image using Strategy 1, I_{rec2} represents the reconstructed image using Strategy 2, I_{rec3} represents the reconstructed image using Strategy 3, I_{rec4} represents the reconstructed image using Strategy 4 and I_{rec5} represents the reconstructed image using Strategy 5. In the tables of average estimation error, the best entry of each row is marked as boldface. In the tables of average values of four criterion, the best entry of each column is marked as boldface. The motion-corrupted image comes from placing original random translational segments together, which is given by:

$$I_{mot} = \text{ifft}\big(\sum_{i=1}^{N} F_i(k,l)\big) \tag{5.19}$$

where $F_i(k, l)$ is the ith segment and N is the total number of segments.

Table 5.1: Average translational motion estimation errors (two directions Δ_x,Δ_y) of each k-space segment (8 lines) for each search strategy (pixel/unit)

Segment	Strategy 1	Strategy 2	Strategy 3	Strategy 4	Strategy 5
1	0.0998,1.8990	0.0998,1.8990	0.0650,1.1691	0.0615,0.6923	**0.0644,0.5356**
2	4.9890,5.0110	0.1774,1.8724	0.0603,0.4606	0.0602,0.4606	**0.0558,0.3620**
3	5.0391,5.0143	0.1291,2.0006	0.0736,1.2740	0.1468,0.4411	**0.1537,0.3837**
4	5.0318,5.0687	0.1597,2.1334	0.0692,0.4621	0.0637,0.3783	**0.0649,0.2570**
5	5.0217,4.9801	0.1831,2.5413	0.0789,0.9800	**0.1153,0.2986**	0.1202,0.3256
6	5.0286,4,9957	0.1785,3.1942	0.0814,0.4605	0.0980,0.2475	**0.0998,0.1887**
7	4.9305,5.0669	0.1680,3.8557	0.0961,0.7970	**0.0713,0.2394**	0.0766,0.3029
8	5.0587,5.0004	0.1600,3.4528	0.1398,0.4593	0.1731,0.2128	**0.1647,0.1852**
9	4.9750,5.0455	0.1703,3.0327	0.0985,0.7714	**0.1754,0.2096**	0.1844,0.3078
10	4.9994,5.0006	0.1929,2.7654	0.1880,0.4545	0.2362,0.1895	**0.2154,0.2011**
11	4.9730,4.9784	0.2079,2.5063	**0.0894,0.9387**	0.1939,1.2875	0.2008,1.0000
12	5.0472,4.9806	0.2630,1.5380	**0.2202,0.5570**	0.2076,0.7596	0.2196,0.5980
13	5.0237,4.9882	0.2729,1.6419	0.2018,0.9620	**0.1934,0.8191**	0.2392,1.1085
14	4.9548,5.0724	0.2869,1.4097	**0.2664,0.6443**	0.2977,1.8543	0.3055,1.4656

Table 5.2: Average values of four criteria of the reference image, the motion blurred images and the five reconstructed images from the five search strategies (8 lines segment)

Images	SSD	IE	EG	TV
I_{ref}	0	410.1539	879.8204	1.1352e-3
I_{mot}	1.8313e-10	448.4703	979.2290	1.2628e-3
I_{rec1}	1.3378e-10	415.4935	899.3643	1.1604e-3
I_{rec2}	1.1768e-10	413.3635	891.7397	1.1487e-3
I_{rec3}	1.3218e-11	411.9923	882.5268	1.1375e-03
I_{rec4}	5.2190e-12	410.7653	**881.7578**	**1.1367e-03**
I_{rec5}	**4.6205e-12**	**410.501**	881.8877	**1.1367e-3**

From Table 5.1 to Table 5.8, we can draw the following observations:

1. Comparing Strategy 1 with Strategy 2, the results of Strategy 2 have smaller average translational motion estimation errors and the average values of criteria. Average translational motion estimation errors for Strategy 1 are extraordinarily large, because the size of the reference segments does not include enough data to get accurate estimation and the reference segments are not extended.

Table 5.3: Average translational motion estimation errors (two directions Δ_x,Δ_y) of each k-space segment (10 lines) for each search strategy (pixel/unit)

Segment	Strategy 1	Strategy 2	Strategy 3	Strategy 4	Strategy 5
1	0.2134,0.2966	0.2134,0.2966	**0.0674,0.3207**	**0.0674,0.3207**	**0.0674,0.3207**
2	4.9520,4.9737	0.2863,0.3403	0.0609,0.3720	**0.0602,0.1781**	**0.0602,0.1781**
3	5.0099,5.0004	0.2869,0.3924	0.0748,0.1590	0.0748,0.1590	**0.0694,0.1619**
4	4.9899,5.0173	0.2787,0.5175	0.0709,0.4382	**0.0735,0.2651**	0.0760,0.2639
5	4.9925,4.9691	0.2745,0.6683	0.0963,0.1843	0.0943,0.1652	**0.0808,0.1736**
6	4.9876,5.0228	0.2535,1.3170	0.1051,0.4581	**0.1111,0.3079**	0.1185,0.3084
7	5.0102,5.0101	0.2353,0.9771	0.1338,0.3003	0.1255,0.2373	**0.1089,0.2459**
8	5.0057,5.0135	0.2172,0.7450	0.1279,0.4857	0.1191,0.3547	**0.1261,0.3562**
9	4.9760,5.0224	0.2170,0.6700	0.0897,0.3600	**0.0901,0.3016**	0.0903,0.3049
10	5.0127,5.0346	0.2144,0.6059	0.2131,0.4807	**0.1989,0.4595**	0.2106,0.4675
11	5.0420,5.0565	0.1734,0.6280	**0.1343,0.4503**	0.1249,0.6279	0.1243,0.6196

Table 5.4: Average values of four criteria of the reference image, the motion blurred images and the five reconstructed images from the five search strategies (10 lines segment)

Images	SSD	IE	EG	TV
I_{ref}	0	410.1539	879.8204	1.1352e-3
I_{mot}	5.4738e-11	434.0825	972.0623	1.2550e-3
I_{rec1}	2.1977e-11	413.5135	892.3260	1.1504e-3
I_{rec2}	5.8409e-12	409.5080	882.7683	1.1365e-3
I_{rec3}	4.7798e-12	410.7949	880.7689	1.1350e-3
I_{rec4}	**2.7349e-12**	**410.2985**	**880.5240**	**1.1348e-3**
I_{rec5}	2.7509e-12	410.3011	880.6121	1.1349e-3

Table 5.5: Average translational motion estimation errors (two directions Δ_x,Δ_y) of each k-space segment (12 lines) for each search strategy (pixel/unit)

Segment	Strategy 1	Strategy 2	Strategy 3	Strategy 4	Strategy 5
1	0.1197,0.1178	**0.1197,0.1178**	0.0758,0.4003	0.0758,0.4003	0.0758,0.4003
2	5.0288,5.0470	0.1910,0.1925	0.0543,0.3103	**0.0545,0.1863**	**0.0545,0.1863**
3	4.9700,5.0472	**0.2726,0.2728**	0.0798,0.8030	0.0798,0.8030	0.0840,0.7474
4	4.9429,4.9447	0.2548,0.3451	0.0812,0.4885	0.0809,0.3721	**0.0843,0.3635**
5	5.0067,4.9646	0.2083,1.5289	0.0800,0.8216	0.0790,0.7933	**0.0752,0.7521**
6	5.0066,5.0320	0.2108,1.2325	0.1253,0.6003	0.1174,0.4844	**0.1215,0.4728**
7	5.0257,5.0153	0.2073,0.9326	0.1058,0.7955	0.1098,0.7434	**0.1104,0.6950**
8	4.9647,4.9940	0.2034,0.7582	0.1606,0.5752	0.1546,0.4651	**0.1638,0.4525**
9	5.0350,5.0293	**0.1342,0.6749**	0.1423,0.9133	0.1308,0.8065	0.1295,0.7570

Table 5.6: Average values of four criteria of the reference image, the motion blurred images and the five reconstructed images from the five search strategies (12 lines segment)

Images	SSD	IE	EG	TV
I_{ref}	0	410.1539	879.8204	1.1352e-3
I_{mot}	4.6843e-11	430.2335	967.2813	1.2486e-3
I_{rec1}	2.1536e-11	411.6085	889.5606	1.1473e-3
I_{rec2}	7.3393e-12	**409.7032**	882.7113	1.1357e-3
I_{rec3}	9.0457e-12	409.7552	881.0210	1.1347e-3
I_{rec4}	7.4486e-12	409.8498	880.8988	1.1343e-3
I_{rec5}	**6.9332e-12**	409.8401	**880.6265**	**1.1341e-3**

Table 5.7: Average translational motion estimation errors (two directions Δ_x,Δ_y) of each k-space segment (15 lines) for each search strategy (pixel/unit)

Segment	Strategy 1	Strategy 2	Strategy 3	Strategy 4	Strategy 5
1	**0.0627,0.0546**	**0.0627,0.0546**	0.0729,1.3594	0.0729,1.3594	0.0729,1.3594
2	5.0165,5.0098	**0.0827,0.1088**	0.0552,0.1457	0.0544,0.1419	0.0544,0.1419
3	4.9549,5.0018	**0.1078,0.1671**	0.0685,1.0903	0.0685,1.0903	0.0679,1.0800
4	5.0214,5.1141	0.1545,1.0540	0.0891,0.3546	0.0654,0.3474	**0.0654,0.3453**
5	5.0166,4.9946	**0.1453,0.8106**	0.0843,0.9565	0.0845,0.9556	0.0922,0.9276
6	4.9673,4.9747	0.1174,0.5954	0.1035,0.3821	0.0859,0.3841	**0.0844,0.3785**
7	4.9842,4.9900	**0.1451,0.5392**	0.1112,0.8694	0.1185,0.8673	0.1284,0.8472

Table 5.8: Average values of four criteria of the reference image, the motion blurred images and the five reconstructed images from the five search strategies (15 lines segment)

Images	SSD	IE	EG	TV
I_{ref}	0	410.1539	879.8204	1.1352e-3
I_{mot}	3.9798e-11	428.3945	960.9661	1.2405e-3
I_{rec1}	2.3701e-11	413.3896	895.6266	1.15472e-3
I_{rec2}	1.0784e-11	**410.1553**	883.0794	1.1370e-3
I_{rec3}	1.0343e-11	410.8307	882.4583	1.1356e-3
I_{rec4}	1.0309e-11	410.8349	882.2986	1.1353e-3
I_{rec5}	**1.0138e-11**	410.8410	**882.1629**	**1.1351e-3**

2. The performance of Strategy 3 is better than Strategy 2, especially when the segment size is smaller. Even if average translational motion estimation errors of Strategy 2 are smaller when the segment size is larger, the difference of the average values of criteria between Strategy 2 and Strategy 3 is trivial. The reference starting from the low frequency contains more energy than the reference starting from the high frequency, which may explain the different performance between Strategy 2 and Strategy 3.

3. Strategy 4 and Strategy 5 always give the best results but with longer processing time, due to the second-time correction of some segments.

4. Strategy 3 gives similar but a little worse performance compared to Strategy 4 and Strategy 5. But Strategy 3 is more efficient. Strategy 3 is used for the next subsection and the Experiments section.

5. Some TV (total variation) values of the corrected images are smaller than the values of the reference image, which illustrates that the total variation criterion is not perfect. To our knowledge, there are no perfect criteria. If the criterion is replaced by other criteria, the results are similar but with higher computational load using more sinusoidal terms.

6. The average translational motion estimation errors may include three parts. The first part error comes from the non-ideal criterion, and the motion may be over-corrected by the criterion. The second part error arises from by the $\frac{1}{5}$ pixel motion correction accuracy of the proposed method. The last part error comes from non-perfect search strategy.

5.7.2 examples of the proposed method

In this subsection, four simulated motion-corrupted images generated by different segment sizes were corrected and reconstructed by the proposed method using search strategy 3. For each example, five sub-figures are included: (a)(b) the real and estimated motions combined with errors in horizontal and vertical directions, (c) the reference image, (d) the motion-corrupted image, (e) the reconstructed image. Figure 5.9 to Figure 5.12 show the four examples.

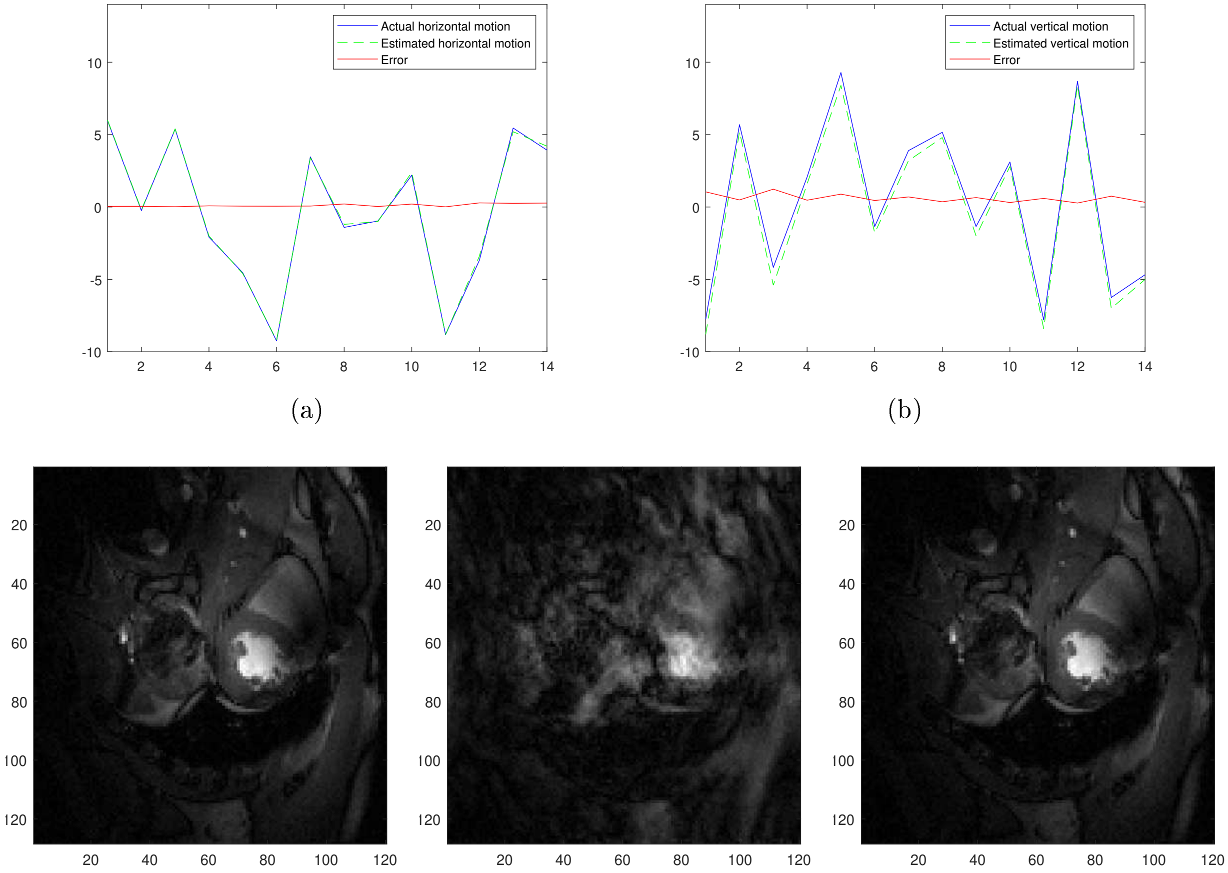

(a) (b)

(c) (d) (e)

Figure 5.9: Example 1 of the proposed method with segment size 8.

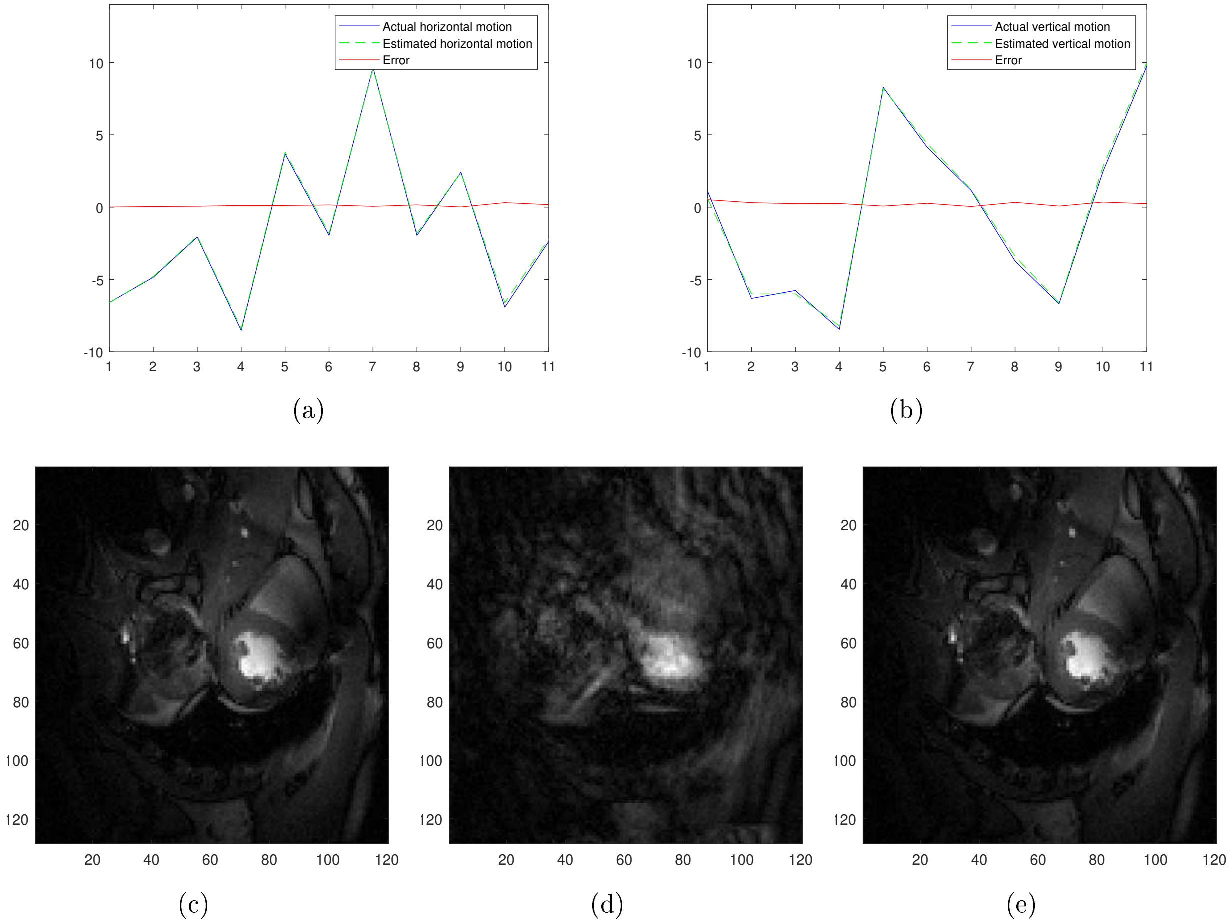

(a) (b)

(c) (d) (e)

Figure 5.10: Example 2 of the proposed method with segment size 10.

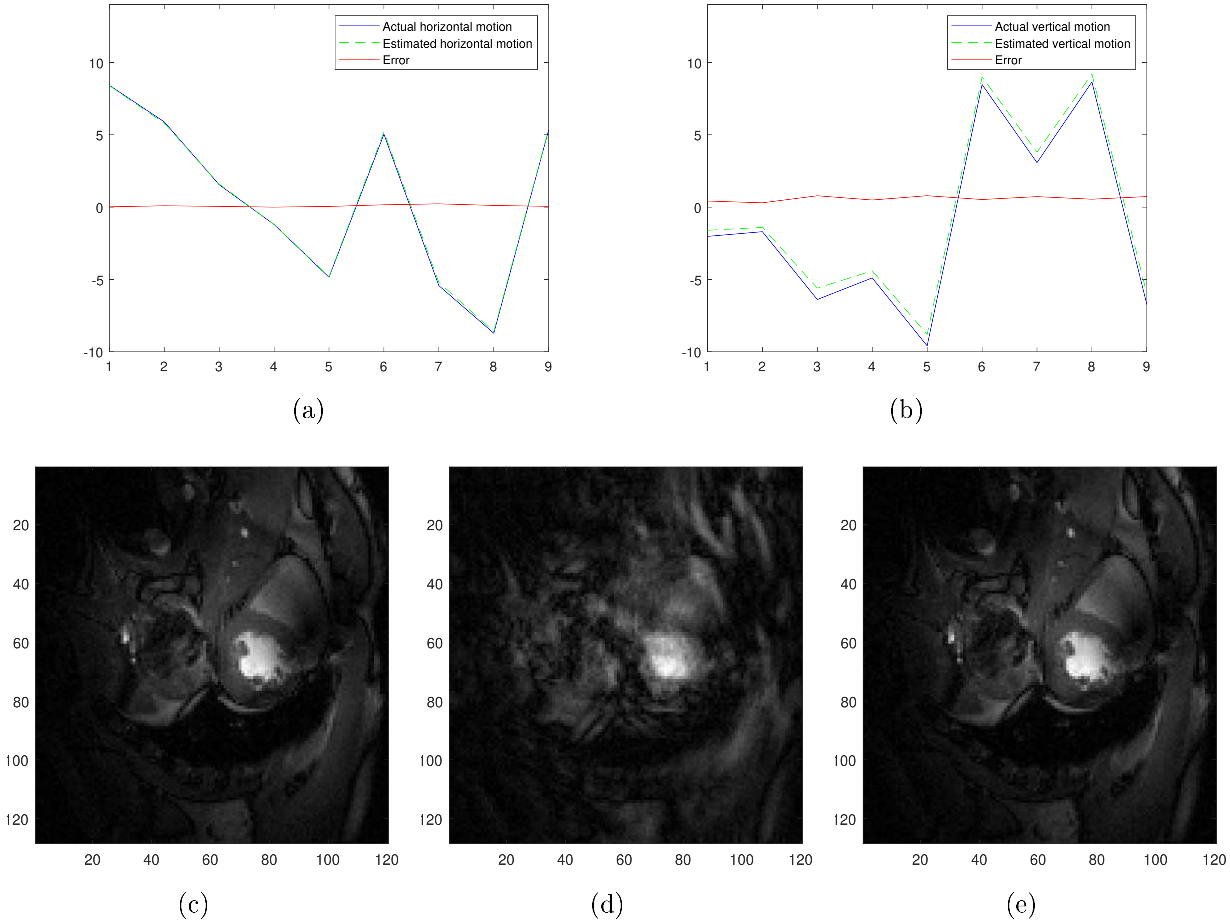

(a)

(b)

(c)

(d)

(e)

Figure 5.11: Example 3 of the proposed method with segment size 12.

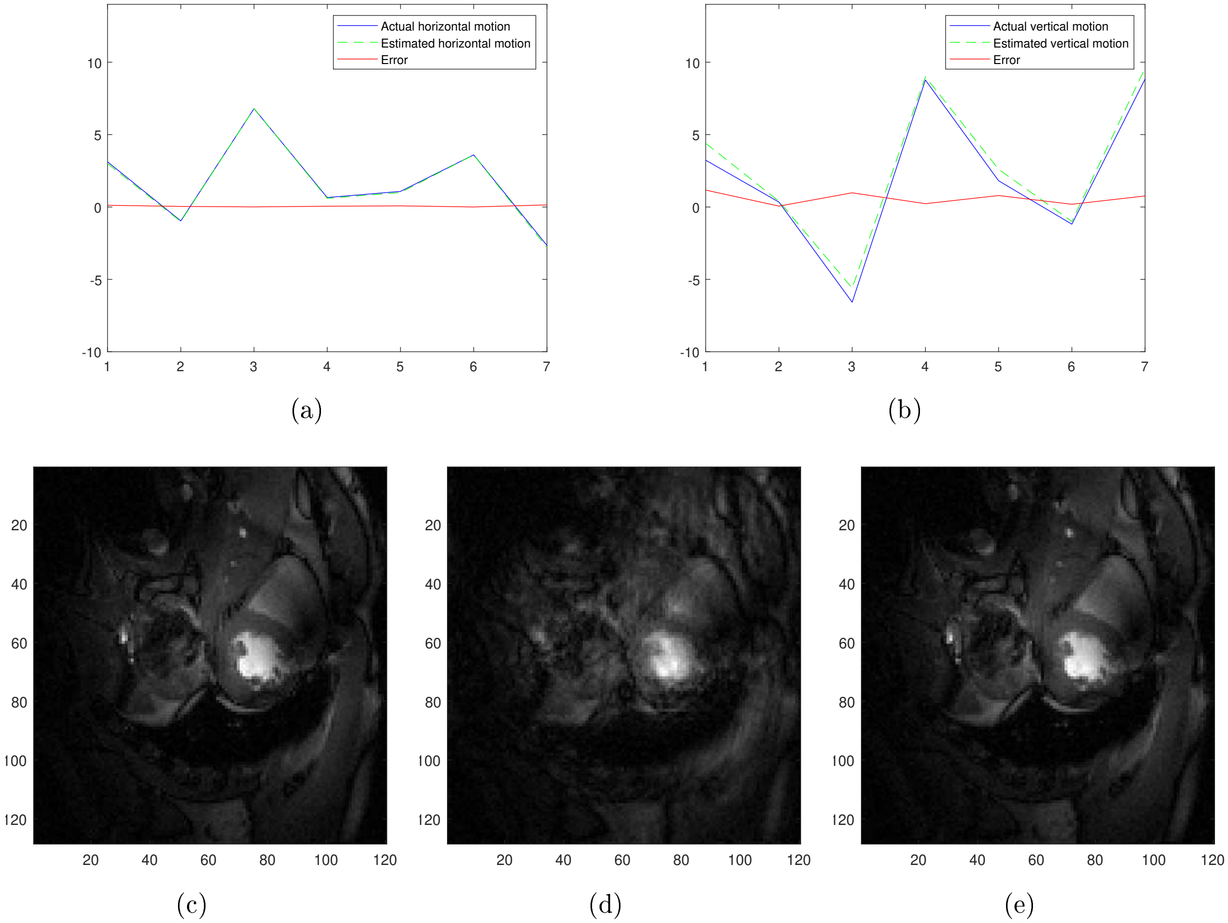

(a)

(b)

(c)

(d)

(e)

Figure 5.12: Example 4 of the proposed method with segment size 15.

Subfigures (a)(b) from the figures above illustrate that both estimated translations follow the actual translations, and the error is relative small. The horizontal translations are always better estimated than the vertical motion because the segment contains all the frequency components in the horizontal direction but only partial components in the vertical direction. The errors in the vertical direction mainly just shift the whole image a little.

Subfigures (e) from the figures above show the reconstructed image quality is noticeably improved by the proposed motion correction algorithm and the reconstructed images are almost the same with the reference image. All of these results show successful motion correction for any segment size.

5.8 Experiments

For validation of the proposed algorithm, MRI cardiac imaging experiments were conducted. Cardiac imaging consists of imaging of different cardiac phases. An external electrocardiogram (ECG) signal is a conventional tool to track the phase of the cardiac cycle during imaging. To reduce the effect of heart motion, the acquisition window for each cardiac phase must be short to decrease heart motion during the acquisition, which means that full k-space data cannot be collected in one cardiac cycle. Therefore, multiple cycles are needed to collect the data in the segment pattern, which consists of a certain number of phase lines. For each cardiac phase, the whole k-space data is collected from several cardiac cycles at the same cardiac phase. So only considering heart motion, we can treat cardiac phase imaging motionless due to the short acquisition window and quasi-periodicity of heartbeat. Breathing, which amounts to imposing a motion on top of heart motion, is a big challenge for cardiac imaging. This imposed motion can distort the image. Here we assume that the breathing can be approximated as two translations. Therefore, free-breathing cardiac imaging can be treated as the translational motion correction of each k-space segment, and breath-hold image without other motion can be treated as a no-motion reference image.

In this section, the scan sequence was the same as in the simulation section. The proposed method was used to reconstruct free-breathing real-experimental MRI gating cardiac data (Auburn University MRI Research Center) in each cardiac phase. The original images were distorted due to free-breathing motion. According to the record of the ECG device, the segment size of the frequency domain was chosen as 8 frequency (k-space) lines. Figure 5.13 shows the comparisons of breath-hold no-motion images, original free-breathing images, and reconstructed images from the original free-breathing images for two cardiac phases. The breath-hold no-motion images were acquired separately as reference images for comparison.

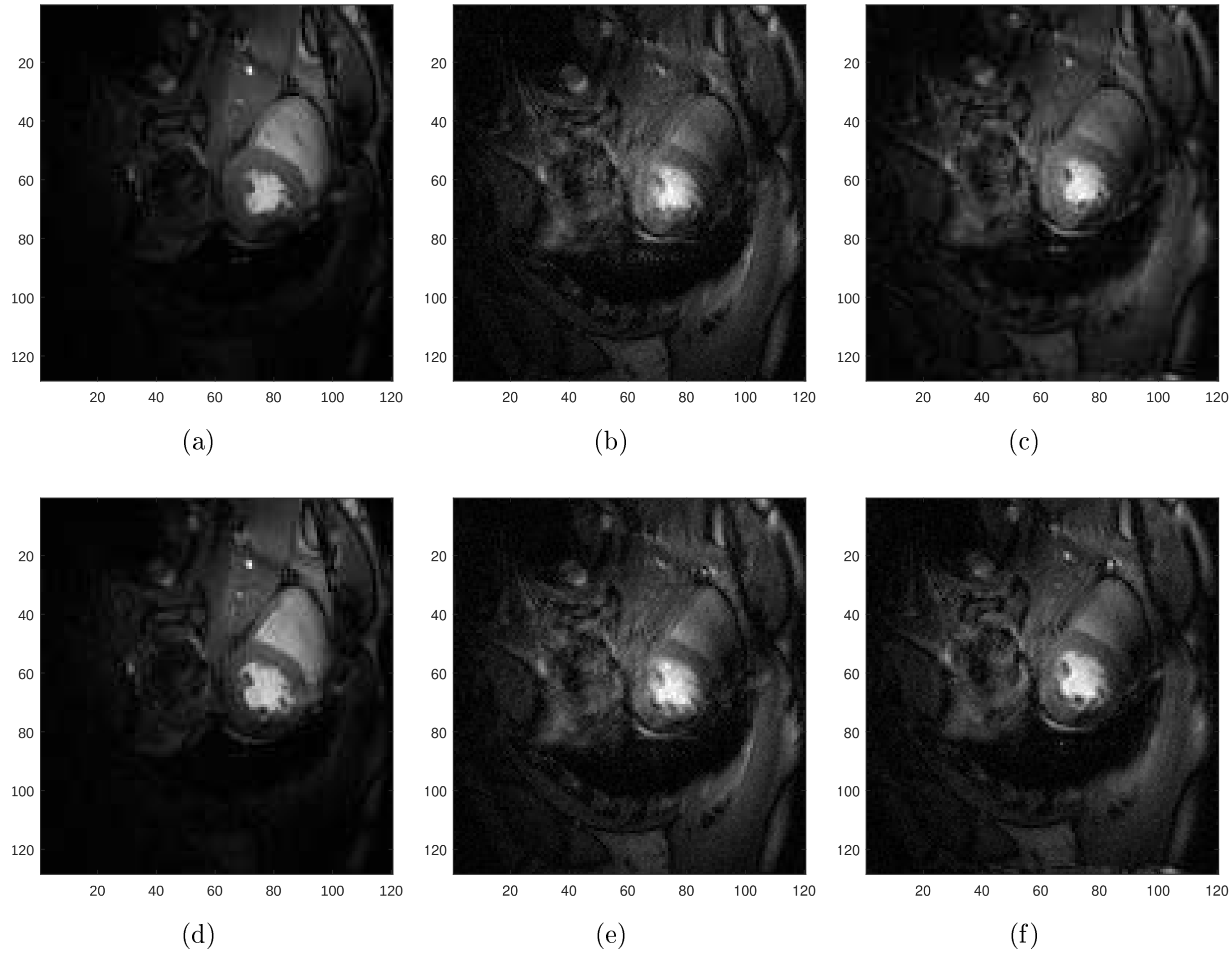

(a) (b) (c)

(d) (e) (f)

Figure 5.13: Comparison of breath-hold no-motion images, original free-breathing images and reconstructed images from the original free-breathing images for two cardiac phases. The first row is one cardiac phase, and the second row is the other cardiac phase. (a)(d) breath-hold no-motion images. (b)(e) original free-breathing images. (c)(f) reconstructed images from the original free-breathing images.

5.9 Discussion

Fig 5.13 shows that the reconstructed images reduce the blurs of the original images effectively, and more details are recovered in the heart region. However, some artifacts remain, especially in the region around the heart. We think the real-world breathing motion gives rise to the remaining artifacts. Real breathing motion is not exactly a two-directional translation in a 2D plane. It includes some through-plane and non-rigid motion, which is beyond the scope of the proposed method.

The proposed method is efficient. The whole process time was around 0.8 s implemented in MATLAB on an 8 GB RAM Intel Core i7-3630QM 2.40 GHz CPU processor machine. Thus, it can be used in real-time processing.

Chapter 6

Motion Correction of Magnitude MR Images using Generative Adversarial Networks

Although the previous proposed methods can correct motion effectively and efficiently, they both require complex-valued raw data. However, raw data is not usually preserved in a clinical environment. In this case the previous two methods cannot be used. In this chapter, we present a novel data-driven motion correction method for magnitude MR images using generative adversarial networks (GANs). GANs (pix2pix model) are implemented to reduce motion artifacts and reconstruct motion-corrupted images through adversarial training between generator and discriminator networks to estimate a motion-corrected image that is close to the reference image. The training set is made of image pairs consisting of motionless reference images and corresponding motion-simulated images. The proposed method is validated by a simulated motion test set and a real motion (experimental) test set.

This chapter is organized as follows: 6.1 introduction to artificial neural networks, 6.2 introduction to convolutional neural networks, 6.3 generative adversarial networks (pix2pix model) basics, 6.4 dataset and training, and 6.5 results.

6.1 Artificial neural networks

Artificial neural networks (ANNs) are widely used in machine learning. In general, an ANN is made of a collection of connected computational units, called artificial neurons, which simulates biological neurons. Artificial neurons are arranged in layers. Data enters a neural network at the input layer, and predictions of the network are generated at the output layer. One or more hidden layers exist between the input and output layer. In general, the basic implementation of a neural network is to provide reasonable predictions by training a set of labeled data, called training data. During a training process, parameters of a neural network (weights) are tuned by comparing predictions of training data feeding through the network and actual labeled training data, until the network can provide good predictions of the training data. The training process can also be considered as learning a data pattern. After the data pattern is learned, the network is ready to give predictions for unseen data (non-labeled data). Figure 6.1 shows a multilayer perceptron neural network.

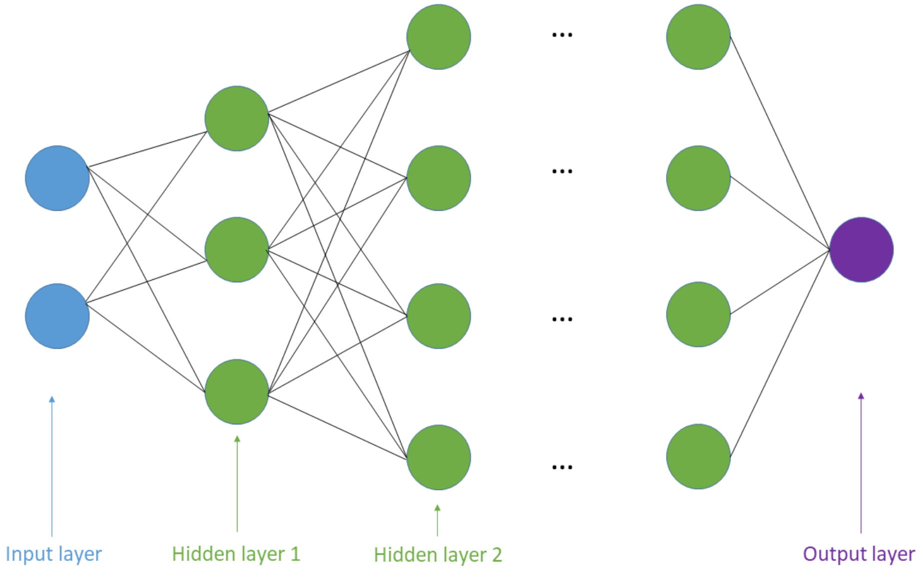

Figure 6.1: One multilayer perceptron neural network. The blue neurons represent the neurons from input layer, the green neurons represent the neurons from hidden layers, and the purple neuron represent the neurons from output layer

For ANNs, at least two types of data sets are needed—training set and test set. A training set is the set of examples used for learning. In this dataset, input data are associated with expected output. A test set is the set of examples used to evaluate the performance of a trained neural network. Sometimes a neural network may require a validation set, but we will only use training set and test set in this chapter.

A basic training process of the multilayer perceptron neural network is discussed here. The process consists of two parts—forward propagation and backward propagation.

For forward propagation, the output vector $\hat{y}$ is calculated layer by layer from the input vector X:

$$\hat{y} = (f_n, f_{n-1}, ..., f_1)(X; W), \tag{6.1}$$

where $f_n, f_{n-1}, ..., f_1$ are activation functions and W is the weight matrix. For each layer, two kinds of calculation are conducted—a linear transformation of the output of the layer and a followed nonlinear function called the activation function. Consider the k_{th} layer as an example.

$$z^{(k)} = o^{(k-1)} W^{(k-1)}, \tag{6.2}$$

where $z^{(k)}$ is the linear transformation of the output of the previous layer, $o^{(k-1)}$ is the output of the $(k-1)_{th}$ layer, and $W^{(k-1)}$ is the weight vector from the $(k-1)_{th}$ layer to the k_{th} layer. The output of the activation function is given by:

$$o^{(k)} = f_k(z^{(k)}), \tag{6.3}$$

where $o^{(k)}$ is the output of the k_{th} layer. Sigmoid, Tanh, ReLU, and Leaky ReLU are the commonly used activation functions.

After $\hat{y}$ is calculated from forward propagation, the loss function is needed to measure the difference between $\hat{y}$ and the labeled output. The task of the training process is to update weights to optimize the prediction of the neural network, which is equal to minimizing the loss function. A backward propagation gradient descent method from the output layer to the input layer is needed. By using the chain rule of derivatives, the gradients of the loss function with respect to all the weights are calculated, and all the weights are updated using gradient descent to minimize the loss function. This is the basic training process for ANNs.

Due to the high computational load, the development of ANNs was slow. But recently, thanks to parallel computation processors (GPUs), ANNs have developed more rapidly.

6.2 Convolutional neural networks

In general, for image neural networks, each pixel of the image is used as the input of the network. If the neurons are fully connected, the computational load is very high, which is not acceptable for typical image sizes. In addition, the huge number of weights will result in overfitting easily. In order to prune the extra connections, convolutional neural networks (CNNs) have been proposed to preserve the spatial relationships of the input images. CNNs are built with a layer structure, and input is fed through layer by layer with neurons in each layer only calculating a small part of the previous layer [62]. CNNs consist of four types of layers: convolutional layer, activation layer, pooling layer, and fully-connected layer. Each type of layer has certain basic functions. A simple CNN structure is shown in Figure 6.2.

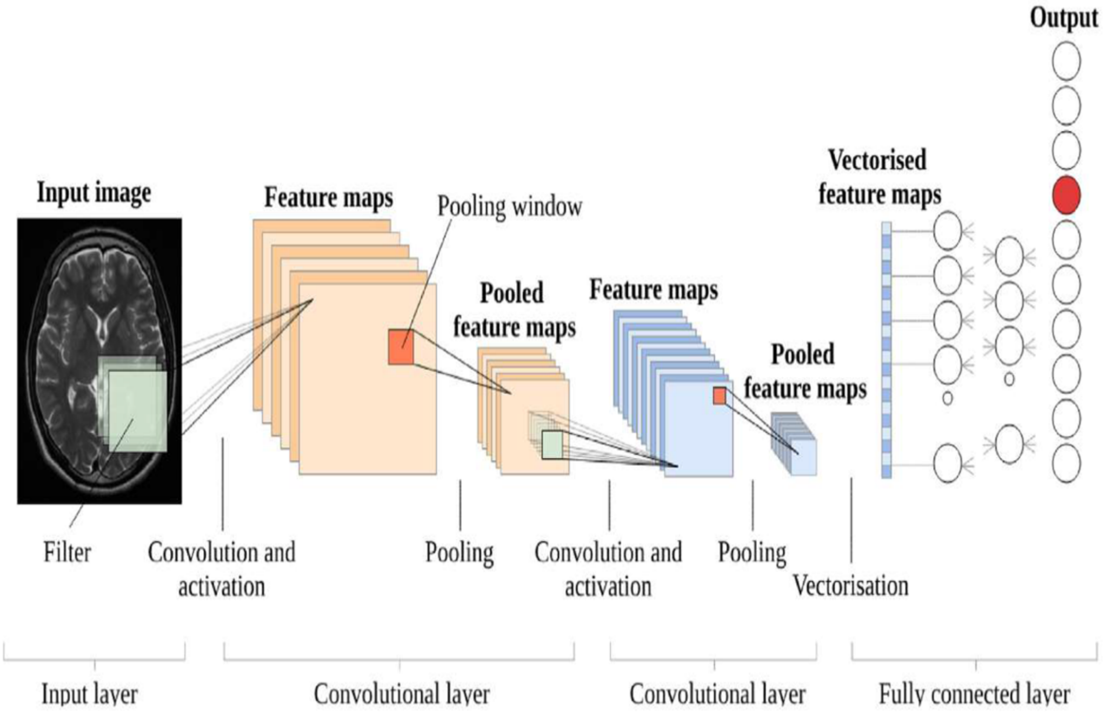

Figure 6.2: Example of a convolutional neural network. (Figure 6.2 is from [62].)

convolutional layer

The convolutional layer is used to compute the convolution between a small size filter and a local region of the input layer or the output activation from the previous layer. The small size filter (3×3 or 5×5) slides all over the input layer or the output activation from the previous layer to detect the same feature from the whole image. One convolutional layer may consist of multiple filters with different weights (parameters) in each filter, and each filter performs the above calculation. Each filter presents a feature of the input image, like a horizontal line or corner. Due to the structure where the same filter slides over the whole image, the number of weights needed to be trained is drastically reduced.

activation layer

The output from the convolutional layer is fed through the activation layer by calculating element by element. The most popular activation function is ReLU, defined as $max(0, x)$.

pooling layer

The pooling layer is used to perform a downsampling operation, which is always inserted between the successive convolutional layers. The max pooling, which is the most common pooling operation, preserves a max value from each neighboring 2×2 region, and discards 75% of the activations. The pooling operation preserves the important features while reducing the size of the feature map.

fully connected layer

All the activations from the previous layer are fully connected by the fully connected layer. The fully connected layer is the same as the ANNs discussed in the previous section. It generates the final output.

6.3 Generative adversarial networks (pix2pix model)

Generative adversarial networks (GANs) have been very successful since they were introduced by Goodfellow et al. [35] in 2014. GANs are widely used in generating photorealistic images [111], implementing super-resolution [55], and modeling patterns of motion in video [94] [84]. GANs include two models: a generator model G and a discriminator model D. The generator model G tries to generate model distribution $G(z)$ from random noise z to match the actual data distribution p_{data}. The discriminator D tries to learn to distinguish the input from the model distribution $G(z)$ or the actual data distribution. The objective of G is to fool D, and to make D make a mistake. The training process of GANs is like a fight between the generator and the discriminator. An example of a GAN is shown in Figure 6.3.

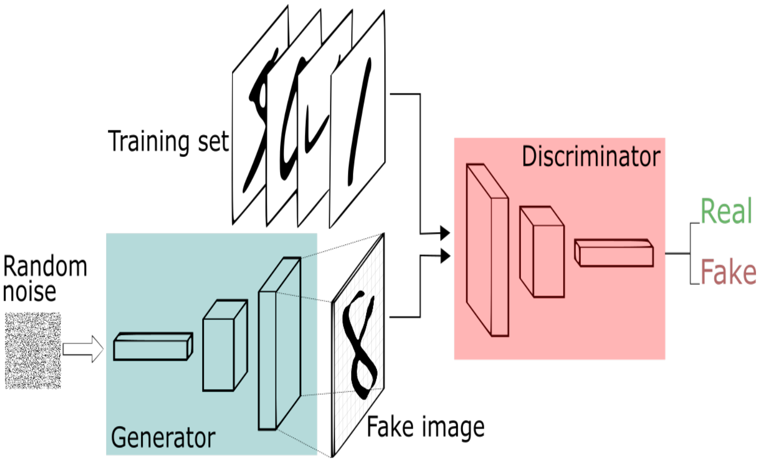

Figure 6.3: An example of a GAN. (Figure 6.2 is from `https://skymind.ai/wiki/generative-adversarial-network-gan`.)

Our task is to make the generator's distribution p_g equal to the actual data distributionp_{data}. Input random noise is represented as z with density $p_z(z)$, and the data space generated by the generator is represented as $G(z)$. $D(x)$ is a scalar, which represents the probability that a sample is from the actual data x with density p_{data} rather than $G(z)$. D is trained to provide the maximum probability to label correctly the actual data x versus the generated data $G(z)$, and G is trained to minimize $\log(1 - D(G(z)))$, so the value function $V(G, D)$ can be represented mathematically as [35]:

$$\min_G \max_D V(D, G) = \mathbb{E}_{x \sim p_{\text{data}}(x)} [\log D(x)] + \mathbb{E}_{z \sim p_z(z)} [\log(1 - D(G(z)))] . \qquad (6.4)$$

The objective function is given by:

$$\mathcal{L}_{GAN}(G, D) = \mathbb{E}_{x \sim p_{\text{data}}(x)} [\log D(x)] + \mathbb{E}_{z \sim p_z(z)} [\log(1 - D(G(z)))] . \qquad (6.5)$$

The global optimum for Eq 6.4 is $p_g = p_{\text{data}}$, which accomplish our objective. For a detailed discussion of the training process and proof, see [35].

For an unconditional GAN, there are no restrictions or control over the generated data, which may introduce large errors in some cases. Conditional generative adversarial nets (cGANs) were proposed to handle this problem [70] by providing some extra information y to both generator and discriminator. This additional y constrains the generator to generate a restricted class of data. An example of a cGAN is given in Figure 6.4.

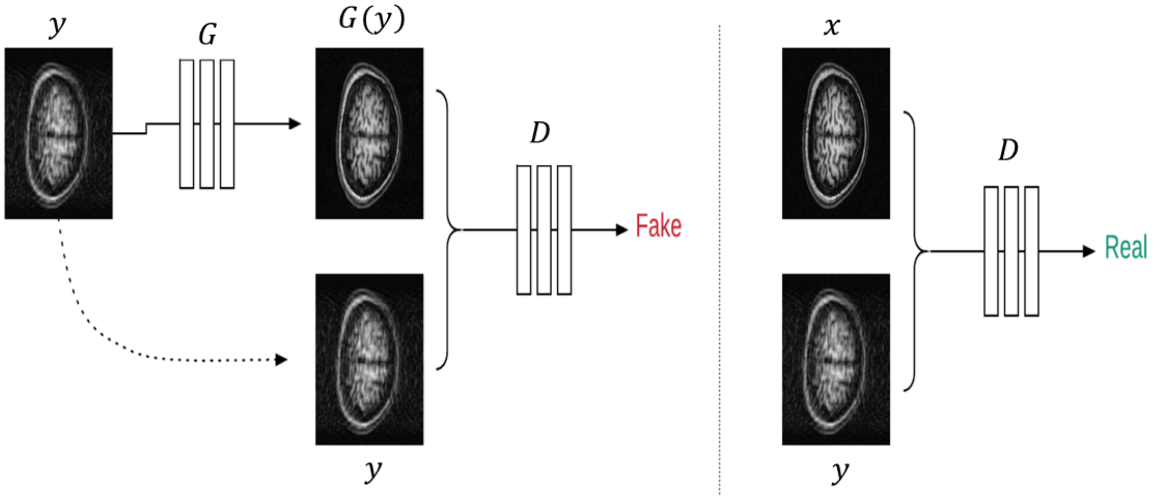

Figure 6.4: An example of a cGAN. The discriminator D is trained to distinguish the tuple between motion-corrected image $G(y)$ and motion-corrupted image y from the tuple between motionless image x and motion-corrupted image y. The generator G is trained to fool the discriminator D. Both the generator G and discriminator D can access the motion corrupted image y in the cGAN.

The objective function of cGANs is given by [50]:

$$\mathcal{L}_{cGAN}(G, D) = \mathbb{E}_{y,x}\left[\log D(y, x)\right] + \mathbb{E}_{y,z}\left[\log(1 - D(y, G(y, z)))\right], \tag{6.6}$$

where D tries to maximize the objective function and G tries to minimize it, so the desired G^* is given by [50]:

$$G^* = \arg\min_G \max_D \mathcal{L}_{cGAN}(G, D). \tag{6.7}$$

The pix2pix model add another term to the objective function Eq (6.7):

$$\mathcal{L}_{L^1}(G) = \mathbb{E}_{x,y,z}\left[||x - G(y,z)||_1\right], \tag{6.8}$$

so the final objective function is given by [50]:

$$G^* = \arg\min_G \max_D \mathcal{L}_{cGAN}(G,D) + \lambda\mathcal{L}_{L^1}(G). \tag{6.9}$$

The L^1 term does not change discriminator's function, but it forces the generated data from the generator to be close to x (ground truth) in an L^1 way.

6.4 Dataset and training

A pix2pix model requires pairs of images as the training set: motionless images and corresponding motion-corrupted images. 8000 2D images were acquired from 3D datasets of 276 subjects in the Autism Brain Imaging Data Exchange (ABIDE) dataset [23] to be motionless images in the training set. The corresponding motion-corrupted images were generated from these motionless images. Motion was simulated in k-space, according to the properties of the Fourier Transform. Each k-space line (along phase encode direction), was modeled with two random translations within ±12 pixels and one random rotation angle within ±12° . The center k-space phase lines (randomly chosen from 20 to 60 lines) were preserved without motion corruption to keep the basic image structure.

Two test sets were used to validate the proposed method. One test set—the simulation test set—includes 1780 simulated motion-corrupted images, which were generated by modeling motion of no-motion images in another subset of the ABIDE dataset (53 subjects). The other test set—the experimental test set—includes 200 real motion-corrupted images from two subjects. Six datasets were acquired by a standard vendor-supplied MP-RAGE sequence with resolution 1 mm isotropic and flip angle = 9° on Siemens Verio 3T Scanner at Auburn University MRI Research Center. The subjects were instructed to perform no motion and head motion to separately acquire motionless images (reference) and real motion-corrupted images.

For the pix2pix model training, minbatch Adam solver was used with learning rate = 0.0002, and momentum parameters were $\beta_1 = 0.5$, $\beta_2 = 0.999$. The network was trained over 200 epochs (40 hours) on an NVIDIA Tesla P100 GPU.

6.5 Results

In this section, we use the simulated test set to evaluate quantitatively the accuracy of the motion-corrected images using the proposed method. We show several examples of applying the proposed motion correction method on the simulated motion-corrupted images and real motion-corrupted images.

Three metrics—structural similarity index (SSIM), sum of absolute differences (SAD), and sum of squared difference (SSD)—were evaluated to compare the motion-corrupted images and the motion-corrected images.

SSIM is given by [96]:

$$SSIM = \frac{(2\mu_x\mu_y + c_1)(2\sigma_{xy} + c_2)}{(\mu_x^2 + \mu_y^2 + c_1)(\sigma_x^2 + \sigma_y^2 + c_2)}, \tag{6.10}$$

where μ_x and μ_y are the mean of the images, σ_x and σ_y are the variance of the image, x and y present two images to be compared, and c_1 and c_2 are small constants to provide calculation of stability. For SSIM, high values mean two input images are similar, but for SAD and SSD, the low values mean two input images are similar. Table 6.1 compares the average metrics between the motion-corrupted images and the motion-corrected images with the same reference images. Each entry in the table is the average value of all the 1780 cases in the simulation test set.

Results of motion correction on five simulation datasets from the simulation test set are shown in Figure 6.5. For comparing the error images (the absolute value of the difference

Table 6.1: Average values of three metrics of the motion-corrupted images and the motion-corrected images

Images	SSIM	SAD	SSD
I_{mot}	0.6538	5.9593	192.2482
I_{rec}	0.6997	5.1133	134.4986

between the reference and input image), we use two rows for each dataset. The first row consists of three images from left to right: motionless image (reference), motion-corrected image, and error image. The second row consists of three images from left to right: motionless image (reference), motion-corrupted image, and error image. Figure 6.6 shows the results of motion correction on two experimental datasets from the experimental test set. The first column shows motion-corrupted images generated by subject motion in the experiment; the second column shows no-motion images generated by motionless subject in the experiment; the third column shows the motion-corrected images through the pix2pix model.

Figure 6.5 and Figure 6.6 show several examples of applying the proposed motion correction method on the simulated motion-corrupted images and real motion-corrupted images. The motion-corrected images indicate that our method was able to eliminate motion artifacts and to preserve the sharp boundaries. In Figure 6.5, the corrected images recovered almost all the details of the reference images. In Figure 6.6, the blurred edges became sharp and the corrected images recovered most of the details of the reference images, but there were some differences between the reference images and the corrected images.

One important note is that the error of the fifth dataset in Figure 6.5 is larger than other datasets, due to large rotation angles of the motion-corrupted image during the motion simulation. These large angles lead to the corrected image having a relative angle to the reference image. If a registration is implemented between the reference image and the corrected image, the error will be smaller. We think the relative distance between reference images and motion-corrected images has an impact on the metrics calculated in Table 6.1. The metrics can be improved by performing registration for each pair of images.

Another important note concerns the reasons for the errors in the corrected images in Figure 6.6. Two explanations may be given for this. First, the subjects' position changed during the experiment. A small position change between two scans can lead to mismatch between motion-corrupted images and reference images. Second, information is lost due to through-plane motion. Some through-plane motion is almost inevitable when subjects performed motion, which leads to some information being lost in the reference plane and some information being obtained from other planes.

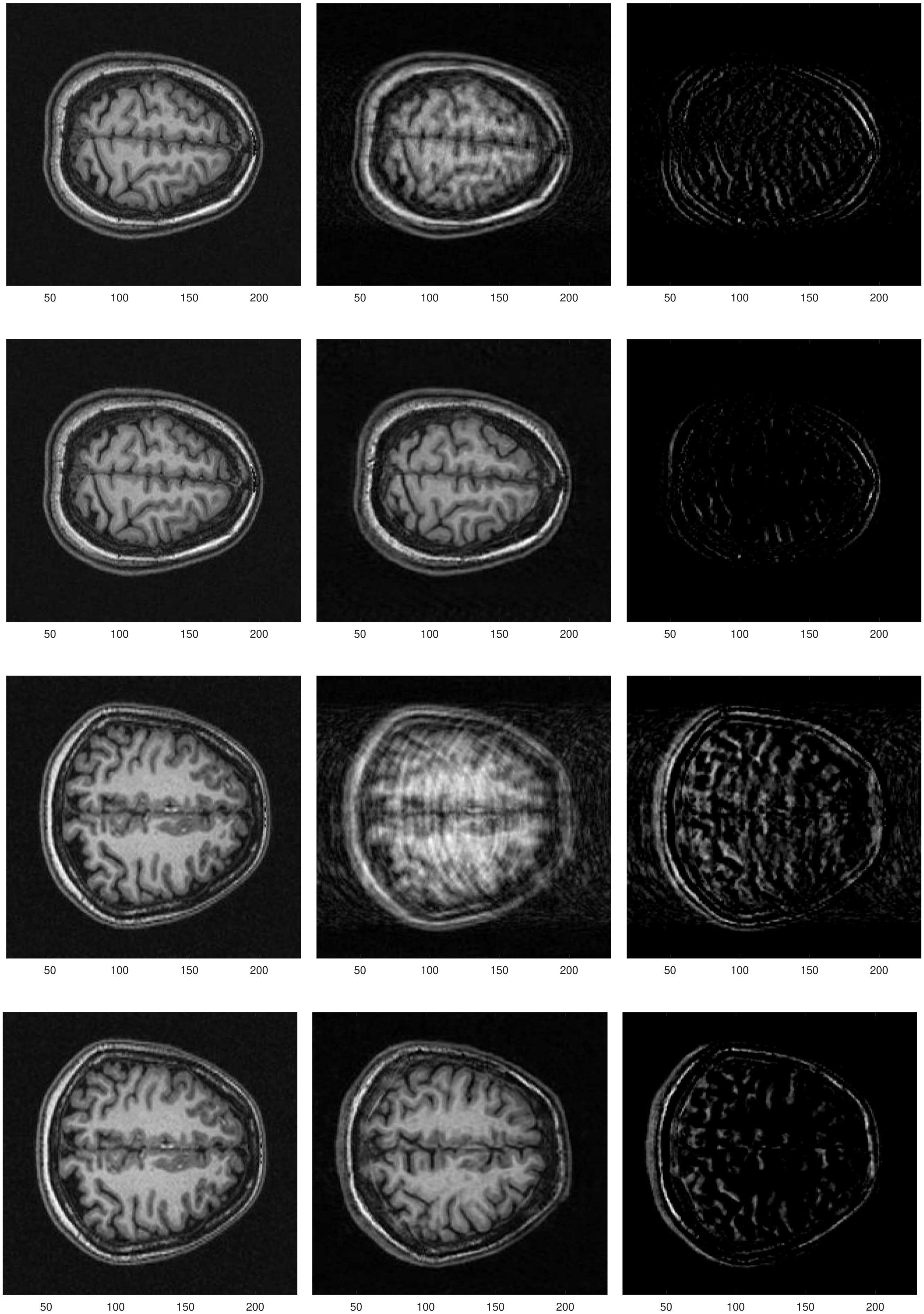
50 100 150 200
50 100 150 200
50 100 150 200
50 100 150 200
50 100 150 200
50 100 150 200
50 100 150 200
50 100 150 200
50 100 150 200
50 100 150 200
50 100 150 200
50 100 150 200

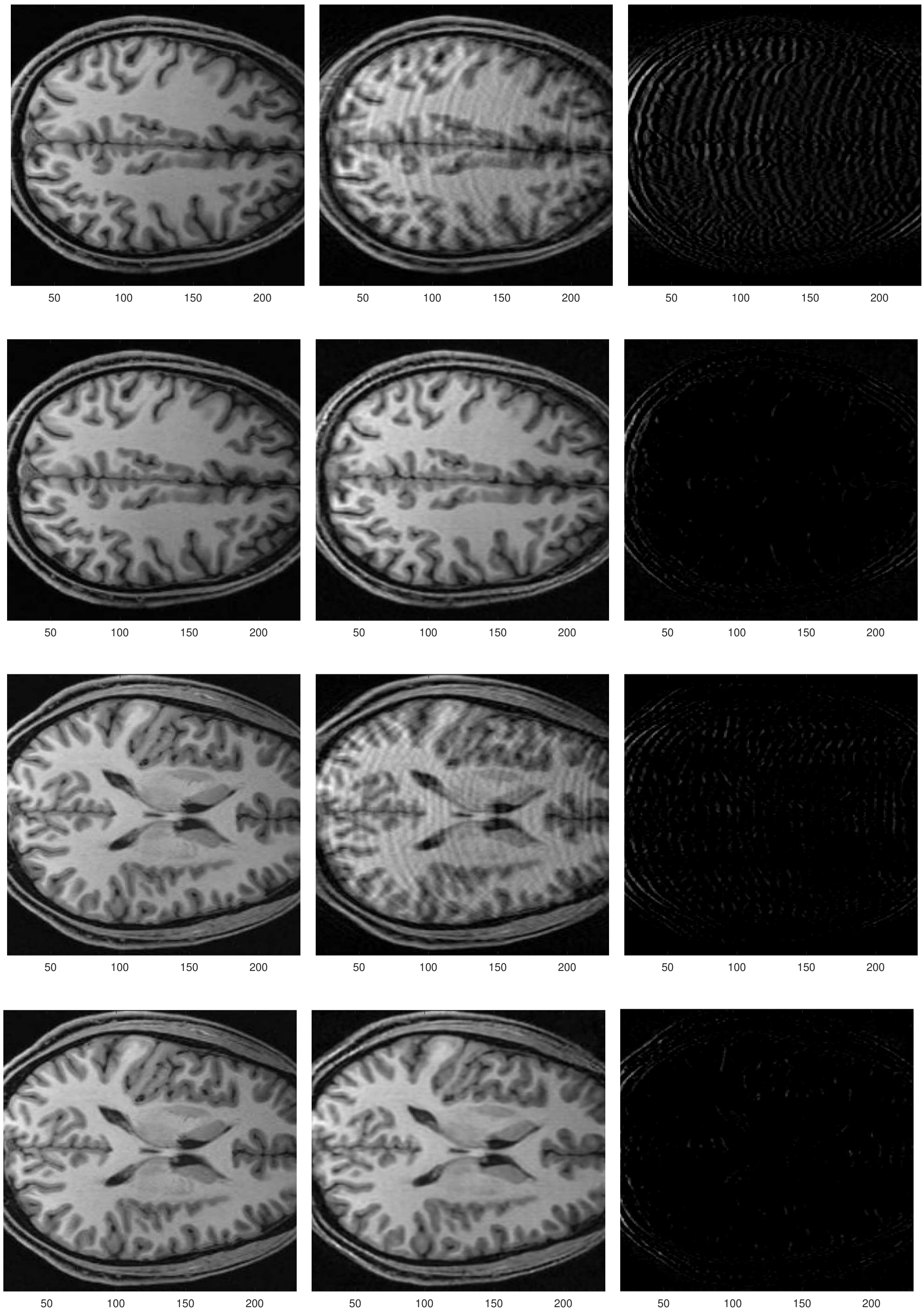
50
100
150
200
50
100
150
200
50
100
150
200
50
100
150
200
50
100
150
200
50
100
150
200
50
100
150
200
50
100
150
200
50
100
150
200
50
100
150
200
50
100
150
200
50
100
150
200

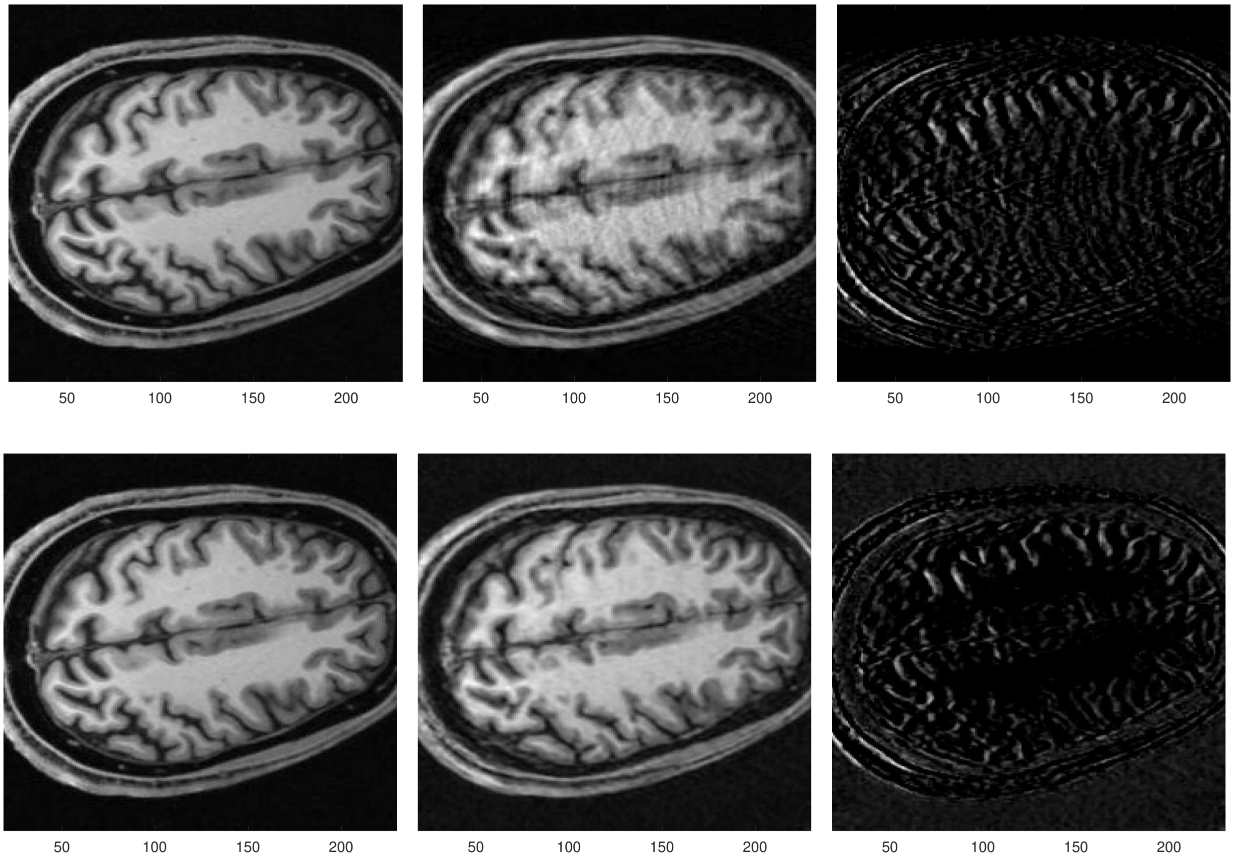

Figure 6.5: Results of motion correction on five simulation datasets from the simulation test set. For each dataset, we use two rows to compare the results. The first row consists of three images from left to right: motionless image (reference), motion-corrupted image, the absolute value of the difference between the reference and motion-corrupted image. The second row consists of three images from left to right: motionless image (reference), motion-corrected image, the absolute value of the difference between the reference and motion-corrected image.

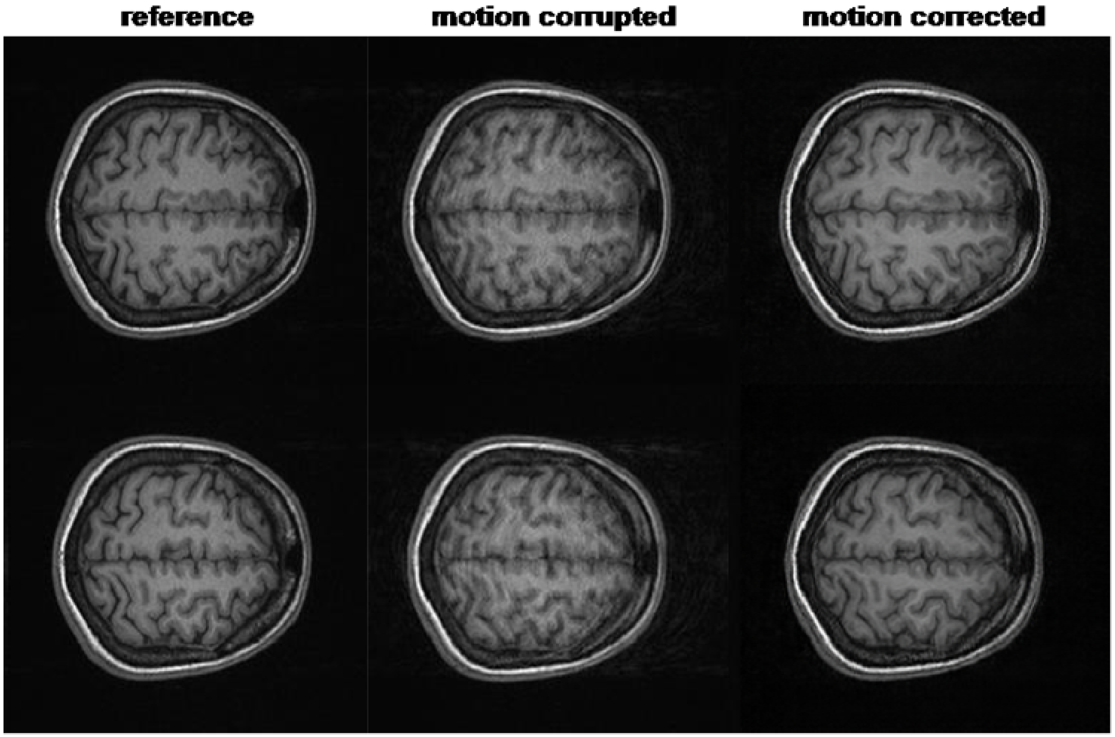

Figure 6.6: Results of motion correction on two experimental datasets from the experimental test set. The first column shows no-motion images generated by subject motion in the experiment; the second column shows motion-corrupted images generated by motionless subject in the experiment; the third column shows the motion-corrected images through pix2pix model.

Chapter 7

Conclusions

We have developed three methods to correct MRI motion retrospectively. These three methods have their own characteristics and scope of application. The autofocusing method using global motion estimation can correct rigid motion for each k-space phase line. This method required raw k-space data with the acquisition order, and the processing is relatively slow compared to the other two methods. The method based on fast robust correlation can also handle rigid motion but for each k-space segment. The main advantage of this method is that it can process the data efficiently. However, this method cannot make line-by-line correction, which may not be precise enough in some applications. Unlike the first two methods, the method using GANs does not require the raw k-space data. This method can also perform rigid motion correction efficiently, if the network has already been trained. This technique may occasionally generate images with phantom features that have no correspondence in the actual object. This is one of the biggest problems for this method, which may hinder diagnosis and scientific research. We summarize below the contributions and discoveries related to the three methods.

We developed an autofocusing motion correction method using global motion estimation to address the two challenges of previous methods: high calculation load and local minima. We tried to implement some previous methods, but the motion correction results were not perfect. After a lengthy study of these methods, we found that neighboring lines in k-space have a strong relationship, and the motion detection of one segment may not correspond to the average motion of all the lines in the segment when the segment size is smaller than a certain number. Due to the strong impact of the neighboring line, the motion of the whole segment may not be corrected properly, which may result in the cost function being trapped in local minima. This finding explained why previous methods cannot correct motion in some cases. Thus, we proposed a new search strategy. The proposed method involves two steps: piecewise linear initial approximation and joint refinement of a global model to perform global estimation. To further improve computational efficiency, golden-section search was used to estimate rotation, and two map data structures were applied to store calculated data. Different focus criteria were compared under the proposed method. Simulations and experimental results demonstrate that the proposed method can effectively and efficiently correct rigid motion (head motion) in MR images.

We also devised an efficient motion correction method based on fast robust correlation. The proposed method corrected motion-distorted images by aligning translational motion between images formed by neighboring frequency segments. To reduce the impact of the strong relationship between neighboring lines, the size of segments cannot be too small. Since the squared difference kernel was invariant to motion between partial-Fourier images, we adopted the absolute value kernel, which can be easily approximated by sinusoidal terms. Total variation of the sum of partial-Fourier images was chosen as the new matching criterion. FFTs are used to calculate correlations for computational speed. Different search strategies to combine and correct motion over the whole k-space were compared. The proposed method can perform real-time processing to reduce image motion artifacts significantly in the simulations and MRI cardiac experiments.

Finally, we designed a novel data-driven motion correction method for magnitude MR images using generative adversarial networks (GANs). GANs (pix2pix model) were implemented to reduce motion artifacts and reconstruct motion-corrupted images through adversarial training between generator and discriminator networks to estimate a motion-corrected image that should be close to the reference image. The training set was made of image pairs consisting of motionless reference images and corresponding motion-simulated images. The proposed method was validated by a simulated motion test set and a real motion (experimental) test set.

The following future work is suggested by our previous studies on this problem:

For the autofocusing method, we expect it to correct 3D rigid motion. For 3D rigid motion, six motion trajectories need to be estimated. Due to the increased search space in 3D, an accurate and efficient piecewise linear initial approximation algorithm is needed. To avoid local minima, one or more restriction conditions should be considered in the process of joint refinement of global model. The proposed method on a windowed image may potentially correct some complicated nonrigid motions. In some cases, we can assume that the whole image can be divided into several small subimages, within which the motion can be modeled as rigid. The subimages are combined after motion of each subimage is corrected by the windowed method.

For the method based on fast robust correlation, we expect it to correct translations with rotation. We may use golden-section search strategy for rotation correction. It should not be hard to extend the proposed method to correct 3D translations, which will make the method more powerful. The proposed method applied to a windowed image will be another attractive extension.

For the method using GANs, we expect it to correct some simple non-rigid motions, such as some motions of joints. Instead of using the same networks for all the motions, a specific network structure and objective function is needed to better fit the motion properties of a certain part of the body. In order to compare different network methods, an authoritative MRI dataset and some metrics should be established.

Bibliography

[1] JL Ackerman, MC Offutt, RB Buxton, TJ Brady, et al. Rapid 3D tracking of small RF coils. In *Proceedings of the 5th Annual Meeting of SMRM, Montreal, Canada*, page 1131, 1986.

[2] Murat Aksoy, Christoph Forman, Matus Straka, Tolga Çukur, Joachim Hornegger, and Roland Bammer. Hybrid prospective and retrospective head motion correction to mitigate cross-calibration errors. *Magnetic Resonance in Medicine*, 67(5):1237–1251, 2012.

[3] Murat Aksoy, Christoph Forman, Matus Straka, Stefan Skare, Samantha Holdsworth, Joachim Hornegger, and Roland Bammer. Real-time optical motion correction for diffusion tensor imaging. *Magnetic Resonance in Medicine*, 66:366–378, August 2011.

[4] Jalal B Andre, Brian W Bresnahan, Mahmud Mossa-Basha, Michael N Hoff, C Patrick Smith, Yoshimi Anzai, and Wendy A Cohen. Toward quantifying the prevalence, severity, and cost associated with patient motion during clinical MR examinations. *J Am Coll Radiol*, 12(7):689–695, Jul 2015.

[5] Brian C Andrews-Shigaki, Brian S R Armstrong, Maxim Zaitsev, and Thomas Ernst. Prospective motion correction for Magnetic Resonance Spectroscopy using single camera retro-grate reflector optical tracking. *Journal of Magnetic Resonance Imaging : JMRI*, 33:498–504, February 2011.

[6] Konstantinos Arfanakis, Ashish A Tamhane, James G Pipe, and Mark A Anastasio. k-space undersampling in PROPELLER imaging. *Magnetic Resonance in Medicine*, 53:675–683, March 2005.

[7] Karim Armanious, Chenming Yang, Marc Fischer, Thomas Küstner, Konstantin Nikolaou, Sergios Gatidis, and Bin Yang. MedGAN: medical image translation using GANs. *arXiv preprint arXiv:1806.06397*, 2018.

[8] David Atkinson, Derek LG Hill, Peter NR Stoyle, Paul E Summers, and Steven F. Keevil. Automatic correction of motion artifacts in Magnetic Resonance Images using an entropy focus criterion. *IEEE Transactions on Medical Imaging*, 16(6):903–910, 1997.

[9] Roland Bammer, Murat Aksoy, and Chunlei Liu. Augmented generalized SENSE reconstruction to correct for rigid body motion. *Magnetic Resonance in Medicine: An Official Journal of the International Society for Magnetic Resonance in Medicine*, 57(1):90–102, 2007.

[10] Christoph Barmet, Nicola De Zanche, and Klaas P Pruessmann. Spatiotemporal magnetic field monitoring for MR. *Magnetic Resonance in Medicine*, 60:187–197, July 2008.

[11] Christoph Barmet, Nicola De Zanche, Bertram J Wilm, and Klaas P Pruessmann. A transmit/receive system for magnetic field monitoring of in vivo MRI. *Magnetic Resonance in Medicine*, 62:269–276, July 2009.

[12] Ariel Benou, Ronel Veksler, Alon Friedman, and T Riklin Raviv. Ensemble of expert deep neural networks for spatio-temporal denoising of contrast-enhanced MRI sequences. *Medical Image Analysis*, 42:145–159, 2017.

[13] Camilo Bermudez, Andrew J Plassard, Larry T Davis, Allen T Newton, Susan M Resnick, and Bennett A Landman. Learning implicit brain MRI manifolds with deep learning. In *Medical Imaging 2018: Image Processing*, volume 10574, page 105741L. International Society for Optics and Photonics, 2018.

[14] Rainer Boegle, Julian Maclaren, and Maxim Zaitsev. Combining prospective motion correction and distortion correction for EPI: towards a comprehensive correction of motion and susceptibility-induced artifacts. *Magnetic Resonance Materials in Physics, Biology and Medicine*, 23(4):263–273, 2010.

[15] Candice A Bookwalter, Mark A Griswold, and Jeffrey L Duerk. Multiple overlapping k-space junctions for investigating translating objects (MOJITO). *IEEE Transactions on Medical Imaging*, 29(2):339–349, 2010.

[16] Timothy T Brown, Joshua M Kuperman, Matthew Erhart, Nathan S White, J Cooper Roddey, Ajit Shankaranarayanan, Eric T Han, Dan Rettmann, and Anders M Dale. Prospective motion correction of high-resolution Magnetic Resonance Imaging data in children. *NeuroImage*, 53:139–145, October 2010.

[17] Akshay S Chaudhari, Zhongnan Fang, Feliks Kogan, Jeff Wood, Kathryn J Stevens, Eric K Gibbons, Jin Hyung Lee, Garry E Gold, and Brian A Hargreaves. Super-resolution musculoskeletal MRI using deep learning. *Magnetic Resonance in Medicine*, 80(5):2139–2154, 2018.

[18] Liang Chen, Paul Bentley, and Daniel Rueckert. Fully automatic acute ischemic lesion segmentation in DWI using convolutional neural networks. *NeuroImage: Clinical*, 15:633–643, 2017.

[19] Joseph Y Cheng, Marcus T Alley, Charles H Cunningham, Shreyas S Vasanawala, John M Pauly, and Michael Lustig. Nonrigid motion correction in 3D using autofocusing withlocalized linear translations. *Magnetic Resonance in Medicine*, 68(6):1785–1797, 2012.

[20] Joseph Y Cheng, Tao Zhang, Nichanan Ruangwattanapaisarn, Marcus T Alley, Martin Uecker, John M Pauly, Michael Lustig, and Shreyas S Vasanawala. Free-breathing

pediatric MRI with nonrigid motion correction and acceleration. *Journal of Magnetic Resonance Imaging*, 42(2):407–420, 2015.

[21] Hongyoon Choi and Kyong Hwan Jin. Fast and robust segmentation of the striatum using deep convolutional neural networks. *Journal of Neuroscience Methods*, 274:146–153, 2016.

[22] William R Crum, Thomas Hartkens, and DLG Hill. Non-rigid image registration: theory and practice. *The British Journal of Radiology*, 2014.

[23] Adriana Di Martino, Chao-Gan Yan, Qingyang Li, Erin Denio, Francisco X Castellanos, Kaat Alaerts, Jeffrey S Anderson, Michal Assaf, Susan Y Bookheimer, Mirella Dapretto, et al. The autism brain imaging data exchange: towards a large-scale evaluation of the intrinsic brain architecture in autism. *Molecular Psychiatry*, 19(6):659, 2014.

[24] Ben A Duffy, Wenlu Zhang, Haoteng Tang, Lu Zhao, Meng Law, Arthur W Toga, and Hosung Kim. Retrospective correction of motion artifact affected structural MRI images using deep learning of simulated motion. *1st Conference on Medical Imaging with Deep Learning (MIDL 2018), Amsterdam, The Netherlands*, 2018.

[25] David Eberly. Thin plate splines. *Geometric Tools Inc*, 2002.

[26] V Edward, C Windischberger, R Cunnington, M Erdler, R Lanzenberger, D Mayer, W Endl, and R Beisteiner. Quantification of fMRI artifact reduction by a novel plaster cast head holder. *Human Brain Mapping*, 11:207–213, November 2000.

[27] Fedwa Essannouni, R Oulad Haj Thami, Driss Aboutajdine, and Ahmed Salam. Adjustable SAD matching algorithm using frequency domain. *Journal of Real-Time Image Processing*, 1(4):257–265, 2007.

[28] H Eviatar, J Saunders, and D Hoult. Motion compensation by gradient adjustment. *Proceedings of the International Society for Magnetic Resonance in Medicine, Vancouver, Canada*, page 1898, 1997.

[29] Hadass Eviatar, B Schattka, JC Sharp, J Rendell, and Murray E Alexander. Real time head motion correction for functional MRI. *Proceedings of the International Society for Magnetic Resonance in Medicine, Philadelphia, Pennsylvania*, page 269, 1999.

[30] Alistair J Fitch, Alexander Kadyrov, William J Christmas, and Josef Kittler. Fast robust correlation. *IEEE Transactions on Image Processing*, 14(8):1063–1073, 2005.

[31] James D Foley, Andries Van Dam, et al. *Fundamentals of interactive computer graphics*, volume 2. Addison-Wesley Reading, MA, 1982.

[32] Hassan Foroosh, Josiane B Zerubia, and Marc Berthod. Extension of phase correlation to subpixel registration. *IEEE Transactions on Image Processing*, 11(3):188–200, 2002.

[33] Karl J Friston, Steven Williams, Robert Howard, Richard SJ Frackowiak, and Robert Turner. Movement-related effects in fMRI time-series. *Magnetic Resonance in Medicine*, 35(3):346–355, 1996.

[34] F Godenschweger, U Kägebein, D Stucht, U Yarach, A Sciarra, R Yakupov, F Lüsebrink, P Schulze, and O Speck. Motion correction in MRI of the brain. *Physics in Medicine and Biology*, 61(5):R32, 2016.

[35] Ian Goodfellow, Jean Pouget-Abadie, Mehdi Mirza, Bing Xu, David Warde-Farley, Sherjil Ozair, Aaron Courville, and Yoshua Bengio. Generative adversarial nets. In *Proceedings of the International Conference on Neural Information Processing Systems (NIPS 2014)*, pages 2672–2680, 2014.

[36] Mark A Griswold, Peter M Jakob, Robin M Heidemann, Mathias Nittka, Vladimir Jellus, Jianmin Wang, Berthold Kiefer, and Axel Haase. Generalized autocalibrating

partially parallel acquisitions (GRAPPA). *Magn Reson Med*, 47(6):1202–1210, Jun 2002.

[37] Edward S Grood and Wilfredo J Suntay. A joint coordinate system for the clinical description of three-dimensional motions: application to the knee. *Journal of Biomechanical Engineering*, 105(2):136–144, 1983.

[38] Jun-Yu Guo, Eugene G Kholmovski, Ling Zhang, and Dennis L Parker. Evaluation of motion effects on parallel MR imaging with precalibration. *Magnetic Resonance Imaging*, 25:1130–1137, October 2007.

[39] E Mark Haacke and John L Patrick. Reducing motion artifacts in two-dimensional Fourier transform imaging. *Magnetic Resonance Imaging*, 4(4):359–376, 1986.

[40] A Haase, J Frahm, D Matthaei, W Hänicke, and K.-D Merboldt. FLASH imaging: rapid NMR imaging using low flip-angle pulses. *Journal of Magnetic Resonance*, 67:258–266, 1986.

[41] J V Hajnal, R Myers, A Oatridge, J E Schwieso, I R Young, and G M Bydder. Artifacts due to stimulus correlated motion in functional imaging of the brain. *Magnetic Resonance in Medicine*, 31:283–291, March 1994.

[42] Mohammad Havaei, Axel Davy, David Warde-Farley, Antoine Biard, Aaron Courville, Yoshua Bengio, Chris Pal, Pierre-Marc Jodoin, and Hugo Larochelle. Brain tumor segmentation with deep neural networks. *Medical Image Analysis*, 35:18–31, 2017.

[43] M Herbst, J Maclaren, JG Korvink, and M Zaitsev. A practical tracking system to avoid motion artifacts. In *Proceedings of the 19th Annual Meeting of ISMRM, Montreal, Canada*, page 2683, 2011.

[44] Derek LG Hill, Philipp G Batchelor, Mark Holden, and David J Hawkes. Medical image registration. *Physics in Medicine and Biology*, 46(3):R1, 2001.

[45] A Hoffmann, SC Faber, KJ Werhahn, L Jäger, and M Reiser. Electromyography in MRI–first recordings of peripheral nerve activation caused by fast magnetic field gradients. *Magn Reson Med*, 43(4):534–539, Apr 2000.

[46] William Scott Hoge. A subspace identification extension to the phase correlation method. *IEEE Transactions on Medical Imaging*, 22(2):277–280, 2003.

[47] A M Hubbard, R I Markowitz, B Kimmel, M Kroger, and M B Bartko. Sedation for pediatric patients undergoing CT and MRI. *Journal of Computer Assisted Tomography*, 16:3–6, 1992.

[48] Peter J Huber. Robust statistics. 1981.

[49] BF Hutton, M Braun, and P Slomka. Image registration techniques in nuclear medicine imaging. In *Quantitative Analysis in Nuclear Medicine Imaging*, pages 272–307. Springer, 2006.

[50] Phillip Isola, Jun-Yan Zhu, Tinghui Zhou, and Alexei A Efros. Image-to-image translation with conditional adversarial networks. In *Proceedings of the IEEE Conference on Computer Vision and Pattern Recognition*, pages 1125–1134, 2017.

[51] Alexander Kadyrov, Hui Yu, Joe Eyles, and Honghai Liu. Explore new eye tracking and gaze locating methods. In *Systems, Man, and Cybernetics (SMC), 2013 IEEE International Conference on*, pages 2866–2871. IEEE, 2013.

[52] Jack Kiefer. Sequential minimax search for a maximum. *Proceedings of the American Mathematical Society*, 4(3):502–506, 1953.

[53] Stefan Klein, Marius Staring, and Josien PW Pluim. Evaluation of optimization methods for nonrigid medical image registration using mutual information and B-splines. *IEEE Transactions on Image Processing*, 16(12):2879–2890, 2007.

[54] Jan Kybic and Michael Unser. Fast parametric elastic image registration. *IEEE Transactions on Image Processing*, 12(11):1427–1442, 2003.

[55] Christian Ledig, Lucas Theis, Ferenc Huszár, Jose Caballero, Andrew Cunningham, Alejandro Acosta, Andrew Aitken, Alykhan Tejani, Johannes Totz, Zehan Wang, et al. Photo-realistic single image super-resolution using a generative adversarial network. In *Proceedings of the IEEE Conference on Computer Vision and Pattern Recognition*, pages 4681–4690, 2017.

[56] Wenqi Li, Guotai Wang, Lucas Fidon, Sebastien Ourselin, M Jorge Cardoso, and Tom Vercauteren. On the compactness, efficiency, and representation of 3D convolutional networks: brain parcellation as a pretext task. In *International Conference on Information Processing in Medical Imaging*, pages 348–360. Springer, 2017.

[57] Chang Liu, Xi Wu, Xi Yu, YuanYan Tang, Jian Zhang, and JiLiu Zhou. Fusing multiscale information in convolution network for MR image super-resolution reconstruction. *Biomedical Engineering Online*, 17(1):114, 2018.

[58] Stephan Liwicki, Georgios Tzimiropoulos, Stefanos Zafeiriou, and Maja Pantic. Euler principal component analysis. *International journal of Computer Vision*, 101(3):498–518, 2013.

[59] Alexander Loktyushin, Hannes Nickisch, Rolf Pohmann, and Bernhard Schölkopf. Blind retrospective motion correction of MR images. *Magnetic Resonance in Medicine*, 70(6):1608–1618, 2013.

[60] Alexander Loktyushin, Hannes Nickisch, Rolf Pohmann, and Bernhard Schölkopf. Blind multirigid retrospective motion correction of MR images. *Magnetic Resonance in Medicine*, 73(4):1457–1468, April 2015.

[61] Alexander Loktyushin, Christian Schuler, Klaus Scheffler, and Bernhard Schölkopf. Retrospective motion correction of magnitude-input MR images. In *Medical Learning Meets Medical Imaging*, pages 3–12. Springer, 2015.

[62] Alexander Selvikvåg Lundervold and Arvid Lundervold. An overview of deep learning in medical imaging focusing on MRI. *Zeitschrift für Medizinische Physik*, 2018.

[63] Michael Lustig, David Donoho, and John M Pauly. Sparse MRI: The application of compressed sensing for rapid MR imaging. *Magnetic Resonance in Medicine*, 58:1182–1195, December 2007.

[64] Julian Maclaren, Michael Herbst, Oliver Speck, and Maxim Zaitsev. Prospective motion correction in brain imaging: a review. *Magnetic Resonance in Medicine*, 69(3):621–636, 2013.

[65] Julian Maclaren, Kuan J Lee, Chaiya Luengviriya, Oliver Speck, and Maxim Zaitsev. Combined prospective and retrospective motion correction to relax navigator requirements. *Magnetic Resonance in Medicine*, 65(6):1724–1732, 2011.

[66] Frederik Maes, Andre Collignon, Dirk Vandermeulen, Guy Marchal, and Paul Suetens. Multimodality image registration by maximization of mutual information. *IEEE Transactions on Medical Imaging*, 16(2):187–198, 1997.

[67] S Malviya, T Voepel-Lewis, O P Eldevik, D T Rockwell, J H Wong, and A R Tait. Sedation and general anaesthesia in children undergoing MRI and CT: adverse events and outcomes. *British Journal of Anaesthesia*, 84:743–748, June 2000.

[68] Kiaran P McGee, Armando Manduca, Joel P Felmlee, Stephen J Riederer, and Richard L Ehman. Image metric-based correction (autocorrection) of motion effects: analysis of image metrics. *Journal of Magnetic Resonance Imaging: An Official Journal of the International Society for Magnetic Resonance in Medicine*, 11(2):174–181, 2000.

[69] Jason Mendes, Eugene Kholmovski, and Dennis L Parker. Rigid-body motion correction with self-navigation MRI. *Magnetic Resonance in Medicine: An Official Journal of the International Society for Magnetic Resonance in Medicine*, 61(3):739–747, 2009.

[70] Mehdi Mirza and Simon Osindero. Conditional generative adversarial nets. *arXiv preprint arXiv:1411.1784*, 2014.

[71] Dwight G Nishimura. *Principles of Magnetic Resonance Imaging*. Stanford University, 2010.

[72] Francisco PM Oliveira and João Manuel RS Tavares. Medical image registration: a review. *Computer Methods in Biomechanics and Biomedical Engineering*, 17(2):73–93, 2014.

[73] Melvyn B Ooi, Sascha Krueger, Jordan Muraskin, William J Thomas, and Truman R Brown. Echo-planar imaging with prospective slice-by-slice motion correction using active markers. *Magnetic Resonance in Medicine*, 66:73–81, July 2011.

[74] Melvyn B Ooi, Sascha Krueger, William J Thomas, Srirama V Swaminathan, and Truman R Brown. Prospective real-time correction for arbitrary head motion using active markers. *Magnetic Resonance in Medicine*, 62:943–954, October 2009.

[75] Kamlesh Pawar, Zhaolin Chen, J Shah, and Gary F Egan. Motion correction in MRI using deep convolutional neural network. In *Proc ISMRM Scientific Meeting & Exhibition*, page 1174, 2018.

[76] Johannes M Peeters and Miha Fuderer. SENSE with improved tolerance to inaccuracies in coil sensitivity maps. *Magnetic Resonance in Medicine*, 69:1665–1669, June 2013.

[77] James G Pipe et al. Motion correction with PROPELLER MRI: application to head motion and free-breathing cardiac imaging. *Magnetic Resonance in Medicine*, 42(5):963–969, 1999.

[78] Josien PW Pluim, JB Antoine Maintz, and Max A Viergever. Mutual-information-based registration of medical images: a survey. *IEEE Transactions on Medical Imaging*, 22(8):986–1004, 2003.

[79] Russell A Poldrack, E Juliana Par-Blagoev, and P Ellen Grant. Pediatric functional Magnetic Resonance Imaging: progress and challenges. *Topics in Magnetic Resonance Imaging : TMRI*, 13:61–70, February 2002.

[80] Robert A Pooley. Fundamental physics of MR imaging. *Radiographics*, 25(4):1087–1099, 2005.

[81] KP Pruessmann, M Weiger, MB Scheidegger, and P Boesiger. SENSE: sensitivity encoding for fast MRI. *Magn Reson Med*, 42(5):952–962, Nov 1999.

[82] Chen Qin, Jo Schlemper, Jose Caballero, Anthony N Price, Joseph V Hajnal, and Daniel Rueckert. Convolutional recurrent neural networks for dynamic MR image reconstruction. *IEEE Transactions on Medical Imaging*, 38(1):280–290, 2019.

[83] Lei Qin, Peter van Gelderen, John Andrew Derbyshire, Fenghua Jin, Jongho Lee, Jacco A de Zwart, Yang Tao, and Jeff H Duyn. Prospective head-movement correction for high-resolution MRI using an in-bore optical tracking system. *Magnetic Resonance in Medicine*, 62:924–934, October 2009.

[84] Kevin Schawinski, Ce Zhang, Hantian Zhang, Lucas Fowler, and Gokula Krishnan Santhanam. Generative adversarial networks recover features in astrophysical images of galaxies beyond the deconvolution limit. *Monthly Notices of the Royal Astronomical Society: Letters*, 467(1):L110–L114, 2017.

[85] Klaus Scheffler and Stefan Lehnhardt. Principles and applications of balanced SSFP techniques. *European Radiology*, 13:2409–2418, November 2003.

[86] E Seto, G Sela, W E McIlroy, S E Black, W R Staines, M J Bronskill, A R McIntosh, and S J Graham. Quantifying head motion associated with motor tasks used in fMRI. *NeuroImage*, 14:284–297, August 2001.

[87] Jan Sijbers, AJ Den Dekker, Johan Van Audekerke, Marleen Verhoye, and Dirk Van Dyck. Estimation of the noise in magnitude MR images. *Magnetic Resonance Imaging*, 16(1):87–90, 1998.

[88] DK Sodickson and WJ Manning. Simultaneous acquisition of spatial harmonics (SMASH): fast imaging with radiofrequency coil arrays. *Magn Reson Med*, 38(4):591–603, Oct 1997.

[89] Aristeidis Sotiras, Christos Davatzikos, and Nikos Paragios. Deformable medical image registration: a survey. *IEEE Transactions on Medical Imaging*, 32(7):1153–1190, 2013.

[90] O Speck, J Hennig, and M Zaitsev. Prospective real-time slice-by-slice motion correction for fMRI in freely moving subjects. *Magma (New York, N.Y.)*, 19:55–61, May 2006.

[91] Stefan Thesen, Oliver Heid, Edgar Mueller, and Lothar R Schad. Prospective acquisition correction for head motion with image-based tracking for real-time fMRI. *Magnetic Resonance in Medicine*, 44(3):457–465, 2000.

[92] Georgios Tzimiropoulos, Stefanos Zafeiriou, and Maja Pantic. Subspace learning from image gradient orientations. *IEEE Transactions on Pattern Analysis and Machine Intelligence*, 34(12):2454–2466, 2012.

[93] André JW Van der Kouwe, Thomas Benner, and Anders M Dale. Real-time rigid body motion correction and shimming using cloverleaf navigators. *Magnetic Resonance in Medicine*, 56(5):1019–1032, 2006.

[94] Carl Vondrick, Hamed Pirsiavash, and Antonio Torralba. Generating videos with scene dynamics. In *Advances In Neural Information Processing Systems*, pages 613–621, 2016.

[95] Shanshan Wang, Zhenghang Su, Leslie Ying, Xi Peng, Shun Zhu, Feng Liang, Dagan Feng, and Dong Liang. Accelerating Magnetic Resonance Imaging via deep learning. In *2016 IEEE 13th International Symposium on Biomedical Imaging (ISBI)*, pages 514–517. IEEE, 2016.

[96] Zhou Wang, Alan C Bovik, Hamid R Sheikh, Eero P Simoncelli, et al. Image quality assessment: from error visibility to structural similarity. *IEEE Transactions on Image Processing*, 13(4):600–612, 2004.

[97] Heidi A Ward, Stephen J Riederer, Roger C Grimm, Richard L Ehman, Joel P Felmlee, and Clifford R Jack. Prospective multiaxial motion correction for fMRI. *Magnetic Resonance in Medicine*, 43(3):459–469, 2000.

[98] Edward Brian Welch, Armando Manduca, Roger C Grimm, Heidi A Ward, and Clifford R Jack Jr. Spherical navigator echoes for full 3D rigid body motion measurement in MRI. *Magnetic Resonance in Medicine*, 47(1):32–41, 2002.

[99] William M Wells, Paul Viola, Hideki Atsumi, Shin Nakajima, and Ron Kikinis. Multimodal volume registration by maximization of mutual information. *Medical Image Analysis*, 1(1):35–51, 1996.

[100] Nathan White, Cooper Roddey, Ajit Shankaranarayanan, Eric Han, Dan Rettmann, Juan Santos, Josh Kuperman, and Anders Dale. PROMO: Real-time prospective motion correction in MRI using image-based tracking. *Magnetic Resonance in Medicine*, 63(1):91–105, 2010.

[101] Wikipedia contributors. Golden-section search — Wikipedia, the free encyclopedia. https://en.wikipedia.org/w/index.php?title=Golden-section_search&oldid=855814054, 2018. [Online; accessed 11-October-2018].

[102] Jonathan Windram, Lars Grosse-Wortmann, Masoud Shariat, Mary-Louise Greer, Mark W Crawford, and Shi-Joon Yoo. Cardiovascular MRI without sedation or general anesthesia using a feed-and-sleep technique in neonates and infants. *Pediatric Radiology*, 42:183–187, February 2012.

[103] Zhiyong Xie and Gerald E Farin. Image registration using hierarchical B-splines. *IEEE Transactions on Visualization and Computer Graphics*, 10(1):85–94, 2004.

[104] Sadie E Yancey, David J Rotenberg, Fred Tam, Mark Chiew, Shawn Ranieri, L Biswas, Kevan J T Anderson, S Nicole Baker, Graham A Wright, and Simon J Graham. Spin-history artifact during functional MRI: potential for adaptive correction. *Medical Physics*, 38:4634–4646, August 2011.

[105] Yan Yang, Jian Sun, Huibin Li, and Zongben Xu. ADMM-Net: A deep learning approach for compressive sensing MRI. *arXiv preprint arXiv:1705.06869*, 2017.

[106] Ryo Yonemoto, Toru Uesugi, Takao Kawamura, and Kazunori Sugahara. Panoramic image generation based on FFT technique and its hardware realization. In *SICE-ICASE, 2006. International Joint Conference*, pages 4174–4177. IEEE, 2006.

[107] M Zaitsev, C Dold, G Sakas, J Hennig, and O Speck. Magnetic Resonance Imaging of freely moving objects: prospective real-time motion correction using an external optical motion tracking system. *NeuroImage*, 31:1038–1050, July 2006.

[108] Maxim Zaitsev, Julian Maclaren, and Michael Herbst. Motion artifacts in MRI: A complex problem with many partial solutions. *Journal of Magnetic Resonance Imaging : JMRI*, 42:887–901, October 2015.

[109] Kun Zeng, Hong Zheng, Congbo Cai, Yu Yang, Kaihua Zhang, and Zhong Chen. Simultaneous single-and multi-contrast super-resolution for brain MRI images based on a convolutional neural network. *Computers in Biology and Medicine*, 99:133–141, 2018.

[110] Tao Zhang, Shilpy Chowdhury, Michael Lustig, Richard A Barth, Marcus T Alley, Thomas Grafendorfer, Paul D Calderon, Fraser J L Robb, John M Pauly, and Shreyas S Vasanawala. Clinical performance of contrast enhanced abdominal pediatric MRI with fast combined parallel imaging compressed sensing reconstruction. *Journal of Magnetic Resonance Imaging*, 40:13–25, July 2014.

[111] Jun-Yan Zhu, Taesung Park, Phillip Isola, and Alexei A Efros. Unpaired image-to-image translation using cycle-consistent adversarial networks. In *Proceedings of the IEEE International Conference on Computer Vision*, pages 2223–2232, 2017.

[112] Barbara Zitova and Jan Flusser. Image registration methods: a survey. *Image and Vision Computing*, 21(11):977–1000, 2003.